Superconducting radio frequency cavities for parametric amplification and optomechanics

by

Alessandro R. Castelli

A dissertation submitted in partial satisfaction of the
requirements for the degree of
Doctor of Philosophy

in

Physics

in the

GRADUATE DIVISION
of the
UNIVERSITY OF CALIFORNIA, MERCED

Committee in charge:
Professor Sayantani Ghosh, Chair
Professor Christopher Viney
Professor Emeritus Raymond Chiao
Professor Jay E. Sharping, Advisor

Summer 2018

Superconducting radio frequency cavities for parametric amplification and optomechanics

The dissertation of Alessandro R. Castelli is approved:

Chair Date

Date

Date

Advisor Date

University of California, Merced

Summer 2018

Abstract

Superconducting radio frequency cavities for parametric amplification and optomechanics

by

Alessandro R. Castelli
Doctor of Philosophy in Physics

University of California, Merced

Professor Sayantani Ghosh, Chair

Superconducting radio frequency (SRF) cavities present a unique opportunity in their potential for extremely large quality factors (Q) which allow for low-loss microwave systems which extend photon lifetimes. They have subsequently been used and improved upon as individual cells of particle accelerators where large accelerating voltages are required. More recently, they have been used as double SRF cavity systems for coupling electromagnetic fields via qubits inserted into the cavity bodies. Capitalizing on this Q enhancement, we propose an SRF cavity system for parametric amplification of these microwave fields from vacuum. This triple SRF cavity consists of a pump cavity with a silicon nitride (SiN) membrane acting as one end-wall and two signal/idler cavities that are separated by an iris plane. Parametric amplification occurs when some parameter of the system varies sinusoidally in time and this subsequently drives the system into oscillation. Here, we vary the length of the cavities by driving the SiN membrane end-wall into motion using the radiation pressure from the pump cavity. Sufficient energy transfer between cavities will allow amplification and subsequent oscillation of the vacuum fields. We will introduce and explain theoretical background, SRF cavity fabrication and testing, SiN membrane mechanics, and lastly double cavity mechanics. We will identify which facets of the project seem feasible at this time.

To my parents, siblings, Vivian, and too many of my friends to list here.

I know it's been a long road and it seems as though I may have forgotten you at times. Just know that I was thinking of all of you during this endeavor and all your words and gestures have pushed me to where I am today. This would not have been possible without your help. Thank you.

Acknowledgments

A portion of the text of this dissertation is a reprint of the material as it appears in "Electromagnetic coupling to centimeter-scale mechanical membrane resonators via RF cylindrical cavities." The co-authors listed in these publications directed and supervised research which forms the basis for the dissertation.

Curriculum vitae

Academic Background

Ph.D. Ongoing graduate student at the University of California, Merced under the joint supervision of Dr. Jay Sharping and Dr. Raymond Chiao working with superconducting radio frequency cavities to study parametric oscillation and optomechanics. August 2012 - Current

B.Sc B.Sc. in AMO Physics from the University of California, Merced. August 2008 - May 2012

Publications

- Martinez, L.A., Castelli, A.R., Delmas, W., Sharping, J.E., & Chiao, R. (2016). Electromagnetic coupling to centimeter-scale mechanical membrane resonators via RF cylindrical cavities. *New Journal of Physics, 18*(11), 113015.
- Piñón, T.M., Castelli, A.R., Hirst, L.S., & Sharping, J.E. (2013). Fiber-optic trap-on-a-chip platform for probing low refractive index contrast biomaterials. *Applied optics, 52*(11), 2340-2345.

Oral Presentations

- *Level repulsion of two coupled 3D microwave cavities for quantum electrodynamics*, APS Far West Section Meeting 2017; Merced, California. (November 2017)
- *Frequency-tunable SRF cavities for microwave opto-mechanics*, APS March Meeting 2017; New Orleans, Louisiana. (March 2017)
- *Microwave frequency electromagnetic coupling to a thin membrane as one end of a cylindrical cavity*, APS March Meeting 2015; San Antonio, Texas. (March 2015)
- *Radio frequency electromagnetic coupling to a thin membrane as one end of a cylindrical cavity*, APS Far West Section Meeting 2014; Reno, Nevada. (October 2014)
- *Evaluation of coupling efficiency alignment parameters for microfluidic, fiber-integrated optical trapping*, U.C. Merced undergraduate thesis presentation session; Merced, California. (May 2012)

Relevant Skills

- Laboratory and Research: experiment design, data collection and analysis (Igor Pro)

- Machine Shop: Lathe, Mill, CNC
- CAD: SolidWorks
- FEA Simulation: COMSOL Multiphysics (for radio frequency cavity simulation)
- Programming: MATLAB, LabVIEW, Python
- Word Processing: LaTeX, Microsoft Office, OpenOffice

Teaching

Fall 2017	Teaching Assistant, Introductory Physcis III
Spring 2017	Teaching Assistant, Modern Physics Lab
Fall 2016	Teaching Assistant, Introductory Physics III (Modern Physics)
Spring 2014	Teaching Assistant, Introductory Physics II
Spring 2013	Teaching Assistant, Introductory Physics I (Classical Mechanics)
Fall 2012	Teaching Assistant, Introductory Physics II (Electricity and Magnetism)

Graduate Coursework

- Classical Mechanics
- Electrodynamics
- Quantum Mechanics
- Statistical Mechanics
- General Relativity
- Quantum Optics

Awards

May 2016	Sharping Research Group Excellence Award
October 2014	3rd place Margaret Burbidge Award for graduate experimental research at the APS Far West Section
May 2013	University of California, Merced–Graduate Summer Fellowship
May 2012	University of California, Merced–Chancellor's Honor List

December 2011	University of California, Merced–Dean's Honor List*
January 2011	Golden Bobcat Scholarship*
January 2009	Frances M. Benton Scholarship*
	*Most recent of successive awards

Contents

List of Figures

List of Tables

Chapter 1

Introduction

1.1 Mechanical oscillators and optomechanics

A mechanical oscillator, generally speaking, consists of a mechanical element that, when displaced from its equilibrium position, experiences a restoring force that results in oscillatory motion. Examples of mechanical oscillators include a mass attached to a spring, a pendulum, and a drumhead. Of course, each of these objects has a rate and time in which they complete one cycle of oscillation. These are referred to as the resonance frequency, f_0, and period, T, respectively. These values are inversely related to each other such that $T = \frac{1}{f_0}$. These parameters are largely determined by the oscillator's mass and the system's stiffness.

Applying an instantaneous force to a mechanical oscillator causes it to oscillate at its resonance frequency but drag and friction from the surrounding environment will cause the amplitude of oscillation, A, to eventually decay to zero. If the force is applied at a rate equal to the oscillator's resonance frequency, however, the amplitude of oscillation will reach its largest possible value. This concept is expressed more succinctly in Fig. 1.1 in which we see the amplitude response of the mechanical oscillator as a function of the frequency of the force applied. The figure also demonstrates the quality of the oscillator through the bandwidth of the Lorentzian curve, Δf. This term is also sometimes called the full width at half maximum (FWHM) since it is the distance between frequencies of oscillation for which the oscillator is pumping half of its total power. We can then introduce an expression for the quality factor, Q, of the system that describes how many oscillations occur before all of the oscillator's energy dissipates. This expression is

$$Q = \frac{\omega_0}{\Delta\omega} = \frac{\omega_0 U_{tot}}{P_{diss}} \tag{1.1}$$

where ω_0 is the angular resonance of the oscillator ($f_0 = \omega_0/2\pi$, $\Delta f = \Delta\omega/2\pi$), U_{tot} is the total energy stored in the oscillator, and P_{diss} is the power dissipated in each cycle.

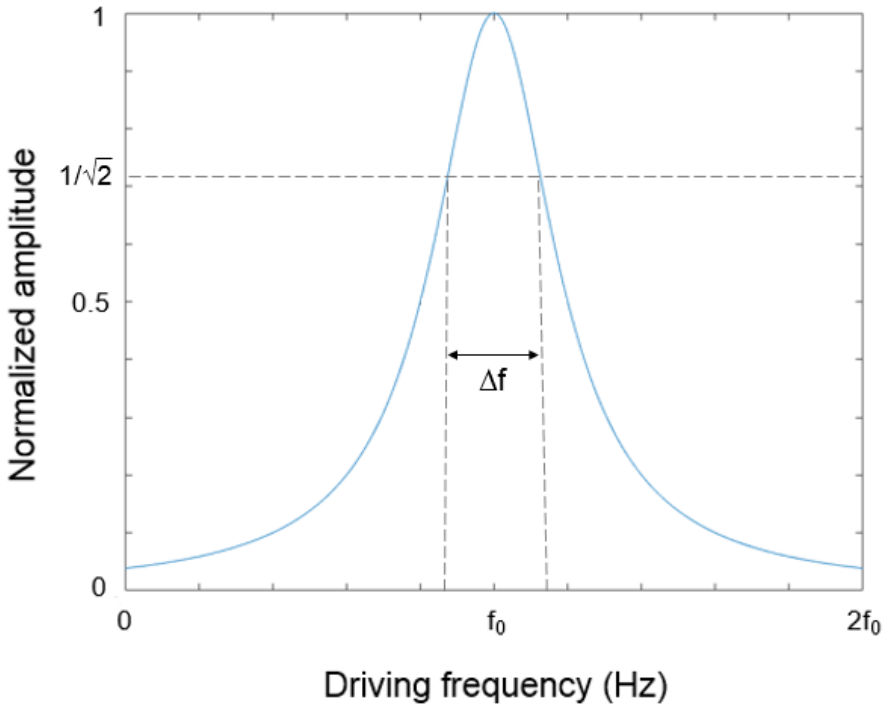

Figure 1.1: Normalized amplitude response of a generalized damped driven oscillator.

Mechanical oscillators are largely used and studied in the context of macroscopic mechanics but have been successfully implemented in optically integrated systems for probing their quantum nature at microscopic sizes. This way of thinking began in 1967 with Braginsky's introduction to the optical spring constant and ponderomotive effects [1]. Fast-forward 40 years and scientists are using this idea to extract or deposit energy into a mechanical oscillator with careful manipulation of light frequencies [2–5]. This field of physics which pertains to these light-matter interactions is called optomechanics and it has been growing rapidly over the past ten years. We will be using ideas such as these to move forward with an experiment to extract electromagnetic and gravitational radiation from vacuum fluctuations.

1.2 Gravitational wave reflection

Typically when a physicist hears the term "Meissner effect" they think to the phenomenon in which a metal that has become superconducting expels any magnetic field permeating its volume. They typically do not, however, envision a gravito-electric analogue to the effect. The gravitational Meissner effect is

a theory proposed by Raymond Chiao et al. in which, much like EM waves, gravitational waves are reflected at the surface of a superconducting metal [6]. The key idea behind the theory lies in the non-localizability of the Cooper pairs that form once a metal has become superconducting. Cooper pairs are inherently non-local systems due to their momenta being completely known. According to Heisenberg's uncertainty principle, this means that a Cooper pair's position within a superconductor is completely uncertain, lending to the idea that the Cooper pair is non-localizable. In short, Cooper pairs are not limited by the equivalence principle (EP) because their non-localizability implies an absence of any meaningful geodesic. This "breaking" of the EP means that Cooper pairs are not subject to free-fall in the presence of a gravitational wave.

Consider a conducting plate subject to an incident gravitational wave (Fig. 1.2) [6]. To an outside observer, the ions and electrons in the normal conducting plate will appear to move in hyperbolic, quadrupolar motion as shown below. However, they are actually remaining stationary and it is space itself that moves in such a way in the presence of incident gravitational radiation. In other words, the ions and electrons are in free fall. Now, consider the plate after it has undergone a superconducting transition. To an outside observer, the ions will behave the same as before, but the electrons, now having formed Cooper pairs, will appear to remain stationary. This causes negative charge to accumulate at points A and C while positive charge gathers at points B and D. The resulting Coulomb forces are extremely large and consequently oppose the effects of the incoming gravitational wave which leads to a reflection-like effect. In this way, superconductors act as mirrors for gravitational radiation.

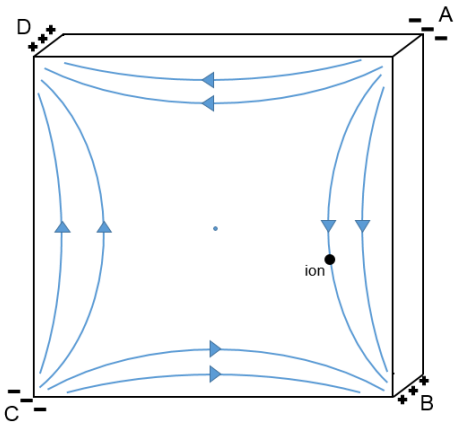

Figure 1.2: The gravitational Meissner effect in action. Hyperbolic trajectories of lattice ions in the absence of their corresponding Cooper pairs leads to a large enough Coulomb force to oppose incoming gravitational radiation [6].

1.3 Purpose of this dissertation

Incorporating a mechanical element into a superconducting cavity system can lead to important cavity quantum electrodynamics (cQED) experiments. The dynamical Casimir effect (DCE) is one such example [7]. The DCE is the idea that electromagnetic radiation can manifest in a cavity system from stimulated vacuum fluctuations provided energy is deposited into the system at a rate that exceeds cavity losses. Expanding this idea to general relativity and recalling the principles of the gravitational Meissner effect, one can envision a gravitational DCE analogue that generates gravitational radiation from vacuum fluctuations.

The research outlined in this thesis aims to create a parametric amplifier and oscillator system using three superconducting cavities with various unique components. I have worked towards this goal by utilizing many facets of physics and achieving certain milestones including:

- Designing a triple cavity that incorporates a silicon nitride membrane
- Building and testing superconducting RF cavities from scratch
  - Machining and etching several generations of niobium cavity prototypes
  - Testing their superconducting properties using a dilution refrigerator system
- Measuring the mechanical response of a silicon nitride membrane as one end-wall of a cylindrical RF cavity
- Achieving sufficient tuning capabilities in a superconducting RF cavity
  - Integrating and testing of many styles of piezoelectric transducers including a stack actuator, bimorphic actuator, and a cryogenic linear drive
- Designing and testing alternative cavity geometries to achieve higher quality factor
- Observing an avoided crossing while tuning a double superconducting RF cavity system operating in the high-Q regime

The following chapters will elucidate the methods and consequences of these achievements.

Chapter 2

Background

2.1 Radio frequency cavities

2.1.1 Electromagnetic modes

The electric and magnetic fields inside a radio frequency (RF) cavity need to be well known in order to operate a successful RF experiment. In general, the modes of the cavity are difficult to determine as there are many cavity configurations available and no two behave in the exact same way. Fortunately, the cavity configuration appropriate for our experiments is the cylindrical pill-box cavity. The model for electromagnetic modes in the cylindrical pill-box cavity turns out to be a relatively simple case due to symmetries in the angular direction, uniformity along the optical axis, and no dependence on cavity length. For this geometry, transverse magnetic (TM) and transverse electric (TM) modes are supported while transverse electromagnetic (TEM) modes are not. TE modes do not have electric field oriented in the direction of propagation, TM modes do not have magnetic field oriented in the direction of propagation, and TEM modes have neither electric or magnetic fields oriented in the direction of propagation. When plugging the boundary conditions for this cavity into the eigenvalue equation, the result shows that the TM and TE modes are Bessel functions. While both have been solved in detail, I will only list the TE modes for reasons that will become apparent later in this thesis. Suffice to say, we will not be using the TM mode equations, but the TE mode equations should provide some insight into the physics that influence choices we have made in this project. The equations for the TE modes of the cylindrical cavity geometry are

$$
\begin{aligned}
E_\rho &= -iH_0 \frac{m\eta\omega R^2}{cx'_{mn}} \frac{1}{\rho} J_m\left(\frac{x'_{mn}}{R}\rho\right) sin\left(m\phi\right) sin\left(\frac{p\pi}{L}z\right) \\
E_\phi &= -iH_0 \frac{\eta\omega R}{cx'_{mn}} J'_m\left(\frac{x'_{mn}}{R}\rho\right) cos\left(m\phi\right) sin\left(\frac{p\pi}{L}z\right) \\
E_z &= 0 \\
H_\rho &= H_0 \frac{p\pi R}{Lx'_{mn}} J'_m\left(\frac{x'_{mn}}{R}\rho\right) cos\left(m\phi\right) cos\left(\frac{p\pi}{L}z\right) \\
H_\phi &= -H_0 \frac{mp\pi R^2}{Lx'_{mn}} \frac{1}{\rho} J_m\left(\frac{x'_{mn}}{R}\rho\right) sin\left(m\phi\right) cos\left(\frac{p\pi}{L}z\right) \\
H_z &= H_0 J_m\left(\frac{x'_{mn}}{R}\rho\right) cos\left(m\phi\right) sin\left(\frac{p\pi}{L}z\right)
\end{aligned}
\tag{2.1}
$$

where m, n, and p are the integer values corresponding to azimuthal, radial, and axial modes, respectively, $\eta = \sqrt{\mu_0/\epsilon_0}$ is the impedance of free space, L is the length of the cavity, $J_m(x)$ is the m$^{\text{th}}$ order Bessel function, x_{mn} is the n$^{\text{th}}$ zero of $J_m(x)$ and $J'_m(x)$ is the derivative of $J_m(x)$ with respect to x [8]. It is worth noting that the resonance for these cavities is well-known and is equal to

$$
\omega_{mnp} = c\sqrt{\left(\frac{x'_{mn}}{R}\right)^2 + \left(\frac{p\pi}{L}\right)^2}. \tag{2.2}
$$

2.2 Superconductivity

Superconductivity is the phenomenon in which a superconducting metal, when cooled below it's critical temperature, T_C, achieves a zero resistance state. This means that a current introduced to such a system could flow for an infinite amount of time with no additional energy needed. While one could write a thesis on superconductivity alone, I am choosing to gloss over many of the finer points and focus on concepts immediately pertinent to the research being conducted. Those interested in a more detailed description of superconductivity might find the following references useful [9–15].

2.2.1 The Meissner effect

As we know, superconductivity is possible because of the formation of Cooper pairs in the atomic lattice. These pairs of electrons also account for the phenomenon known as the Meissner effect which represents an important condition necessary for observing high-Q cavities. In short, Cooper pairs feel a magnetic field and

flow in such a way as to cancel the field before it permeates the superconducting material. The field does permeate to a certain depth within the material, called the London penetration depth, but decays exponentially over typical length scales of tens to hundreds of nanometers. This expulsion of magnetic field manifests as a particularly reflective metallic surface. This enhanced electromagnetic reflectivity significantly enhances the photon lifetime and subsequently the cavity quality factor.

The exact extent to which Cooper pairs expel magnetic field can be found by introducing the total Cooper pair kinetic energy of a superconducting volume

$$\begin{aligned} E_{kin} &= \frac{1}{2} m_c v_c^2 n_c \\ &= \int \frac{1}{2m_c} \left(\boldsymbol{\nabla}\phi + \frac{q_c}{c}\vec{A} \right)^2 |\psi|^2 d^3 r \end{aligned} \tag{2.3}$$

where m_c is the Cooper pair mass, v_c is the Cooper pair velocity, and n_c is the total number of Cooper pairs. The secondary portion of Eq. 2.3 refers to the kinetic component of the Ginsberg Landau free energy equation and helps one infer what happens to Cooper pairs in the presence of a weak magnetic field represented in the form of vector potential $\vec{A}$ [16]. Here, ϕ is the Cooper pair phase, q_c is the Cooper pair charge, and ψ is a macroscopic, complex quantum wave function which allows $|\psi|^2 = n_c^2$. Note that m_c, n_c, and q_c are simply two times a standard electron unit of the same type. Since $\vec{A}$ is small in this instance, one can assume that it couples not to the wave function, ψ, but to the phase, ϕ. The integral simply vanishes as a result and rearranging gives

$$\vec{v_c} = \frac{1}{m_c} \left(\boldsymbol{\nabla}\phi + \frac{q_c}{c}\vec{A} \right) \tag{2.4}$$

for the Cooper pair velocity. The goal here is to find a relationship between the imposed vector potential and the magnetic field produced by the Cooper pairs' response. Relating Cooper pair velocity to current density and subsequently magnetic field should achieve the desired result. The current density can be presented in terms of the Cooper pair velocity

$$\vec{J} = -q_c n_c \vec{v_c} \tag{2.5}$$

and plugging in Eq. 2.4 gives

$$\vec{J} = -\frac{q_c n_c}{m_c} \left(\boldsymbol{\nabla}\phi + \frac{q_c}{c}\vec{A} \right) \tag{2.6}$$

for the relationship between the current density and vector potential. The magnetic field is found by taking the curl of the vector potential

$$\vec{B} = \boldsymbol{\nabla} \times \vec{A} \tag{2.7}$$

yielding

$$\boldsymbol{\nabla} \times \vec{J} = -\frac{q_c^2 n_c}{m_c c}\vec{B} \tag{2.8}$$

when we take the curl of Eq. 2.6. Recalling the Maxwell equation

$$\vec{J} = \frac{c}{4\pi}\boldsymbol{\nabla} \times \vec{B} \tag{2.9}$$

and subsequently taking the curl of Eq. 2.8

$$\begin{aligned} \frac{c}{4\pi}\boldsymbol{\nabla} \times \left(\boldsymbol{\nabla} \times \vec{B}\right) &= \frac{c}{4\pi}\boldsymbol{\nabla}\left(\boldsymbol{\nabla} \cdot \vec{B}\right) - \frac{c}{4\pi}\boldsymbol{\nabla}^2\vec{B} \\ &= -\frac{c}{4\pi}\boldsymbol{\nabla}^2\vec{B} \\ &= -\frac{q_c^2 n_c}{m_c c}\vec{B} \end{aligned} \tag{2.10}$$

one arrives at the London equation

$$\lambda^2\boldsymbol{\nabla}^2\vec{B} = \vec{B} \tag{2.11}$$

where

$$\lambda = \sqrt{\frac{m_c c^2}{4\pi q_c^2 n_c}} \tag{2.12}$$

is the London penetration depth. This expression is easier to appreciate when solving Eq. 2.11 for the magnitude of a uniform magnetic field oriented in the positive z-direction which is perpendicular to a superconducting slab oriented in the $y-z$ plane. The solution to this differential equation, granted x runs perpendicular to the boundary, is

$$B_z(x) = B_0 e^{-x/\lambda} \tag{2.13}$$

which demonstrates the exponential decay of the magnetic field beyond the surface of the superconductor.

2.2.2 Type I and type II superconductors

It is worth mentioning that there is a slight caveat to the Meissner effect in the existence of type II superconductivity. In a type I superconductor below its T_C, the

metal expels all magnetic field present in its interior as the Meissner effect holds. However, Niobium (Nb) is a type II superconductor and, therefore, experiences magnetic flux vortices at a field strength referred to as the critical field, H_{C1}. At secondary critical field H_{C2}, the metal is driven back to its non-superconducting state. The vortices each trap a flux quanta given by $\Phi_0 = h/q_c$ and their density is proportional to the strength of the field applied. This means there is a range of magnetic fields between which the Meissner effect does not completely describe the physics of the superconducting system even though the temperature of the metal is below its critical temperature value. Fortunately, most, if not all, of the experiments performed within this thesis occur at fields as close to null as possible. So, even though we are working predominantly with a type II superconductor, we can largely ignore any potential side-effects that might be caused by flux trapping.

2.3 Superconducting radio frequency cavities

2.3.1 Surface resistance and quality factor

When considering the general resistivity of a metal, one must take into account all the sources of interference that an electron can encounter. The general formula for a metal's resistivity as a function of temperature is

$$\rho\left(T\right) = \rho\left(0\right) + A\left(\frac{T}{\Theta}\right)^{n} \int_{0}^{\frac{\Theta}{T}} \frac{x^{n} dx}{\left(e^{x}-1\right)\left(1-e^{x}\right)} \tag{2.14}$$

where $\rho\left(0\right)$ is the residual resistivity due to impurities in the metal, A is a constant based on degree n, T is the temperature, and Θ is the Debye temperature [17]. As electrons freely flow along the cavity surface, any impurities in the atomic lattice impede their progress and consequently add to the resistivity of the metal. Unlike electron scattering from phonons or other electrons, this residual resistivity remains present, even very close to $T = 0$. If the resistivity is due to electron-electron scattering, we use the case of $n = 2$. If we observe electrons jumping between s and d states, we use the $n = 3$ case due to electron-phonon interactions between these states. Lastly, if we observe electron-phonon interaction within one conduction band, we use the $n = 5$ case. If we observe more than one of these instances, we simply add that term to the overall resistivity equation.

Once a material has undergone its superconducting transition, all terms except $\rho(0)$ vanish. This constant is of extreme import in superconducting radio frequency (SRF) cavity mechanics. The BCS theory of superconductivity, named after John Bardeen, Leon Neil Cooper, and John Robert Schrieffer, offers a model for this surface resistance that remains very accurate at temperatures below $T_C/2$. The expression for the surface resistance of a superconductor according to BCS theory

as it applies in an SRF cavity is

$$R_{BCS}\left(T\right) = \frac{B}{T} f^2 e^{-\Delta(T)/kT} \tag{2.15}$$

where f is the RF frequency inside the cavity, k is Boltzmann's constant, $\Delta\left(T\right)$ is half the band gap of the superconductor for a given temperature, and B is a constant based on several superconducting properties including coherence length, penetration depth, Fermi velocity, and mean free path [9]. Unfortunately, the BCS theory cannot model the behavior perfectly due to imperfections in the superconducting material raising the minimum resistance level. This residual resistance R_0 cannot be accounted for theoretically and so must be measured experimentally. Once the residual resistance has been found, we can use the expression for the surface resistance of a superconductor

$$R_S = R_{BCS}\left(T\right) + R_0 \tag{2.16}$$

to accurately model a conducting system.

In a very basic sense, SRF cavities operate through seeded microwave radiation propagating into a cavity and reflecting in such a way as to form standing waves. This reflection occurs due to currents along the inner surface of the cavity being driven into motion thereby emitting electromagnetic waves themselves. These currents are highly susceptible to resistance in the cavity wall which remains nonzero for RF frequencies, even at the superconducting level. This resistance leads to driven currents causing heating and power dissipation in the wall's surface. The physical properties involved in this dissipation lead to one of the most sought after figures of merit in SRF superconductivity, quality factor (Q). The quality factor of a cavity can be understood as the number of RF cycles the cavity can support before all of the wave's power is dissipated. As such, the quality factor is defined as

$$Q = \frac{\omega_0 U_{tot}}{P_{diss}} \tag{2.17}$$

where ω_0 is the resonant RF frequency of the cavity, U is the stored energy as defined by

$$U = \frac{1}{2}\mu_0 \int_V \left|\vec{H}\right|^2 dV = \frac{1}{2}\epsilon_0 \int_V \left|\vec{E}\right|^2 dV \tag{2.18}$$

and P_{diss} is the dissipated power, defined by

$$P_{diss} = \frac{1}{2} R_s \int_S \left|\vec{H}\right|^2 ds. \tag{2.19}$$

The equation for the amount of energy stored in the cavity, U_{tot}, results from the fact that the time averaged energy due to the electric field is equal to that of the magnetic field and there is a 90° phase shift between the fields meaning the

energy is constantly transfered between the E-field and B-field. The expression for the dissipated power of the cavity results from a rise in thermal activity based on resistive heating in the cavity walls. One can then express Q_0 as

$$Q = \frac{G}{R_S} \tag{2.20}$$

where, for clarity,

$$G = \frac{\omega_0 \mu_0 \int_V \left|\vec{H}\right|^2 dV}{\int_S \left|\vec{H}\right|^2 da} \tag{2.21}$$

is known as the geometrical constant. Interestingly, the geometrical factor is affected by changes to the cavity's shape but not its size. This is not to say that Q is unaffected by cavity size, however, since the expression for R_S, and therefore P_{diss}, depends on the resonant frequency ω_0. Q is the most important figure of merit we look for in our SRF cavities since the threshold for parametric amplification in our triple cavity scheme is inversely proportional to Q^3. We will examine this result and its implications further in section 2.4.

2.3.2 Multipacting

Multipacting occurs when a spontaneous emission electron is accelerated by the field inside the cavity and collides with another section of the cavity wall. This impact initiates an avalanche effect through which more electrons can break off and gather together. The buildup of electrons can lead to a temperature increase and eventual thermal breakdown. In addition, a resonance response causes these electrons to absorb RF power and hinder the buildup of the field inside the cavity. As a result, Q of the cavity can drop well below desired levels. If the multipacting is a result of a "soft" barrier, it is possible to overcome the effect by simply driving the system further. A "hard" barrier, on the other hand, cannot be overcome by processing and drastically lowers the cavity's Q. Since this hard barrier is a result of the cavity's structure, the only method of avoiding it short of physical restructure involves lowering the field inside the cavity. Soft barriers will not resurface in subsequent experiments if the cavity is kept in vacuum which suggests that multipacting is strongly affected by oxidation or other absorption processes of the first few atomic layers in the cavity walls. Thermometers and light detectors can aid in the detection and locating of multipacting orbits. Once the location of the sites is known, taking action against them in the form of geometric modification or a change in resonant conditions is possible. Applying DC fields to disrupt the multipacting trajectories and hence change resonant conditions acts as another means of avoiding the phenomenon.

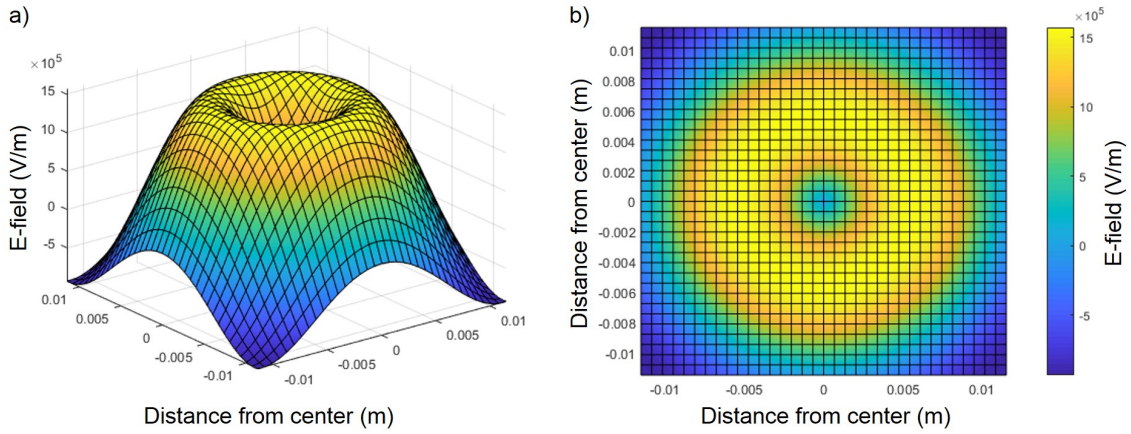

Figure 2.1: a) A contour plot of the TE_{011} mode E-field intensity at the mid-point of the cavity's length where it is expected to be the strongest (Eq. 2.1, E_ϕ). The magnitude of the field is lower than levels in particle accelerators in which multipacting occurred. b) A heatmap representing the contour plot shown in a). One can imagine this as a slice of the E-field strength profile of the cavity taken at $L/2$.

In determining the expected peak E-field strength for our SRF cavity, it is useful to recall the equation for the cavity energy density in terms of the electric and magnetic field strengths; $u = \frac{1}{2}(\epsilon_0 E^2 + \frac{1}{\mu_0} B^2)$. Within the volume of the cavity, we see that the non-zero components of the fields for the TE_{011} mode are E_ϕ, B_z, and B_ρ. Plugging these fields into the energy density equation, integrating over the volume of the cavity to obtain U_{tot}, rearranging Eq. 2.17, and simplifying, we arrive at the equation for peak B-field

$$B_0 = \frac{2x'_{mn}}{R^2\omega}\sqrt{\frac{2P_{in}Q}{\epsilon_0 L\omega J_0(x'_{mn})}} \tag{2.22}$$

which has the correct units of Teslas.

Plugging in all the cavity parameters and plotting the E-field at $z = L/2$ (Fig. 2.1) leads us to expect that the peak electric field for our operating domain will be 150 kV/m, which is a factor of 10-100 below the threshold for multipacting and thermal breakdown issues identified in accelerator configurations. An active area of research and development in the accelerator SRF cavity community is the identification of mechanisms effecting Q rolloff at high peak electric field strengths. Typically one observes a decrease in Q as the peak electric field exceeds values on the order of 5-10 MV/m [18].

2.3.3 Figures of merit

The sample can of the dilution refrigerators has an inner diameter of 15 cm, and a usable inner height of around 20 cm. The samples placed inside can be cooled down to tens of milli-Kelvin when He 3 isotope gas is used for heat transfer. Microwave access to the sample can is achieved using superconducting SMA cables installed in both dilution refrigerators. The RF power originates from an RF signal generator that supplies an AC signal which is injected into the cavity via the aforementioned SMA cables. The method of coupling this signal to the cavity mode(s) is of utmost importance as losses will always be present at the input and output coupling regimes. The main goal in this aspect of SRF cavity physics is to minimize the losses associated with generating and receiving the RF signal. This is accomplished by inserting an antenna-like input coupler supporting a TE RF mode into one end of the cavity and placing a similar output coupler on the opposite end.

While not explicitly the case in SRF experiments, undriven cavity mechanics highlight important aspects of cavity performance. The input and output coupler external quality factors are two such aspects and they lead directly to the couplers' respective coupling constants. Recall our definition of the cavity Q from the previous section: $Q = U_{tot}/P_{diss}$. Now, replacing P_c with P_e for the power lost from the input coupler and P_t for the power lost from the output coupler, we see that

$$Q_{e/t} = \frac{U_{tot}}{P_{e/t}} \tag{2.23}$$

where $Q_{e/t}$ is either the quality factor of the input or output coupler, respectively. We can then define some coupling parameters thusly

$$\beta_{e/t} = \frac{Q}{Q_{e/t}} = \frac{P_{e/t}}{P_{diss}} \tag{2.24}$$

where $\beta_{e/t}$ can be thought of as the coupling strength of the input or output coupler [19]. As is apparent by the equations above, a larger $\beta_{e/t}$ represents a relatively high loss coupler with respect to the loss from the cavity wall. Therefore, it becomes clear that a low value of β is ideal for SRF experiments where low loss is not only desirable but necessary.

2.3.4 Residual losses

As mentioned before, the BCS theory can prove extremely useful in theoretically determining a cavity's surface resistance. However, another factor in R_{BCS} needs to be addressed before the cavity's surface resistance can truly be minimized. The residual resistance, denoted as R_0, is vital to the understanding of an SRF cavity's experimental limitations. Regardless of how much one cools a system in order to reduce its R_{BCS}, the residual resistance will ultimately act as the resistance "barrier"

that no amount of cooling can overcome. The factors that commonly play a role in increasing a cavity's residual resistance include residues from chemical etching, condensed gases, and any foreign materials used in the fabrication process. As such, it remains a constant struggle to practice optimal cleanliness during machining, coating, and assembling processes.

Typical residual losses fall close to areas of high electric and magnetic field implying that they could be field dependent. These losses are still very small (on the order of nΩ) but can still lower the Q of the cavity by an order of magnitude. Unsurprisingly, points of significantly higher resistances can be attributed to defects in the material. Defects can lead to thermal breakdown of superconductivity, but this will be covered more in the next section. Aside from direct phonon generation from the RF field [20], proposed sources of residual resistance that do not result from the cavity wall include design flaws in multi-celled structures and non-uniformity of material at cell joints. Trapped magnetic flux can also lead to a significant increase in residual resistance and even thermal breakdown.

Hydrogen buildup in the niobium can manifest during cooling as a hydride precipitate at the cavity surface. The hydrides increase surface resistance leading to more losses within the cavity thereby decreasing the overall Q. The most prominent precipitation temperatures lay between 150 and 60 K, so the amount of time spent cooling between these two boundaries determines how likely a cavity will contain hydrides. Ideally, bulk hydrogen concentration in niobium should be less than 2 ppm by weight in order to avoid detrimental amounts of hydrides from forming. Commercial niobium usually does not contain more than 1 ppm by weight, so remaining below this critical level should not be a problem.

Residual losses from oxides are essentially inconsequential when compared to cavities without the oxide layer. In fact, residual resistance increased by less than 1-2 nΩ when the oxygen layer was re-introduced to the niobium surface. The one advantage, it would appear, of the oxide-free cavity surface is a reduced sensitivity to residual loss caused by external fields. The lack of oxidation also implies a lack of flux trapping centers allowing for the Meissner affect to occur unimpeded.

2.3.5 Thermal breakdown

Fabricating niobium cavities and even niobium coated cavities is an exceptionally sensitive process involving a vacuum sealed environment and state of the art deposition technologies. Often times when manufacturing cavities for use in SRF experiments, imperfections on the order of micrometers can arise from mistakes made during the machining or coating processes. These defects considerably hinder the performance of the cavity during SRF experiments and could potentially lead to thermal breakdown of superconductivity in the cavity walls.

Thermal breakdown is the result of current flowing through a defect present

in the niobium and, since the defect is not superconducting, subsequently heating the surrounding material to above its critical temperature. Typically, DC currents will not travel through defects because they take the path of least resistance; i.e. the superconducting material surrounding the defects. However, in the case of RF frequencies, the impedance causes the current to travel through these defects leading to an increase in temperature since they display a resistance substantially larger than zero [21].

The increase in temperature substantially reduces the amount of effort involved in finding defects. Several temperature mapping techniques are available for locating the source of the heating and, once found, the defect can be removed thereafter. Several types of defects have been known to find their way into SRF cavities and most are a direct result of remnants from treatment processes. For example, a drying stain from chemical washing mere micrometers in diameter can contain crystals containing K, Cl, and P. In Cu cavities sputtered with Nb, stray Cu particles from machining can serve as another type of quenching medium. In fact, any sort of foreign matter incident on the superconducting surface of the cavity will inexorably lead to some level of quenching. Thermal breakdown is a highly undesirable effect to have present in an SRF cavity, so understanding its sources and its model proves beneficial.

2.3.6 A simple model for thermal breakdown

The quenching field that leads to thermal breakdown can be written as

$$H_{max} = \sqrt{\frac{(4\kappa(T_c - T_b)}{aR_n}} \tag{2.25}$$

where R_n is the normal state resistance, a is the defect radius, κ is the thermal conductivity, and T_b is the bath temperature.

The guided repair method works especially well when trying to eliminate one or two larger defects resulting from manufacturing error. These can be located through thermometry and promptly removed by standard machining practices. This method does not work on smaller defects that arise from poor cavity preparation or handling.

At very low temperatures, i.e. below 4.2 K, thermal conductivity is simply proportional to the residual resistivity ratio (RRR). The most effective method of avoiding thermal breakdown when dealing with very small interstitial defects is to raise the thermal conductivity κ. Raising thermal conductivity becomes essential when realizing that H_{max} is proportional to $\sqrt{\kappa}$. In the end, raising RRR becomes the most effective way to reduce the risk of field quenching at defect sites in the cavity.

Depositing a micron-thick layer of niobium onto a copper cavity is yet another method of deterring unfavorable thermal effects during high driving field experiments. Cavities of this sort have rarely been seen to quench, but RF losses do noticeably increase with field intensity. This option implies that researchers must choose between a purely niobium cavity and a copper cavity sputtered with niobium.

2.4 A superconducting Nb triple cavity for parametric amplification and oscillation

2.4.1 A brief introduction to nonlinear optics

Nonlinear optics refers to the branch of optics in which the induced polarization of a material is given by a nonlinear relationship between the electric field strength and the electric susceptibility of the space through which the light is traveling. In conventional optics, the induced polarization is given by

$$\tilde{P}(t) = \epsilon_0 \chi^{(1)} \tilde{E}(t) \tag{2.26}$$

where $\tilde{P}(t)$ is the induced polarization, $\chi^{(1)}$ is the linear electric susceptibility, and $\tilde{E}(t)$ is the electric field magnitude [22]. The tilde above certain variables denotes that the variable is rapidly varying with time. This equation represents a very large portion of optical physics in which the induced polarization of a material is simply proportional to the electric field magnitude. Nonlinear optics, on the other hand, allows for very interesting quantum effects and has been gaining traction in many fields of physics as a result. In a nonlinear medium, the induced polarization takes the form

$$\begin{aligned} \tilde{P}(t) &= \epsilon_0 \left[\chi^{(1)} \tilde{E}(t) + \chi^{(2)} \tilde{E}^2(t) + \chi^{(3)} \tilde{E}^3(t) + \cdots \right] \\ &\equiv \tilde{P}^{(1)}(t) + \tilde{P}^{(2)}(t) + \tilde{P}^{(3)}(t) + \cdots \end{aligned} \tag{2.27}$$

in which $\chi^{(2)}$ and $\chi^{(3)}$ are the second- and third-order susceptibilities, respectively. Each of these susceptibilities leads to a host of nonlinear effects such as second-harmonic generation (SHG), four-wave mixing (FWM), and optical parametric amplification and oscillation (OPA/OPO). It would be too time consuming to delve further into each of these processes fully, but a quick overview of each should be sufficient for the next section which explores the finer points of the overarching project.

These processes become easier to understand when introducing the general form of the nonlinear wave equation

$$\boldsymbol{\nabla}^2 \tilde{E} - \frac{n^2}{c^2}\frac{\partial^2 \tilde{E}}{\partial t^2} = \frac{1}{\epsilon_0 c^2}\frac{\partial^2 \tilde{P}^{NL}}{\partial t^2} \tag{2.28}$$

where n is the linear refractive index, c is the speed of light in vacuum, and $\tilde{P}^{NL}$ is the nonlinear polarization. Given a laser beam with electric field strength

$$\tilde{E}\left(t\right) = Ee^{-i\omega t} + c.c. \tag{2.29}$$

and a material for which $\chi^{(2)}$ is nonzero, the nonlinear polarization induced in the material is given by

$$\begin{aligned} \tilde{P}^{(2)}\left(t\right) &= \epsilon_0 \chi^{(2)} \tilde{E}^2\left(t\right) \\ &= 2\epsilon_0 \chi^{(2)} EE^* + \left(\epsilon_0 \chi^{(2)} E^2 e^{-i2\omega t} + c.c.\right) \end{aligned} \tag{2.30}$$

where the second term demonstrates the polarization's nonlinear dependence on the electric field; specifically the potential for generation of electromagnetic radiation at twice the pump frequency of the laser beam.

SHG is a second-order nonlinear process in which two photons of frequency ω are destroyed to produce one photon at frequency 2ω. The pump electric field of a laser interacts with molecules in the nonlinear medium and causes the molecules' electrons to oscillate in an anharmonic potential which leads to a mixing of energy between fields of frequency ω and 2ω. Phase matching conditions allow for more or less efficient transfer of energy between the two fields with conversion efficiency of up to 80% being highly achievable [22]. This process can also be understood in terms of atomic energy levels as shown in Fig. 2.2. SHG is a specific case of three-wave mixing (TWM) which is simply a nonlinear process described by two photons of not necessarily equal frequency being converted into a higher frequency photon or vice-versa.

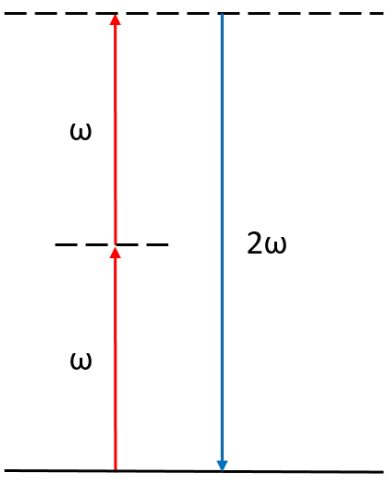

Figure 2.2: An energy level diagram demonstrating second harmonic generation. Two photons of angular frequency ω are excited to a virtual energy level and combine to form a photon of angular frequency 2ω. This is a specific case of three wave mixing.

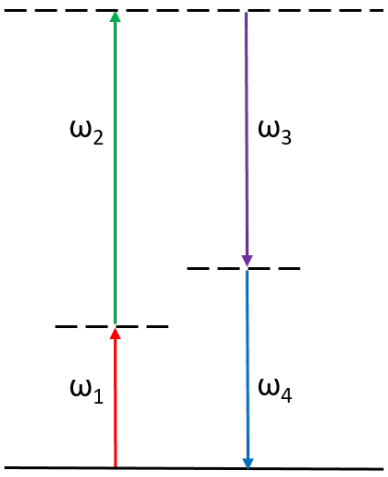

Figure 2.3: An energy level diagram demonstrating four wave mixing. Here, two photons of different angular frequencies combine and are re-emitted as two photons of two more different frequencies. Energy conservation requires that $\omega_1 + \omega_2 = \omega_3 + \omega_4$.

FWM is similar to TWM in the sense that photons of a certain input frequency are converted into photons of a certain output frequency. In the case of FWM, however, three photons of not necessarily equal frequency are converted into a

photon of higher frequency. Non-degenerate FWM can also occur in which two not necessarily equal frequency photons are converted to two photons of different frequencies. An energy level diagram outlining the case of non-degenerate FWM is shown below in Fig.2.3. Lastly, OPA occurs when light passing through a nonlinear medium experiences an increase in signal amplitude due to gain. OPO occurs if OPA takes place in a cavity-like environment.

2.4.2 Triple cavity design

The, as of now theoretical, triple SRF cavity consists of three SRF chambers that work in unison to achieve parametric amplification/oscillation. These chambers are called the "pump cavity" and the two "signal/idler" cavities. Fig. 2.4 below demonstrates the geometry and component assembly of the three cavities. The system design utilizes many facets of physics so it is perhaps best to break down each chamber individually for ease of explanation and understanding.

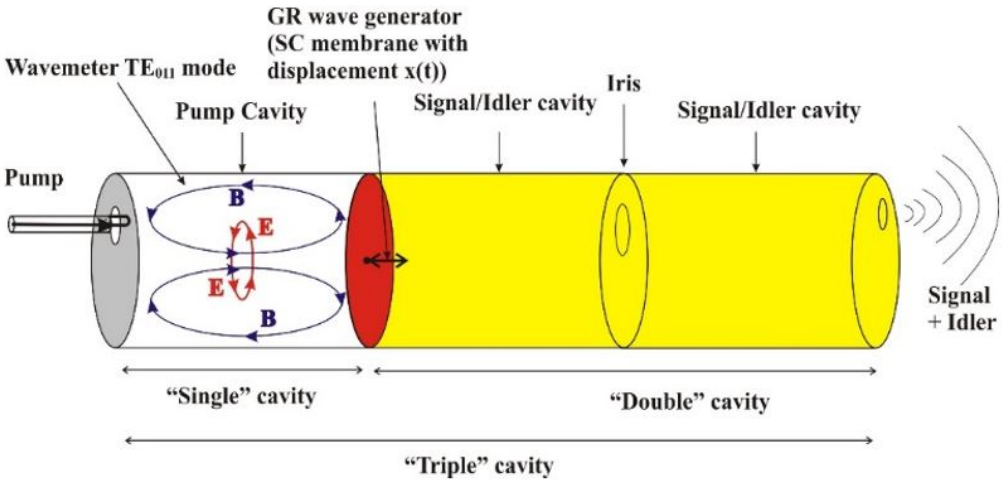

Figure 2.4: A cartoon demonstrating the mechanics behind the triple cavity system. The silicon nitride membrane is driven into motion by the electromagnetic radiation pressure in the pump cavity. The iris splits the dual cavity mode by the same amount as the separation between resonances determined by maximum membrane displacement. The rapid change in boundary condition then leads to a build-up of virtual photons in the dual signal/idler cavity until real photons are produced [23].

The pump cavity is an SRF cavity of extremely high Q (10^9 or greater) with a silicon nitride membrane attached as one of its end-caps. The RF pump signal, centered around 11 GHz, enters the cavity where the build-up of radiation pressure

then acts as the driving force on the membrane (more on driving silicon nitride membranes in Chapter 4). Of course, the mechanical resonance, Ω_m, of the membrane is much smaller than that of the driving force ($F \propto B^2$, $\omega_F = 2\omega_0 = 22$ GHz), but it is assumed that the extremely large frequency will drive the membrane as a free mass.

The rapidly changing boundary condition for the vacuum field in the signal/idler cavities acts as an oscillatory parametric drive for the build-up of energy in those cavities. The iris separating these cavities will be engineered to generate the same mode-splitting we would expect from the Doppler-shifted photons which deposit or extract energy from the oscillating boundary. We predict that we can achieve threshold for parametric amplification and subsequent oscillation with a sufficient RF power seeded into the pump cavity.

2.4.3 Triple cavity parametric amplification and oscillation

Martin Crocce derives an expression for photon production in these types of cavities and arrives at the equation [24]

$$N(t) = -\frac{1}{2} + \frac{1}{4}e^{2at} + \frac{1}{4}e^{-2at} \tag{2.31}$$

where

$$a = \frac{p^2 c^2 \pi^2 \epsilon_{max}}{2\omega L^3}. \tag{2.32}$$

Here, p is the same axial mode integer value mentioned previously, ϵ_{max} is the maximum membrane amplitude, ω is the cavity resonance, and L is the cavity length. Assuming a condition in which the gain of the system is larger than the system losses, we can write $P_g > P_l$. This assumption leads to the condition in which

$$\frac{d}{dt}N(t) = 2aN(t) > \frac{\omega}{Q}N(t) \tag{2.33}$$

where Q is the cavity quality factor. Assuming that the mechanical resonance, Ω, is twice the cavity resonance ($\Omega = 2\omega$), letting $\mathcal{L}_{eff} = \pi c/\omega$, and rearranging, we arrive at the relationship

$$\Omega\epsilon_{max} > \frac{2\pi c}{Q}\left(\frac{L}{\mathcal{L}_{eff}}\right)^3. \tag{2.34}$$

If $v = \Omega\epsilon_{max}$ and recalling $U_{kin} = \frac{1}{2}mv^2$, we see that

$$U_{kin} \geq \frac{1}{2}m\left(\frac{2\pi c}{Q}\left(\frac{L}{\mathcal{L}_{eff}}\right)^3\right)^2 \tag{2.35}$$

To find the threshold condition in terms of input and dissipated power, we can write

$$P_{thresh} \geq \frac{U_{kin}}{\tau} \tag{2.36}$$

where $\tau = Q/\omega$ is the time constant associated with energy dissipation in these cavities. Lastly, plugging in our previous expression for U_{kin} leads to

$$P_{thresh} \geq \frac{\omega m}{2Q} \left(\frac{2\pi c}{Q} \left(\frac{L}{\mathcal{L}_{eff}} \right)^3 \right)^2 \tag{2.37}$$

which is the pump power required to achieve parametric amplification/oscillation in the triple cavity setup. Calculating this value using a cavity Q of approximately 10^9 gives a threshold power of 250 μW.

Chapter 3

Building a high-Q SRF cavity

3.1 Design

In this section, I will outline the steps taken to decide on an SRF cavity's various facets of design from a theoretical and experimental perspective. These steps will be largely based on the experimental goals laid out in the introduction section of this thesis. One should always give careful consideration to a cavity's geometry when designing a high-Q SRF cavity. Many factors, such as field cut-off, theoretical Q limitations, and mode-mapping will affect geometry choice. In fact, choosing a geometry could be entirely based on factors such as these if the shape of the cavity is not imperative to the experiment's success. Assuming one is not limited to a geometry based on experimental restrictions, we shall discuss the choices made in deciding on the cylindrical cavity and the TE_{011} mode.

3.1.1 Cylindrical geometry

There were several options to consider while deciding on a cavity geometry for the experiment. These included open cavities such as those used by Kuhr et al. [25] and high-purity aluminum rectangular/cylindrical cavities such as those used by Reagor et al. [26]. Deciding on a cylindrical geometry for the triple cavity system came about as a result of a desire for simplicity. Open cavities require exceptional alignment to achieve quality factors in-line with our needs and they seem inconvenient for experimentation inside the DR. Rectangular cavities have the potential for symmetry but this is not as inherent as it is for cylindrical cavities. The field mechanics are also greatly simplified for interactions with integrated mechanical components. As mentioned in section 2.1.1, an azimuthally uniform field strength coupled with an adjustable cavity length that does not affect the field distribution are highly desirable traits when considering . This means we can build our cavities to DR specifications while only keeping radius in mind since

any length will support all cavity modes provided it is not below wavelength cutoff. Additionally, the on-axis fields are good candidates for potential interaction with any mechanical components we decide to integrate into the system. Any field mechanics involving spectral splittings with an iris become much easier as well.

3.1.2 Investigation of cylindrical modes

The modes of the cylindrical cavity span a relatively large bandwidth. The locations of these modes are given with respect to their D/L ratio in the following helpful chart (Fig. 3.1) which we replicated based on a paper published by I.G. Wilson of Bell Labs in 1946 [27]. D and L represent the diameter and length of the cavity, respectively. The spectrum for one of our cylindrical cavities is shown immediately after in Fig. 3.2.

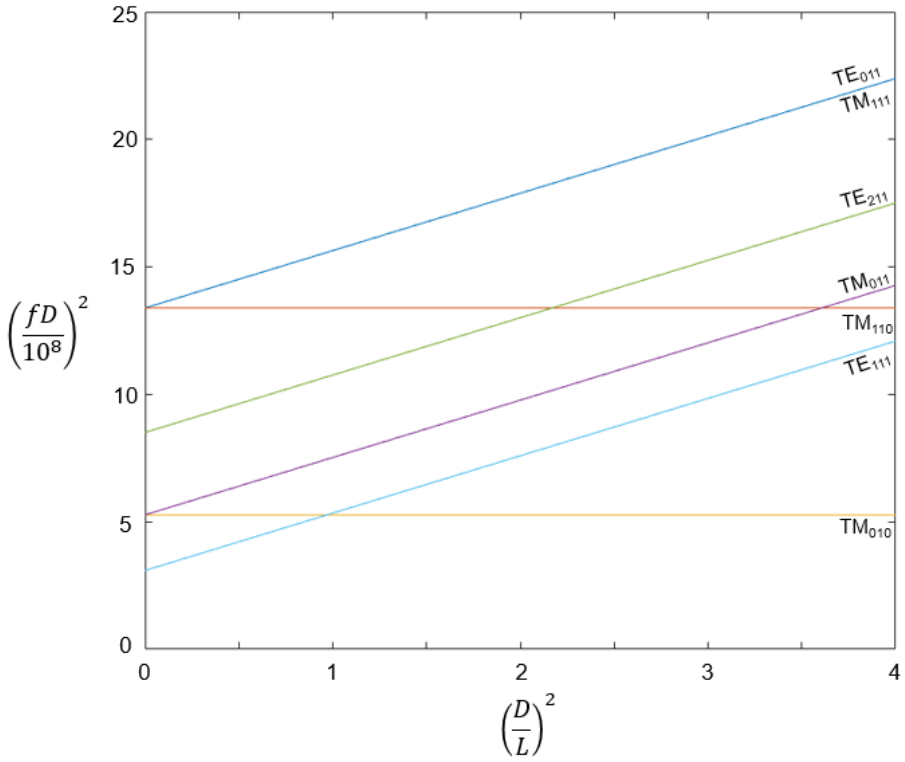

Figure 3.1: We created this mode map using a Bell Labs journal article as the basis and used it to determine appropriate values for the ratio of D/L in our cylindrical cavities. [27].

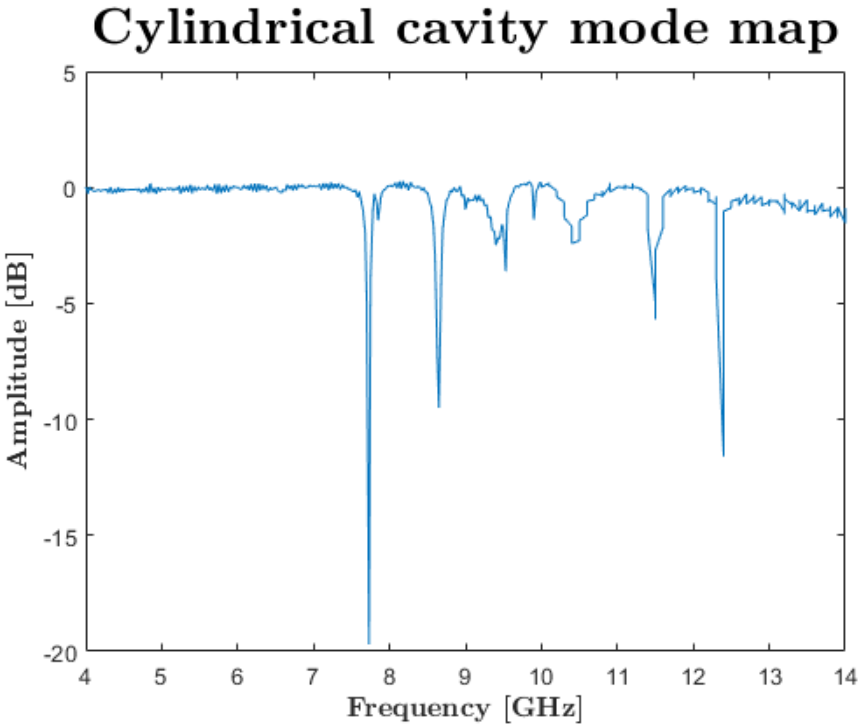

Figure 3.2: A typical reflection spectrum for one of our cylindrical cavities. The TE_{011} mode is located between 11 and 12 GHz. The uneven peak shape is caused by the TM_{111} mode.

This gives many options for the operating frequency of the triple cavity system, but it is well known that the TE_{011} mode offers the best quality factor for this specific geometry [28]. This mode is degenerate with the TM_{111} mode as shown in Fig. 3.3. This mode is often referred to as a "parasitic" mode due to the fact that it has an inherently lower quality factor which carries over to the TE_{011} mode if the degeneracy is not broken in some fashion. Generally speaking, the degeneracy will be broken naturally due to imperfections in cavity machining or thermal contraction while inside the DR. If this is not the case, however, certain elements of cavity construction exist that will ensure that the two modes do not overlap. The most straightforward method involves a protruding (receding) end-cap rim that increases (decreases) effective cavity length for the TM_{111} mode but not the TE_{011} mode. A graphic depicting this scenario as well as the frequency shift response of each mode is shown below in Fig. 3.4. A further strategy for heavily attenuating the TM_{111} mode involves integration of a piston-like end-wall which can also be used as a cavity tuning mechanism if used in conjunction with a bimorphic PZT as shown in Fig. 3.5 (this work is elaborated on and data is presented in section 6.1.2).

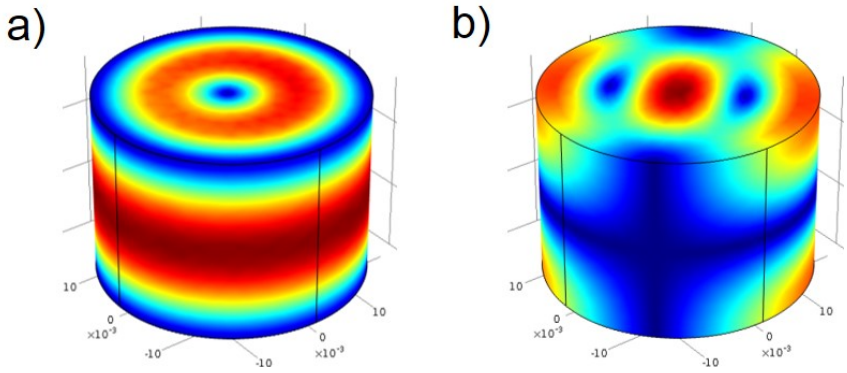

Figure 3.3: a) A COMSOL simulation displaying the surface magnetic field of the TE_{011} mode. This mode propagates along the central cavity surfaces and through the center of its volume. almost no field is located at the seams where the end-cap is connected to the cavity body. b) A COMSOL simulation displaying the surface magnetic field of the TM_{111} mode. This mode is degenerate with the TE_{011} mode but adversely affects Q since there are large concentrations of field near the end-cap seams.

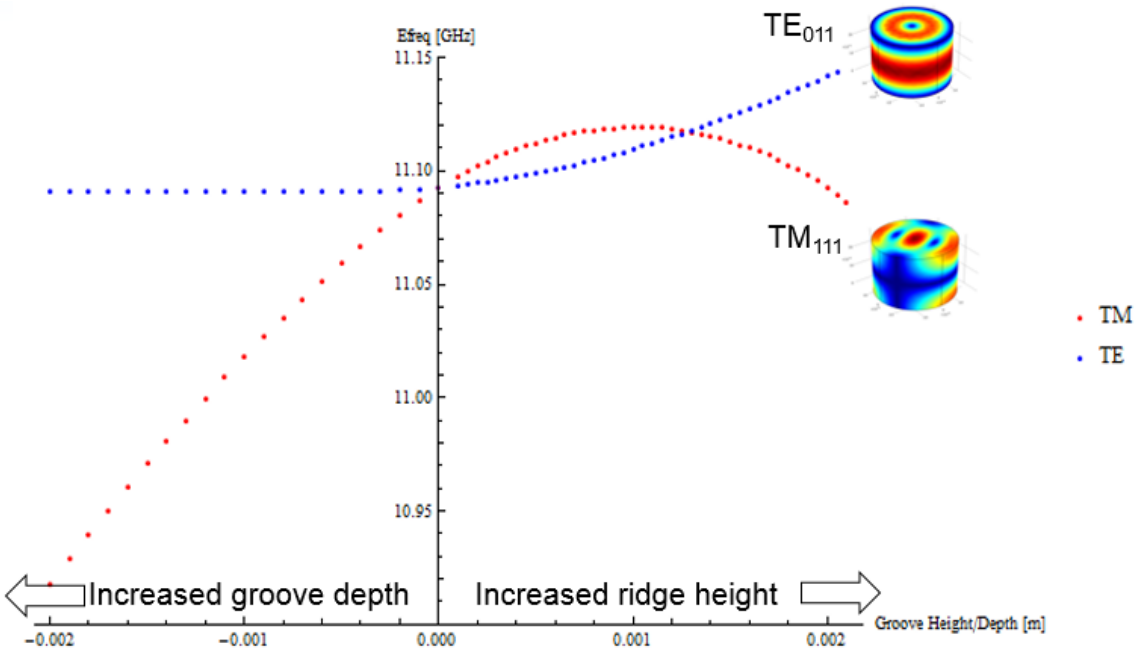

Figure 3.4: A graph demonstrating the effects of groove depth/ridge height on the resonances of the TE_{011} (blue) and TM_{111} (red) modes. As expected, the TE_{011} mode is not affected at all by a groove and minimally affected by a ridge as compared to the TM_{111} mode. It would appear that a groove is much more effective as a means of breaking degeneracy between the two modes.

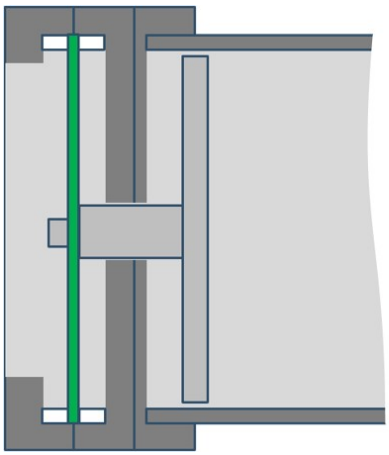

Figure 3.5: A cartoon demonstrating how a piston-like component is integrated into our cavities. The piston leaves a very small opening between its outer diameter and the inner diameter of the cavity wall (approximately 250 μm) which prevents currents driven by the TM_{111} mode from being supported. This effectively breaks the degeneracy between the TE_{011} and TM_{111} modes.

3.2 Machining

Ideally, one would be able to ask a professional machinist to machine a cavity to the exact specifications desired. This is not always feasible given certain laboratory locations and resources, so this section is here to outline the best way to machine a Nb SRF cavity.

Machining properties of Nb are similar to that of Cu or Pb in the sense that it is a soft, gummy material with a tendency to grab the tool during cutting if material build-up begins to exert too much pressure. It is also extremely dense like stainless steel so, needless to say, the machining process requires extra attention to detail. Gall prevention for this particular material involves proper lubrication and appropriate design of tool angles (Table 3.1) [29].

Lathe turning should use sharp, high-speed stainless steel (HSS) tooling with a small radius to prevent build-up of material on the cutting edge. We use an unconventional feed direction in machining cavity end-caps; instead of cutting from the outside in, we cut from the inside out in a shaving fashion. To keep the Nb cool during turning, we use a 6-10% Castrol Syntilo 9913 cutting oil (mixed with water) and apply with a vented wash-bottle during each cut. This step is extremely important as over-heating during machining will cause the Nb to react with gases in the air and chemicals in the cutting oil forming hydroxides that can seep into the cavity body below the surface. These impurities largely affect the resistance in the

Table 3.1: Table summarizing the tooling parameters for machining Nb [29].

Tool parameter	Value(s)
Approach angle	15-20°
Side rake	30-35°
Side and end clearance	5°
Plane relief angle	15-20°
Nose radius	0.5-0.75 mm (0.02-0.03 in.)
Cutting speed (with HSS) (with carbide tools)	0.3-0.4 m/s (60-80 ft/min) 1.27-1.75 m/s (250-300 ft/min)
Feed, roughing	0.2-0.3 mm/rev (0.008-0.012 in./rev)
Feed, finishing	0.12 mm/rev (0.005 in./rev)
Depth of cut	0.75-3.125 mm (0.03-0.125 in.)

cavity walls and cannot be easily removed. The correct speeds for given cuts must be found with trial and error as certain procedures require different techniques (although recommendations are given in Table 3.1). We finish the Nb turning with 300-400 grit sandpaper and finally a Scotch-Brite™ scorch pad. Machining Nb on the mill is less complicated as tooling does not need to be customized. It should be noted, however, to use slow feed rates and take small cuts as the material is still prone to galling and grabbing.

When drilling Nb, we use the deep hole drilling style and typically stick to speeds ranging from 1000-1500 RPM for #32 to #49 drill bits (we are typically drilling holes for 2-56, 4-40, and 6-32 screws). While center-drilling is usually recommended, it is absolutely necessary for Nb and should drill at slower speeds (700-900 RPM). We use Rapid Tap or equivalent cutting oil as lubricant during this process. Drill bits should be HSS and one should use a new drill each time for holes smaller than #49. Tapping these holes is perhaps the most delicate procedure as it is an extremely slow process. We use Rapid-tap cutting oil and we drill holes one number size larger (e.g. if it calls for #50, use #49 etc.) than those recommended for aluminum. It is recommended to use the mill for the first pass of tapping followed by a quick once-over by hand.

3.3 Etching and baking

3.3.1 Chemical polishing

Once the cavity has been machined, it is necessary to smooth its surface down to the microscopic (or smaller) scale to allow for the lowest surface resistance possible. This is due to the fact that machining Nb, in particular, has a tendency to smooth-over the material rather than cut and remove it. As such, anywhere from 10-100 μm of surface material is a mixture of Nb shavings and other contaminants such as oils and unwanted oxides/hydrides introduced because of heating during the machining process. One of the most efficient ways to dispose of the unwanted surface imperfections is through the use of chemical polishing (CP), introduced by Turneaure and Weissman in 1968 as a method for introducing high-Q, superconducting cavities into particle accelerators [30]. During CP, acids are used to strip away the surface material, thereby exposing a clean, smooth surface which is necessary when trying to minimize RF losses [30, 31]. The acids used originally were most likely hydrofluoric (HF) and nitric (HNO_3) acid, but it is now known, in our case from first-hand experience, that these acids react very strongly with Nb and have a tendency toward thermal run-away if not properly cooled during etching. This introduced the need for a buffering agent for safer and more controlled etching processes.

3.3.2 Buffered chemical polishing

The first use of a buffer in CP for SRF cavities occurred in 1970 when Kinter et al. discovered that the introduction of phosphoric acid (H_3PO_4) to the established solution served as a stabilization agent which allowed for control over the etch rate and reduced heating in the reaction [32]. In Kinter's work it was found that two different BCP solutions, 1:1:1, and 1:1:2 (HF, HNO_3, H_3PO_4 by volume, respectively) gave similar (as resolvable by a light microscope) results in regards to the quality of the surface finish. From their work these two ratios of BCP solution have become commonly used in Nb surface treatment. It has now been found that the 1:1:2 BCP solution gives more uniform results, and has become more of a standard in the SRF cavity community [33]. This is the BCP method we have adopted for the U.C. Merced SRF laboratory.

3.3.3 BCP at U.C. Merced

The BCP solution used at U.C. Merced consists of all ACS grade acids. Specifically, we use 48-51% HF, 68-70% HNO_3, and 85-87% H_3PO_4. As mentioned in the previous section, these acids are used in volumetric proportions of 1:1:2, respectively. ACS-grade acids are cost-effective, moderate quality, and specify

their impurities down to the level of parts per million (ppm). Ultra-grade acids significantly increase in cost but can specify impurity levels down to the level of parts per billion (ppb) or parts per trillion (ppt).

In Tereshkin's work, it is stated that the BCP reaction rate depends on the concentration of dissolved Nb in the solution [34]. It has been reported that for acceptable surface quality the concentration of Nb in the solution should not surpass 15 g/L [35]. As a safety factor, we can set a limit of 10 g/L for the concentration of Nb that has been dissolved in the solution. It is reported that for this concentration, one liter of BCP solution is required to remove 1 μm for each m^2 of surface area treated [34], from which we can write the following ratio

$$\text{BCP solution [L]} > \frac{1L}{1\mu\ 1m^2} \times A \times l \tag{3.1}$$

where A is the surface area in m^2 to be etched, and l is the amount of niobium to be removed in μm. Additionally, there are safety concerns regarding byproducts produced in the chemical reaction during BCP, so it is strongly recommended that any non-professional peruse the following references before attempting to etch Nb cavities themselves [34, 36–39].

BCP at U.C. Merced has become a normal part of the SRF cavity building procedure. We can see the difference that etching makes in surface quality in Fig. 3.6 below. In our experience, etching the cavity body and end-caps usually leads to an increase in Q of approximately 1-2 orders of magnitude. It took some trial and error to achieve good surface finishes and reliable etching rates. Several iterations of etching procedures were attempted before choosing a final method.

All procedures involved mixing and pre-cooling an appropriate amount of solution before the etch. It is also imperative that etching take place in a fume hood or similar environment as the byproducts produced during the procedure are not safe for human inhalation. We monitored the temperature of the reaction by placing a calibrated voltage thermometer in the BCP solution and recording the temperature every 5 minutes. If the temperature ever exceeded 15 °C, we terminated the etch. Continuing to etch at temperatures greater than 15 °C runs the risk of excess hydrogen contamination and thermal run-away.

The first method attempted was dubbed the "dunking method;" and it is named quite aptly. The BCP solution was contained to a Teflon beaker, the Nb was held in place with a clamp, and its surface was lowered into the beaker until making contact with the solution. We soon realized that it was too difficult to control the temperature of the reaction in this way as demonstrated in Fig. 3.7. The thickness of the orange smoke wafting from the reaction signifies an etching rate and BCP solution temperature well outside optimal levels. This may not be due entirely to the method in which we attempted to etch the material (this was the first attempt overall), but it became clear that we needed to take greater care in ensuring the solution and Nb piece are both kept cool.

The next method involved attaching the Nb component to a Teflon tube with screw, sealing the joint with Teflon tape, and pouring the BCP solution into the resulting cup-like structure(Fig. 3.8). We call this the "cup method." It is much easier to control the temperature of the reaction in this way since the metal is in direct contact with the ice bath. As such, no thermal run-away occurred while utilizing this method. A problem arose, however, in that gravity caused the etched material to settle at the bottom of the cup where the Nb is held in place. This prevented further Nb from being etched as efficiently and subsequently adversely affected etching uniformity. This problem only affects our Nb end-caps as the cavity body is oriented vertically and etched material does not settle along its surface.

Lastly, we devised a method similar to the "cup method" but rotated such that the etched material does not settle onto the Nb surface. First, we drilled a hole through the side of a Teflon tube. Next, we attached a Nb end-cap to each side of a Teflon tube using screws and Teflon tape and then turned it onto its side. This created a container for the BCP solution that we call the "vertical method" (Fig. 3.9). Again, the metallic components are placed directly in the ice bath which allows for excellent control of temperature and etch rate. No thermal run-away was observed while utilizing this method. Fig. 3.10 displays the surface finish for each method described in this section.

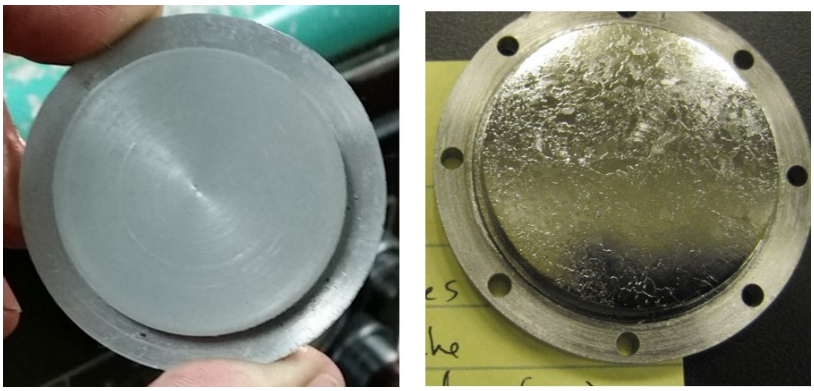

Figure 3.6: (Left) A finished, sanded Nb end-cap component before undergoing the BCP procedure. The metal appears to lack any sheen and machining marks are still apparent. (Right) A photograph of an end-cap after undergoing the BCP procedure. Note the newfound metallic luster and the now exposed grain structure. The unwanted, smoothed-over detritus was etched away after removing less than 100 μm.

Figure 3.7: A photograph demonstrating the "dunking method" of etching in which the BCP solution is contained within a Teflon beaker which is in turn placed in an ice bath in an attempt to control the temperature of the reaction. As evidenced by the orange smoke, this method is prone to thermal run-away even when taking necessary precautions due to the large surface area that is exposed to the BCP solution.

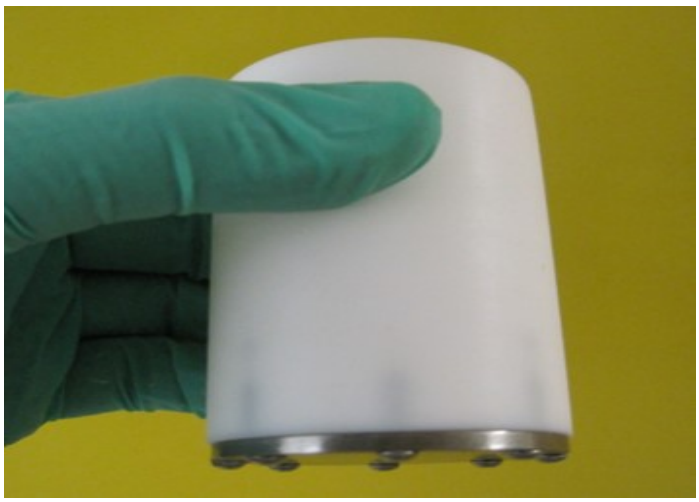

Figure 3.8: A photograph demonstrating the "cup method" of etching in which a Teflon tube is fitted to the exact specifications of the end-cap, attached with screws, and made leak-proof with a Teflon tape seal. This method circumvents thermal run-off by allowing the cap to sit in the ice bath, thereby ensuring an extremely controlled etch. The only problem with this method involved the etched material settling at the bottom of the container and preventing the BCP solution from effectively etching the cap further.

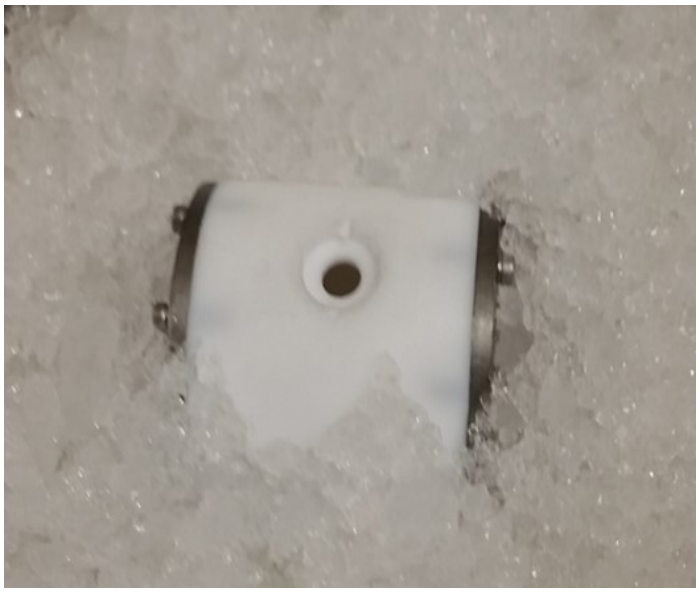

Figure 3.9: A photograph demonstrating the "vertical method" of etching in which a Nb end-cap is affixed to each end of a Teflon tube in the same manner as described in Fig. 3.8. A hole is drilled into the side of this Teflon tube and it is then laid onto its side so that the BCP solution can be poured into the hole. This method is an attempt to mitigate the problem of material settlement described in the "cup method" BCP summary.

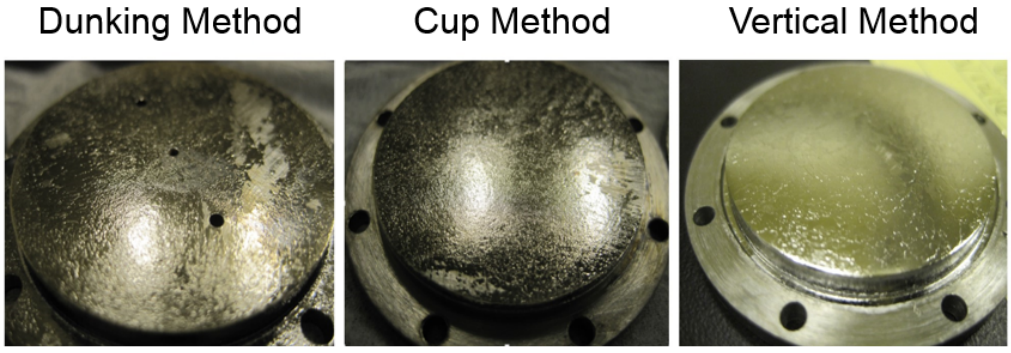

Figure 3.10: The finishes for each etching method described in this section. The vertical method appears to provide the best finish for end-caps.

3.3.4 Baking of cavities and cavity components

Once the cavities and cavity components have been etched, it is necessary to bake them to eliminate the final contaminants that have built up in the surface or perhaps deeper in the material. The bake should reach temperatures of approximately 600-800 °C for approximately 10 hours in a high-vacuum environment [40]. Recent experiments have also shown that a 100-150 °C "*in situ*" bake under ultrahigh vacuum as a final step demonstrates a general improvement in Q [41]. Without high-vacuum, the gases will simply reabsorb into the metal after cooling back to room temperature. U.C. Merced does not have a furnace capable of reaching the required vacuum specifications so we sent the components to our colleagues at Jefferson Labs in Virginia. Scientists at Jefferson Labs specialize in SRF cavities for particle accelerators and have decades of experience in treating Nb for superconducting applications. While etching and baking are important to maximizing a cavity's Q, it is important to note that it is possible during the etching process to contaminate Nb beyond the point that baking will effectively remove contaminants.

3.4 Alternative design: quarter-wave stub cavity

In struggling to obtain a high enough Q with cylindrical cavities, subsequent cavity designs have been explored. The quarter-wave stub cavity stood out because of its geometry which requires no assembly. It is just a solid piece of metal with an exposed opening at one end that allows the field to decay. This geometry is appealing because the seams that form near the end-caps in the cylindrical cavity are the most likely cause of losses in that system. Stub cavities also do not appear to support any degenerate modes that inhibit large Q. Therefore, we designed and tested several stub cavity prototypes at room temperature.

We machined three of these cavities to the same dimensions but with different materials: Al, Cu, and Nb. These were machined by first boring out to the location of the stub and then moving to a computer numerical control (CNC) machine to finish the stub itself. We used an end mill that had a small radius and long arm as the stub cavities are extremely narrow and deep. A drawing of a quarter-wave stub cavity along with its supported modes is shown below in Fig. 3.11.

We took reflection measurements for each cavity and plotted them to observe stub cavity behavior at room temperature (Fig. 3.12). The tests demonstrated that it is exceedingly easy to couple to stub cavity modes compared to cylindrical cavities. Further, stub cavities can be machined with relative ease since they are one solid piece of metal as opposed to other cavities which require machining and assembly of several cavity components. Unfortunately, it is not possible to predict the exact resonance of the cavity as with the cylindrical geometry. This is due to the

fact that there is no exact solution for the resonance equation of these cavities [42]. Regardless, the resonance can be very roughly approximated because these are quarter-wave stub cavities. Stub height will affect the resonance more directly as compared to its radius or the radius of the cavity. Attaining the desired resonance can then be achieved by tuning the cavity. The benefits of these stub cavities vastly outweigh the negatives, so they have become a main area of study in the lab.

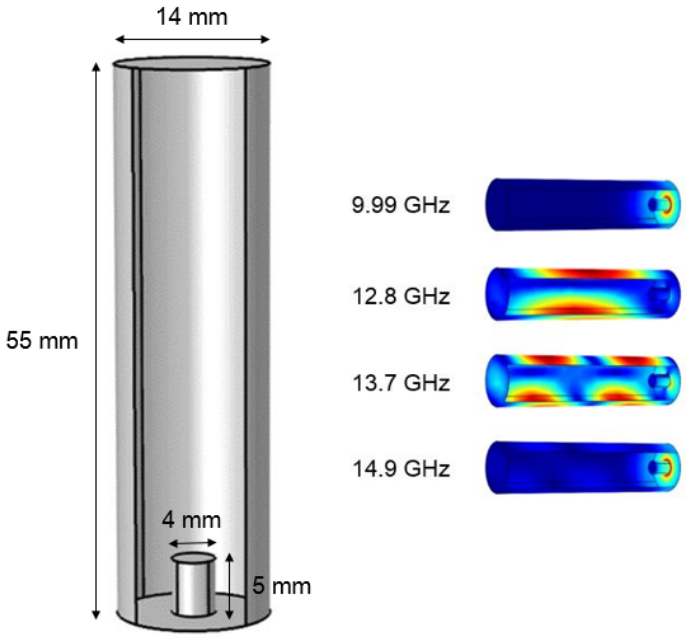

Figure 3.11: (Left) A drawing corresponding to our stub cavity prototypes. (Right) COMSOL simulations illustrating surface magnetic fields corresponding to supported electromagnetic modes. The frequencies listed correspond to these specific dimensions of the cavity. The appeal of these cavities lies in their lack of mechanical seams and ease of coupling which arises from disparate mode location. We will use the 10 GHz mode for experiments as this mode is expected to have the highest Q.

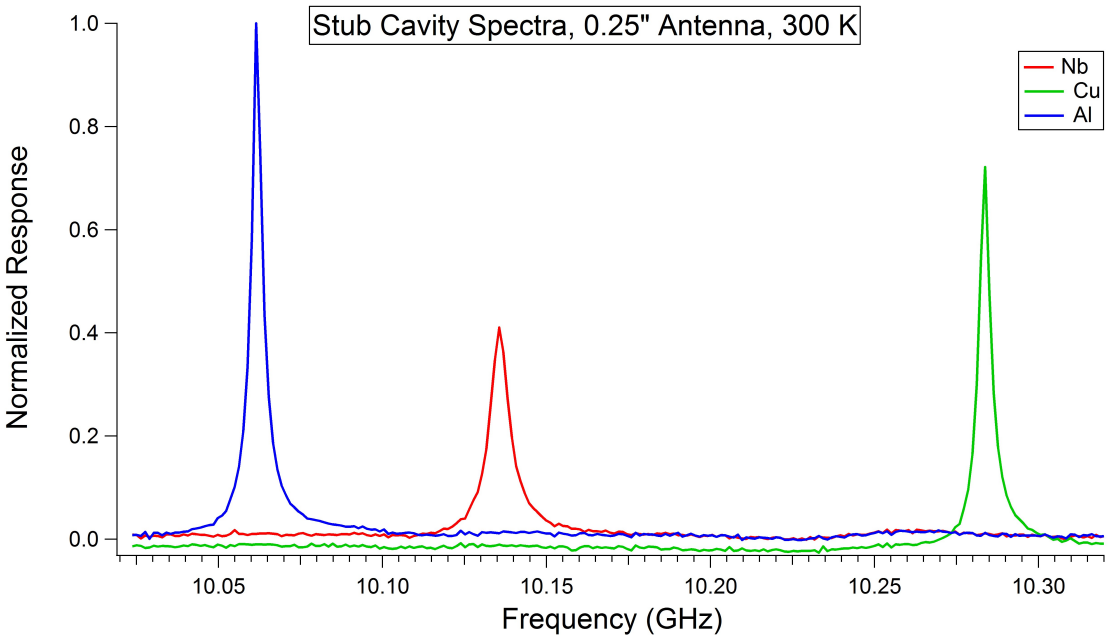

Figure 3.12: Normalized spectra for all three of our prototype stub cavities. We intend to eventually coat the Al and Cu cavities with Nb and test for high-Q. The Nb cavity will be tested for high-Q as well.

Chapter 4

Tests and results of superconducting cavities

We test our cavities at room temperature in order to ascertain mode resonance location, but most relevant tests take place in a cryogenic environment. Knowing where modes exist in frequency space at room temperature makes measurements below 1 Kelvin much easier to perform. This, in part, is due to the fact that resonances drift slightly in the cool-down process because of thermal contractions in the material. Small changes to cavity dimensions change effective cavity volume and, therefore, cavity resonance. Combine this with the fact that resonances with Q factors of 10^8 or higher have linewidths on the order of 100 Hz for our cavities and it becomes apparent that these signals have the potential to be very difficult to find. Measurement techniques will be outlined further later in this chapter.

We cool our samples utilizing a Oxford Triton 200 dilution refrigerator (DR) capable of reaching temperatures as low as 40 millikelvin. We use brass or copper components in fastening the cavities so as to avoid stray magnetic fields inside the sample cage as they could interfere with the Nb's superconducting properties and affect Q measurements. A photograph of our system can be seen in Fig. 4.1 below. We use SubMiniature version A (SMA) cables to transmit electrical microwave signals into and out of the DR. We use Pamtech cryogenic circulators (model XTE0812KC: 8-12 GHz) to separate these incoming and outgoing signals and subsequently observe reflection measurements in addition to transmission measurements depending on our coupling scheme of choice. These circulators are magnetic, but we avoid magnetic field contamination of the cavities by placing the circulators above the 4 K plate of the DR. We have measured magnetic field strength in the sample chamber and found that there is no magnetic field present near our cavities during experiments.

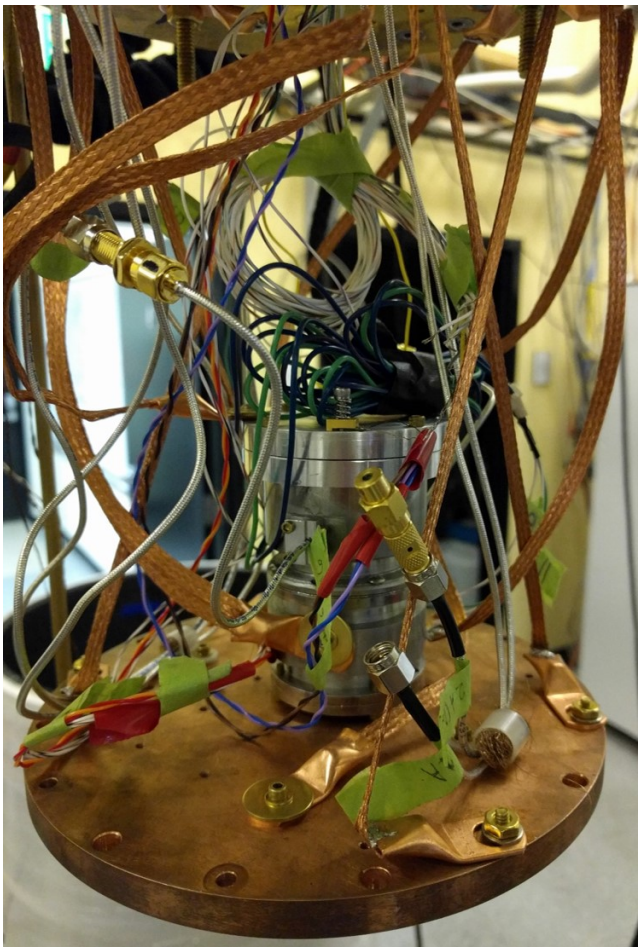

Figure 4.1: A photograph of the sample container space where we place our cavities for cryogenic testing. The SMAs feed through the plates separating temperature stages of the DR and connect to the cavity input/output couplers. Copper braids are attached to the cavity body and act as thermal anchors to ensure heat exchange takes place as the system is under vacuum during testing.

4.1 SRF cavity measurements

4.1.1 Reflection (S11) and transmission (S21) measurements

Scattering parameters (S-parameters) identify the nature and direction of microwave signal measurements. One typically speaks of S-parameters when discussing measurements involving sending a microwave signal across one or more antennas, or ports. Depending on the S-parameter, an antenna can transmit and/or

detect a microwave signal. We never utilize more than two ports in our experiments so I will limit discussion of S-parameters to these two cases. Fig. 4.2 demonstrates a very basic understanding of the convention for which two-port S-parameters are labeled.

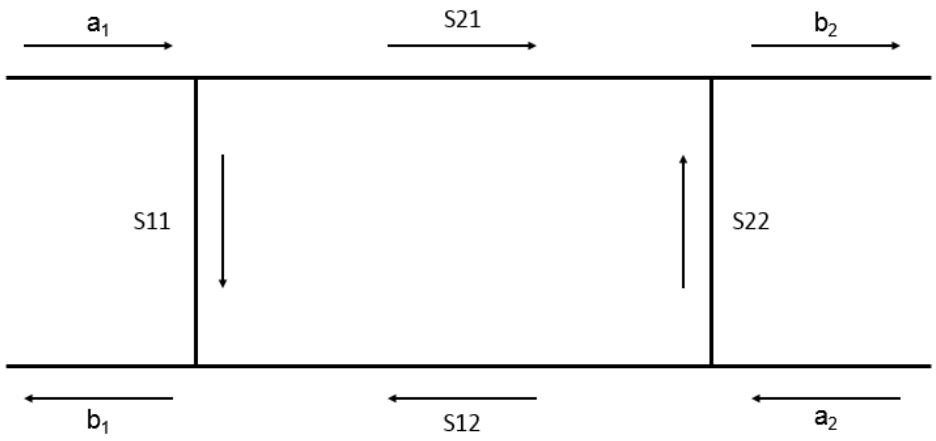

Figure 4.2: A diagram of outgoing (a_n) and incoming (b_n) power waves in a two-port microwave circuit. The S-parameters follow the labeling convention $S n_b n_a$ where n represents the port number, a is a wave leaving the port, and b is a wave going into the port. We are only interested in reflection (S11) and transmission (S21) measurements. That is, we use the output signal from port 1 to measure the cavity reflection spectrum at port 1 or the cavity transmission spectrum at port 2.

Defining the outgoing power waves as a_1, a_2 and the incoming power waves as b_1, b_2 where the subscript denotes the source port, we see the following relationship

$$\begin{pmatrix} b_1 \\ b_2 \end{pmatrix} = \begin{pmatrix} S11 & S12 \\ S21 & S22 \end{pmatrix} \begin{pmatrix} a_1 \\ a_2 \end{pmatrix} \tag{4.1}$$

where we have incorporated the S-parameter matrix. For our measurements, this means that a_1 is the signal traveling from port 1 to the device under test (DUT) and b_1 is the reflected signal traveling from the DUT back to port 1. The values a_2 and b_2 would then follow the same convention but for port 2. This leads to the relationships

$$\begin{aligned} b_1 &= S11a_1 + S12a_2 \\ b_2 &= S21a_1 + S22a_2 \end{aligned} \tag{4.2}$$

wherein the S-parameters are found given the loads from the corresponding incoming and outgoing power waves. A reflection measurement assumes termination of the port 2 load (e.g. a_2=0), so S11=b_1/a_1 and S21=b_2/a_1.

4.1.2 Coupling

Coupling to one of our cylindrical cavities involves placing a loop antenna into a small coupling hole that has been drilled through the cavity wall. Our antennas are made by soldering a thin wire to the central connector of an SMA panel mount jack. The wire is then bent into a loop after sliding a short plastic sleeve down to the solder joint to prevent a potential short-circuit. The free end of the wire is left so that it will push against the inner coupling hole wall when mounted. The length of the loop is currently determined by trial and error with the goal being a superconducting cavity that is critically coupled via evanescent wave at approximately 1 K (see section 4.1.4 for more on coupling parameters).

An SRF cavity coupling design is almost entirely determined by the mode one is interested in observing. Cavities sustain many modes across a broad bandwidth so it is important for one to know which mode they wish to measure before beginning coupler design. In our cylindrical pill-box cavities, we would like to measure the TE_{011} mode so we must consider mode shape and field strength at different surface locations. Referring back to Eq. 2.1, we see maximum B-field concentration at $L/2$ of the cylindrical wall and at radius $0.48R$ of the end-wall. Coupling to locations of strongest surface B-field allows for stronger evanescent wave coupling to the very small holes we use as sub-cutoff circular waveguides. The antennas must be recessed from the actual cavity volume so as to influence the intrinsic quality factor as little as possible. The evanescent wave decays as

$$E \propto e^{-\alpha_{TE_{mn}} x} \tag{4.3}$$

where $\alpha_{TE_{mn}}$ is the mode propagation constant and x is the distance the field has propagated through the coupling hole. The mode propagation constant for a TE_{mn} mode takes the form

$$\alpha_{TE_{mn}} = \sqrt{\left(\frac{x'_{mn}}{r_0}\right)^2 - k^2} \tag{4.4}$$

where k is the wavevector, and r_0 is the radius of the coupling hole [42, 43]. This constant is real when

$$\omega < \frac{x'_{mn} c}{r_0} \tag{4.5}$$

where c is the speed of light in vacuum. Below this cutoff frequency, the field must evanescently decay into the coupling hole. This mode decays exponentially through the waveguide and seeds radiation into the cavity in the form of the TE_{011} mode.

4.1.3 Cavity mode mapping

After prototyping each cavity, we made sure to take a reflection spectrum in order to document the location of each mode before undergoing SRF experiments. The shift in frequency from thermal contractions combined with the narrow linewidth of the resonance after the superconducting transition makes tracking resonances after cool-down difficult. Having the mode map and a general idea of frequency shifts during the cool-down allows one to find the resonance of the cavity more efficiently. Fig. 4.3 displays the resonances of the modes in one of our cylindrical cavities across a bandwidth of 9 GHz. We make maps such as these for each prototype cavity before placing them in the DR for experimentation.

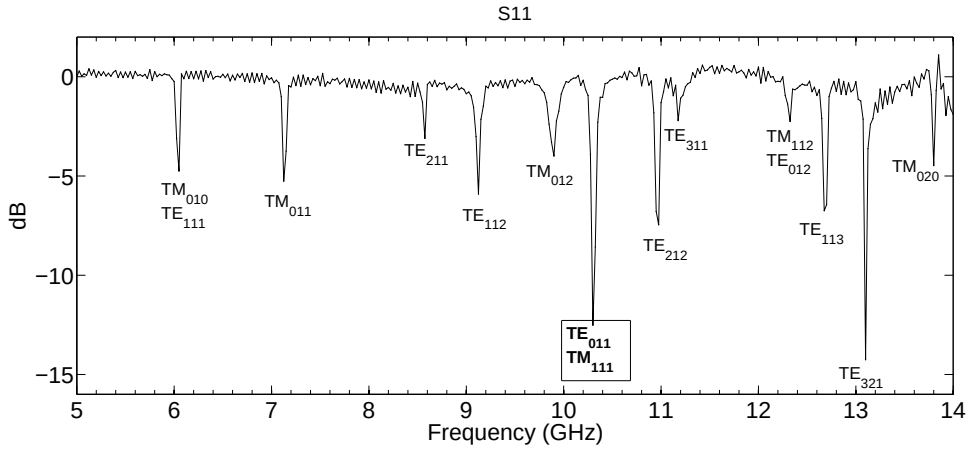

Figure 4.3: S11 measurement showing the mode resonances for one of our cavities. The TE_{011} mode resonance frequency is 10.332 GHz. The degenerate TM_{111} is slightly shifted by adding a small gap at the end-cap of the RF cavity. The relevant dimensions are $D = 3.81$ and $L = 3.81$ cm [44].

4.1.4 Measuring Q

Q measurements typically involve searching for the cavity's resonance followed by seeding an electromagnetic pulse centered at that frequency into the cavity. This is done using an Agilent N5183A RF signal generator and an oscilloscope triggered to an external function generator. We frequency modulate the RF signal and scan near the room temperature resonance until we see a response on the oscilloscope. After locating the approximate resonance frequency, we pulse the signal and scan the frequency in smaller increments until we see a refined pulse signal. Examples of oscilloscope traces for these processes are shown in Fig. 4.4.

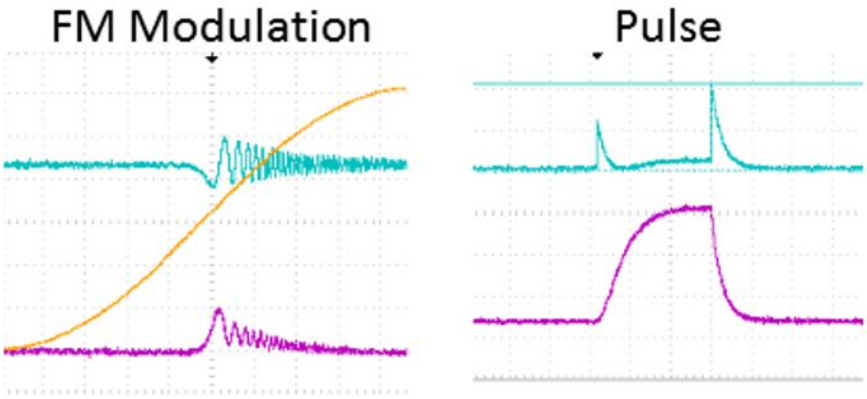

Figure 4.4: (Left) FM modulation of the incoming RF signal for S11 (blue) and S21 (purple) measurements. The signal decays as it continuously overlaps with the cavity resonance. (Right) A pulsed RF signal for S11 (blue) and S21 (purple) measurements.

We use a Schottky diode (model DHMA18AB: 10 MHz-18.5 GHz) to convert the power from the SMA cable to a voltage via BNC connected to a source meter.

The decay time is found by fitting an exponential decay

$$V = e^{-t/\tau_L} \tag{4.6}$$

to the pulse's tail and extracting the time constant τ_L. The intrinsic Q, referred to as Q_0, is defined as

$$Q_0 = \omega_0 \tau_L \left(1 + \beta\right) \tag{4.7}$$

where ω_0 is the resonance of the cavity and β is the cavity's coupling coefficient. Fig. 4.5 shows a standard S11 pulse displayed on an oscilloscope. The heights of the incoming and outgoing signal pulses are a function of coupling strength and they are denoted as (from left to right) P_f and P_e. P_f is related to the power that does not couple into the cavity, while P_e is related to the amount of power that does couple. When critical coupling is achieved, the forward traveling power, P_f, is completely absorbed into the cavity and $P_f = P_e$. In general, β is given by

$$\beta = \frac{1}{2\sqrt{\frac{P_f}{P_e}} - 1}. \tag{4.8}$$

where a value larger than 1 is considered over coupled, a value smaller than 1 is under coupled, and a value approximately equal to one is critically coupled. An example of this type of calculation can be seen by again directing our attention to Fig. 4.5. In the oscilloscope image, P_f is approximately 50 mV and P_e is approximately 40 mV. Using Eq. 4.8 gives $\beta = 1/(2\sqrt{\frac{50}{40}} - 1) = 0.81$. Having a $\beta < 1$

corresponds to an under coupled cavity which agrees with the fact that $P_f > P_e$ in the figure. Calculating the intrinsic Q of the cavity allows us to determine whether the overall quality of the cavity is suitable for further experimentation.

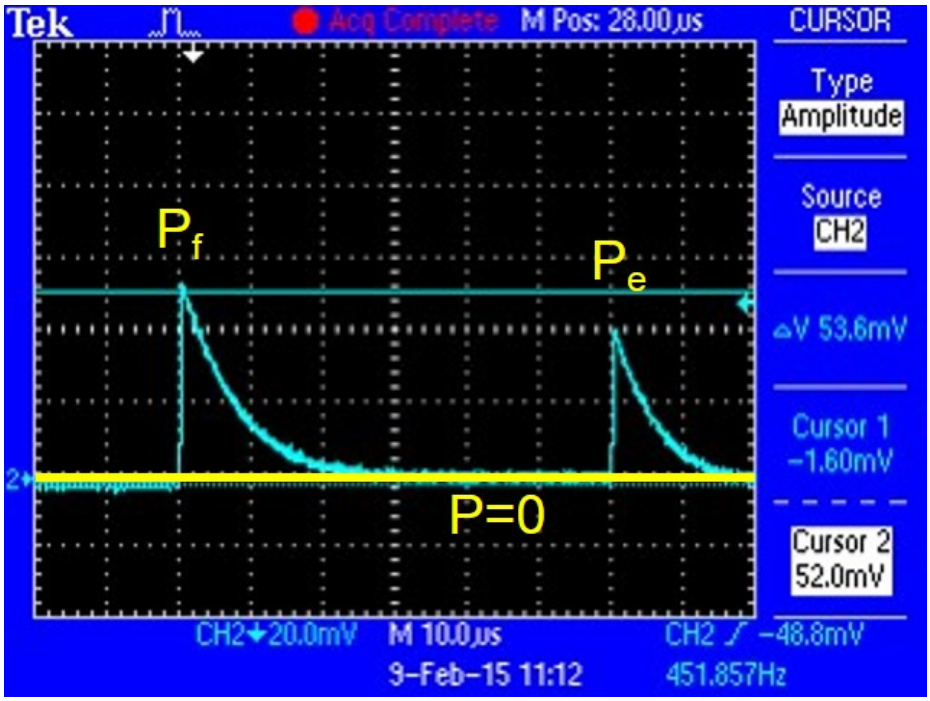

Figure 4.5: The reflected (P_f) and emitted (P_e) power wave peaks used in determining β for the individual coupling parameter in an S11 measurement. The values are taken with respect to the relative zero power level of the pulse in the region between both peaks and are then plugged into Eq. 4.8.

4.2 Cavity prototyping at U.C. Merced

We designed and machined several iterations of cylindrical Nb SRF cavities over the years. Each iteration after generation 1 underwent some form of BCP treatment but the method for BCP became more refined as time went on (see section 3.3 for more on this process). Some components from generations 2 and 3 were baked at Jefferson Labs, but only the highest Q values regardless of end-cap and body configurations are reported in detail. We began with commercial grade tube stock with input and output couplers held in place on the top end-cap (Fig. 4.6a). Results were consistent with the cavity initially commissioned from a third party (500,000). This is most likely due to the fact that cavity mechanics and construction were still very unrefined at this point.

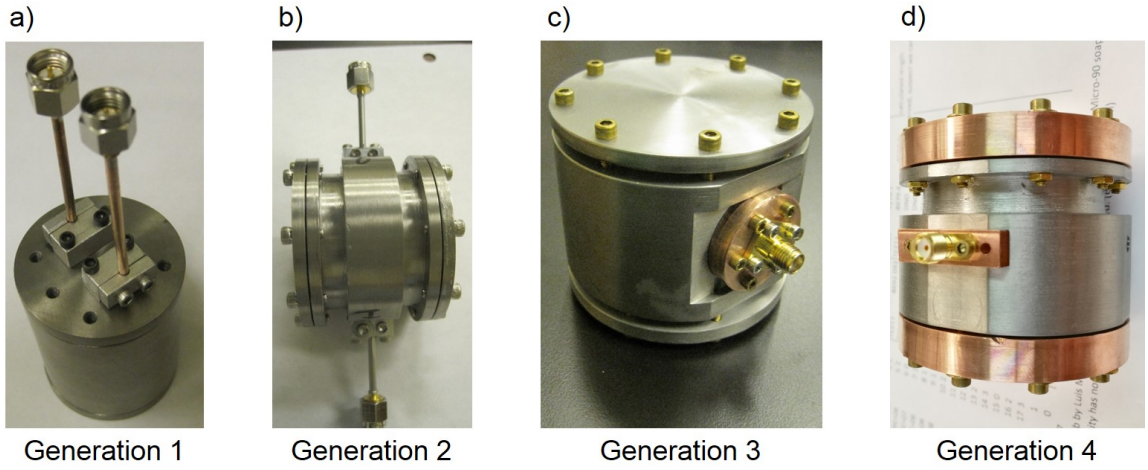

Figure 4.6: a) Generation 1 cavity machined from commercial grade Nb tube stock. b) Generation 2 cavity machined from reactor grade Nb. c) Generation 3 cavity machined from RRR grade Nb. d) Generation 4 cavity

Generation 2, machined from reactor grade Nb, saw the introduction of the bolt-hole pattern (BHP) method of attaching the end-caps to the cavity body (Fig. 4.6b) as well as the first prototype to undergo BCP and baking. We moved the input and output couplers to the sides of the cavity with their dipole moments oriented in such a way as to couple to the peak magnetic field present at the inner surface. Unfortunately, these improvements did not see any considerable raise in the cavity Q.

We began to question whether the end-caps were achieving good ohmic contact with the cavity body, so we introduced a groove along the inner rim for indium (In) seals in generation 3. Additionally, we re-worked the coupler mount to achieve better vacuum-sealing for the interior of the cavity and general coupler attachment issues. Namely, the new mount allowed for fixed coupler insertion length and subsequently took the guesswork out of cavity coupling.

Generation 4 introduced tighter machine tolerances and Cu plates which encompass the Nb end-plates and compress them onto the cavity body for better contact. This cavity also saw an increase in the number of screws used in the BHP. Generation 4 lead to another increase in Q by an order of magnitude without etching or baking. We present the maximum values of Q for each generation of cylindrical cavity and both Nb stub cavities (S1 and S2) in Table 4.1. These were measured utilizing the methods outlined in section 4.1.4.

Table 4.1: Q values for each generation of Nb cylindrical cavity as well as both Nb stub cavities (S1 and S2) that were etched and baked at Jefferson Labs

Cavity	β	τ (μs)	Freq. (GHz)	Q_0
Commissioned from 3rd party	0.6	4.62	11.63368	5.0×10^5
(Gen. 1) Reactor grade tube	0.5	4.04	9.85468	4.5×10^5
(Gen. 2) Reactor grade 8-hole BHP	10.88	29.7	11.01285	2.4×10^7
(Gen. 3) RRR 8-hole BHP	1.29	386	10.51171	5.8×10^7
(Gen. 4) RRR 10-hole BHP	12.3	179	10.46668	1.6×10^8
Reactor grade $\lambda/4$ (S1)	2.3	7,300	10.19863	1.7×10^9
Reactor grade $\lambda/4$ w/defect (S2)	2.12	1,166	10.51061	2.4×10^8

Chapter 5

Silicon nitride membranes and their role in optomechanics

5.1 Examples from literature

The use of light, flexible membranes as mechanical oscillators has been well-documented as a means of observing cavity resonances based on mechanical oscillator behavior. For example, Bui et al. measure optical reflectivity in high Q factor membrane resonators using mechanical ringdown measurements after driving their membrane with a 1064 nm laser [45]. The goal in our Fabry-Pérot cavity is to drive a mechanical oscillator using microwave frequency radiation, so a membrane setup is most feasible in the immediate scope of the project. Silicon nitride (SiN) membranes typically consist of a 100-300 nm SiN film deposited onto a silicon (Si) wafer substrate. The structural integrity of the film is maintained through the substrate providing some amount of tensile stress. These films have been deemed excellent substrates for many varieties of material deposition including polymers [46], metals [47], and even biological tissues [48] due to their chemical inertness and ability to endure thermoelectric extremes.

The large surface area of the membrane ensures that it will couple to the cavity [49] and our ability to fabricate at small thicknesses ensures a very small charge-to-mass ratio. There are three classifications of modes that can be excited in the membrane by the microwave frequency radiation: flexural, dilational, and tensional modes. Flexural modes consist of drumhead-like oscillations that offset the radial and angular components of the membrane. Dilational modes are comprised of oscillations that vary the membrane's thickness. Finally, tensional modes, as the name implies, arise from fixed boundary conditions along the membrane's outer edges that cause its surface tension to oscillate. These modes have been studied in great detail [7, 50] in regards to the membrane's geometry. The Q factor of these membrane structures can range anywhere from 10^3-10^5 at room temperature

depending on the material used and the size of the structure [49, 51]. That is, smaller structures made of more rigid materials will tend to have larger Q.

5.2 Structure

A particularly thorough description of creating a SiN membrane is given in a paper written by Morkved et al. in 1998 [46]. Both sides of a double-side-polished $\langle 100 \rangle$ Si wafer of desired thickness are prepared by first stripping the silicon dioxide (SiO_2) layers. Here, the $\langle 100 \rangle$ refers to the crystalline grain structure of the material and is important for the purposes of etching and photoresist. Next, amorphous, low-stress SiN is deposited onto both sides in a low-pressure environment. Photoresist then creates the patterns for the membrane while SiN is removed via reactive ion etching with tetrafluoromethane (CF_4). The exposed Si is etched with an aqueous potassium hydroxide (KOH) solution which etches the $\langle 100 \rangle$ and $\langle 110 \rangle$ planes faster than the $\langle 111 \rangle$ plane. This causes the Si layer to etch away without affecting the front-side SiN layer whose size is determined mainly by geometry and the size of the starting hole.

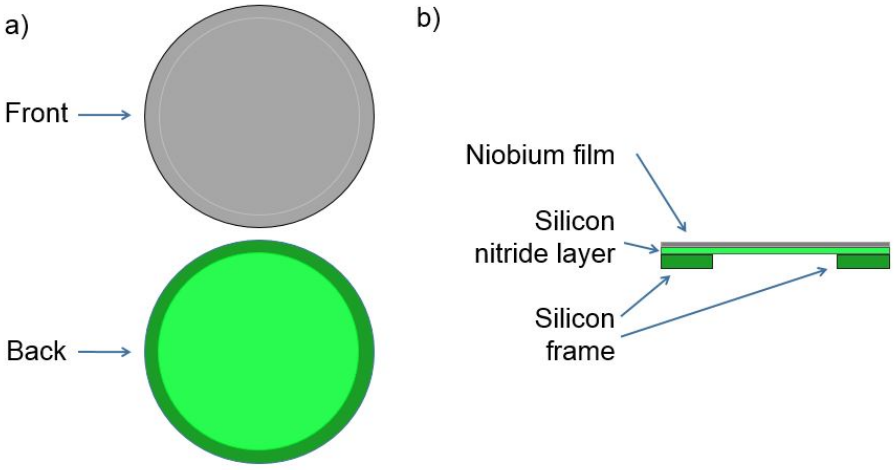

Figure 5.1: Not drawn to scale: a) Depictions of the front and back sides of the SiN window. The front side is coated with Nb while the back side shows the difference between the Si frame and the suspended SiN film. b) A "slice" of the SiN window. The Si frame is 51 mm O.D., the SiN film is 500 nm thick and 38 mm wide, and the Nb film is 300 nm thick.

We are further interested in SiN membranes that have been sputter-coated with Nb since the membrane will act as a superconducting boundary for the purposes of

generating gain in our superconducting cavities. This structure is illustrated above in Fig. 5.1. As such, the quality of the Nb film must be sufficient to produce cavities with an oscillating boundary that maintains the high Q of a solid cavity. We obtained two distinctly different samples of Nb-coated SiN membranes by sputtering our own windows at Marvell Nanolab in Berkeley and ordering them from a MEMS company named Norcada.

5.3 Niobium film analysis

We wish to incorporate a high-quality Nb film into an SRF cavity of our own design. Before we can do this, we need an idea of how well the film will perform once superconducting. Obtaining a value of the residual resistivity ratio (RRR) for our film will give us some indication of its performance once integrated into the cavity. RRR is an accepted figure of merit for superconducting film quality and is obtained by taking the ratio of the film's resistivity at room temperature to its resistivity right before it goes superconducting. Films were evaluated by attaching leads to appropriate locations around their Si frames. They were then placed in a helium (He) dewar which cooled the films to below their critical temperature while we measured the resistance across them. Resistivity is an intrinsic property of a material that determines how well current can flow in said material. The reasons for the difference in resistivity across different substances lie in their material properties. Specifically, in metals, we can more or less attribute the majority of an object's resistivity to electron-electron or electron-phonon interactions within the material. Therefore, finding the RRR of the film is a straightforward approach to determining a film's purity and will aid us in determining which films are suitable for cavity integration.

Superconducting transition measurements were performed using two Norcada SiN windows sputtered with Nb during the same deposition at Norcada and two Norcada SiN windows sputtered during the same deposition at Marvell Nanolab in Berkeley. The main difference between the two "Berkeley" samples is that one membrane ruptured during the sputtering process while the other did not. These samples are termed "failed berkeley sample" and "successful berkeley sample," respectively. The Norcada sample windows consist of a 10x10 mm, 500 μm thick silicon frame and a 5x5 mm, 500 nm thick SiN window with a 300 nm thick sputtered Nb film. It is important to note that the membranes sputtered by Norcada were sputtered during the same deposition as the large 38 mm SiN windows that we eventually attach to our cavity. In this respect, the "Norcada samples" are representative of the superconducting properties of the 38 mm nitride windows. The "Berkeley" membranes are identical in dimension with the exception of their 300 nm Nb films sputtered at Berkeley and 100 nm thick nitride window.

We performed four-lead measurements with a Keithley 2400 source meter and a

LabView VI. We attached electrical contacts (4-lead) to the window frame in an in-line configuration and cooled the samples to approximately 4.5 K in cryofab dewar (#1). We obtained data for resistance vs temperature (RT) curves and voltage vs current (VI) curves which are plotted in Figs. 5.2, 5.3, and 5.4. All tests confirm the presence of a superconducting transition of the Nb films sputtered on the surface of the membranes. Transition temperatures ranging from 8.3 ± 0.1K$- 9 \pm 0.1$ K for the Norcada samples, and 9 ± 0.1 K for the Berkeley samples were recorded.

The high transition temperature and voltage vs current measurements of the Nb superconducting films from Norcada and Berkeley indicate that the films are of relatively good quality. The RRR values for these films are approximately 2.55 for the Norcada sample and 4.39 for the Berkeley sample. Nb films are known to have a lower RRR than bulk Nb (bulk Nb RRR is usally grater than 250) [52], but even films have demonstrated RRRs of 10 or higher [53, 54]. This tells us that our films are not of extremely high purity, but should be sufficient for SRF experiments. For the purpose of achieving high-Q SRF cavities, more tests should be performed. The next steps are to incorporate the large Norcada membranes into our RF cylindrical cavity design, perform Q measurements, and implementing a measurement scheme in which the London penetration depth of the Nb superconducting films can be measured.

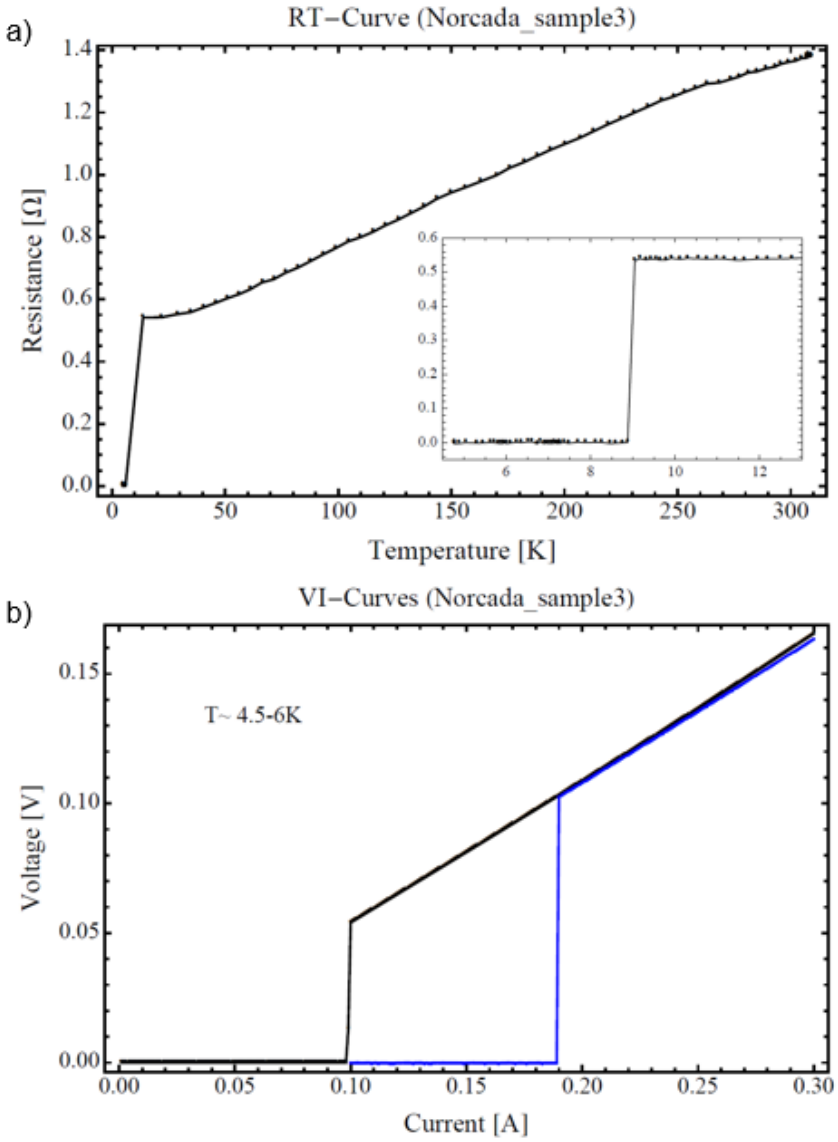

Figure 5.2: a) A four-lead resistance measurement of the "Norcada sample3" membrane consisting of a 300 nm Nb film sputtered by Norcada. Inset is a magnification of the region of interest. The transition temperature of this sample is approximately 9 K. b) A four-lead voltage vs current measurement of the same sample. The critical current is between 100-190 mA for this sample in the temperature range of 4.5-6 K.

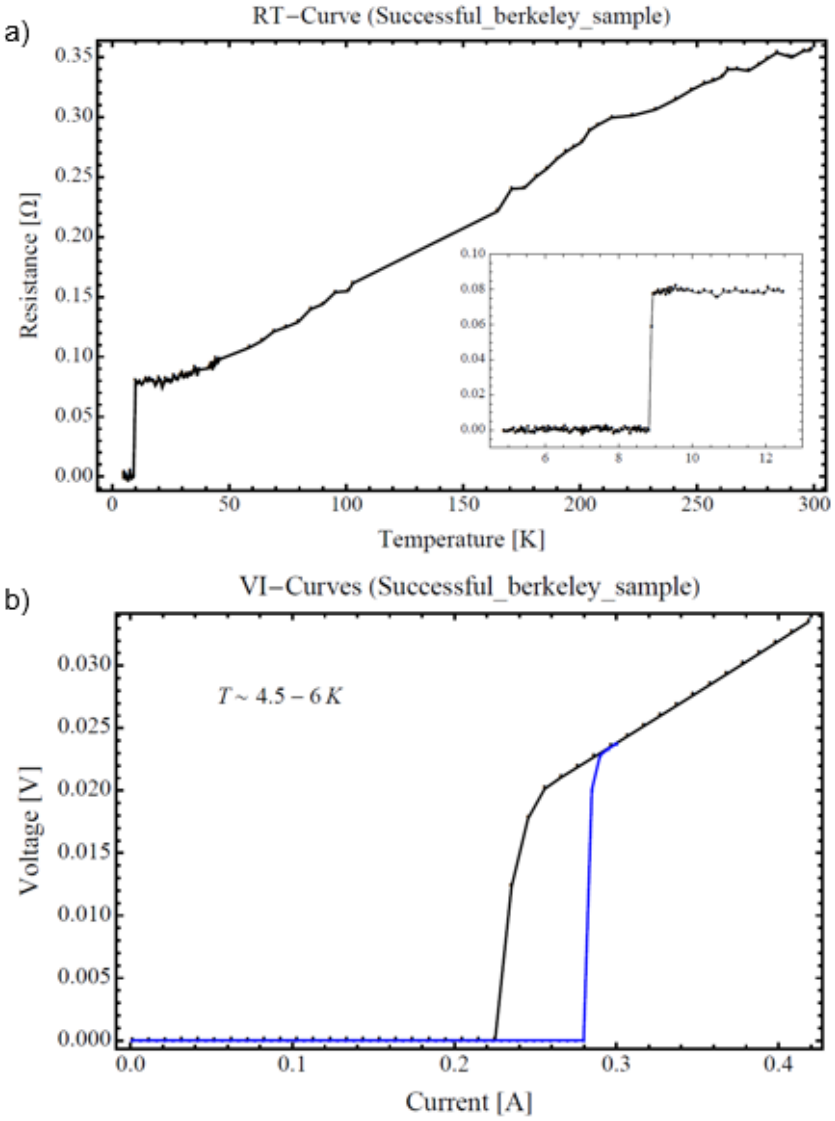

Figure 5.3: A four-lead resistance measurement of the "successful berkeley sample" membrane consisting of a 300 nm Nb film which was sputtered at Marvell Nanolab in Berkeley. Inset is a magnification of region of interest. The transition temperature of this sample is approximately 9 K. b) A four-lead voltage vs current measurement of the same sample. The critical current is between 220-280 mA for this sample in the temperature range of 4.5-6 K.

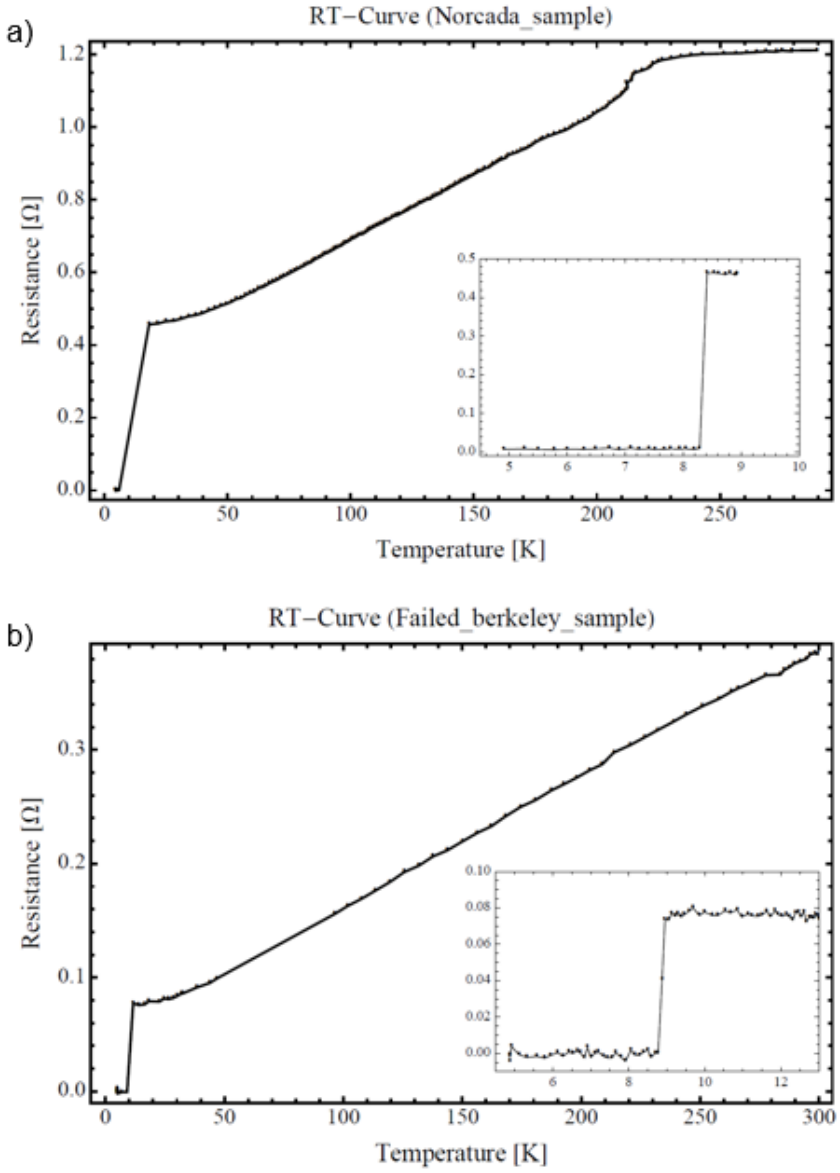

Figure 5.4: a) A four-lead resistance measurement of the "Norcada sample" membrane consisting of a 300 nm Nb film sputtered by Norcada. Inset is a magnification of the region of interest. The transition temperature of this sample is approximately 8.3 K. b) A four-lead resistance measurement of the "faield berkeley sample" membrane consisting of a 300 nm Nb film which ruptured during the sputtering process at Marvell Nanolab in Berkeley. The Si frame remained intact, so we tested the Nb film quality along this surface. Inset is a magnification of region of interest. The transition temperature of this sample is approximately 9 K.

5.4 Driving

5.4.1 The Maxwell stress tensor

One can achieve mechanical motion of a thin film in an SRF cavity by tuning the pump laser to near cavity resonance. The intense optical field that builds up within the cavity results in radiation pressure and simple harmonic motion of the film. This mechanical motion, in turn, frequency modulates the optical field. Consequently, there is an exchange of energy between the optical field and mechanical motion. Careful control of the frequency of the optical field with respect to the resonance frequencies of the cavity and the mechanical oscillator allows one to control the flow of energy, either driving the mechanical oscillator (heating) or damping the mechanical oscillator (cooling). Cavity optomechanics is appealing not only because one can cool a particular mode of the mechanical oscillator into its quantum-mechanical ground state, but also because driven coupled oscillators of this sort lead to other quantum-mechanical effects such as squeezing and entanglement.

The difference between radiation pressure from a coherent laser beam and a stimulated microwave may seem trivial, but the fact remains that a thorough calculation must be performed to confirm their similarities and differences if we want to determine whether it is possible to drive a mechanical oscillator using the TE_{011} mode. First, let us consider an electromagnetic plane-wave. The radiation pressure here is the same as that of a coherent laser beam in its lowest-order Gaussian intensity profile of identical input power since we are merely looking at the force per unit area of the wave. The Gaussian beam is spatially distributed according to Gaussian statistics, but it contains the same amount of energy as the plane-wave. Therefore, integrating over the effective area will lead to the same resultant pressure. The radiation pressure of a plane-wave is well known and is given by

$$P = \frac{\epsilon_0}{2} E_0^2 \tag{5.1}$$

where E_0 is the maximum amplitude of the field. Calculating the pressure from a microwave in our aluminum cavity will necessitate a slightly more complex approach. Since the Poynting vector of TE and TM modes do not impinge on the membrane directly, it is useful to introduce the Maxwell Stress Tensor (MST). We can use the MST here to determine the pressure due to the electromagnetic field at the surface of the membrane. The MST can be broken down into its individual components as follows:

$$T_{ij} = \epsilon_0 \left(E_i E_j - \frac{1}{2} \delta_{ij} E_0^2 \right) + \frac{1}{\mu_0} \left(B_i B_j - \frac{1}{2} \delta_{ij} B_0^2 \right) \tag{5.2}$$

where i and j represent coordinate indices, T_{ij} represents one component of the tensor, $E_{i/j}$ and $B_{i/j}$ represent the electric and magnetic field components matching T_{ij}, and δ_{ij} is the standard Kronecker delta whose value is 1 if $i = j$ and 0 if $i \neq j$ [55]. One component of the MST represents a force oriented in the i direction acting on a surface oriented in the j direction. Therefore, diagonal components of the matrix represent $pressures$ while off-diagonal components represent $shears$. The electric and magnetic field components for the TE_{011} mode are

$$\begin{aligned}
E_\rho\left(TE_{011}\right) &= 0 \\
E_\phi\left(TE_{011}\right) &= -iH_0\frac{\eta\omega R}{cx'_{01}}J'_0\left(\frac{x'_{01}}{R}\rho\right)sin\left(\frac{\pi}{L}z\right) \\
E_z\left(TE_{011}\right) &= 0 \\
H_\rho\left(TE_{011}\right) &= H_0\frac{\pi R}{Lx'_{01}}J'_0\left(\frac{x'_{01}}{R}\rho\right)cos\left(\frac{\pi}{L}z\right) \\
H_\phi\left(TE_{011}\right) &= 0 \\
H_z\left(TE_{011}\right) &= H_0J_0\left(\frac{x'_{01}}{R}\rho\right)sin\left(\frac{\pi}{L}z\right)
\end{aligned} \tag{5.3}$$

where all we have done is re-written Eq. 2.1 and set $m = 0$, $n = 1$, and $p = 1$. Next, we set z equal to L since we are interested in the field mechanics specifically at the membrane's surface and it acts as one end of the cavity. The only non-zero term remaining is

$$H_\rho = -H_0\frac{\pi R}{Lx'_{01}}J'_0\left(\frac{x'_{01}}{R}\rho\right) \tag{5.4}$$

which means the only non-zero component of the MST oriented in the z-direction is

$$T_{zz} = \frac{1}{2\mu_0}(-B_\rho^2) \tag{5.5}$$

where we have converted H_ρ to B_ρ for convenience. We can use the same argument as before to say that the force per unit area depends on the maximum magnetic field magnitude at the surface of the membrane and rewrite Eq. 5.5 as

$$T_{zz} = -\frac{1}{2\mu_0}B_0^2. \tag{5.6}$$

Keeping in mind that $B = \frac{1}{c}E$ and $c = \frac{1}{\sqrt{\epsilon_0\mu_0}}$, we see that this expression simplifies to

$$|T_{zz}| = \frac{\epsilon_0}{2}E_0^2 \tag{5.7}$$

which is analogous to our expression for the radiation pressure impinging on the membrane from a Gaussian beam of identical input power. This result gives us confidence that we will be able to successfully drive the membrane using the TE_{011} mode.

5.4.2 Membrane motion detection using a Michelson interferometer

As a precursor to future cryogenic temperature experiments in which we desire high Q, we have measured the displacement of membranes that have been driven by the TE_{011} mode. The membranes were fabricated by Norcada and consist of a 500 μm Si frame with a 500 nm thick SiN layer that has been coated with 300 nm of Nb. These membranes are mounted to an aluminum cavity (Fig 5.5and this combination is placed in a vacuum chamber pumped down to approximately 7 mbar.

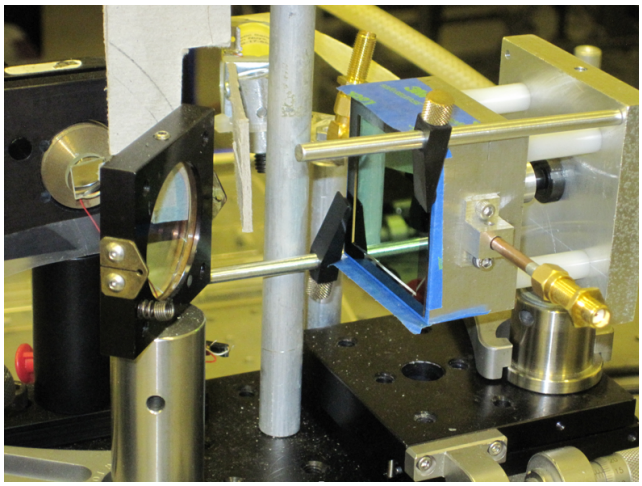

Figure 5.5: Experimental configuration of the Al cavity with Nb-coated SiN membrane attached.

For these experiments, we used a 10 mW helium-neon 633 nm laser as the light source for a Michelson interferometer setup. The displacement amplitude for one of these membranes, x_0, in a Michelson interferometry scheme (Fig. 5.6) can be extracted from

$$x_0 = \frac{\sqrt{2}V_s\lambda}{4\pi\sqrt{\Delta V_1 \Delta V_2}\sin(2kd)}, \tag{5.8}$$

where $kx_0 << 1$, λ is the laser wavelength, d is the DC optical path difference, $\Delta V_{1,2}$ are the voltages of each arm of the interferometer, and V_s is the *rms* voltage

from a Thorlabs FDS 100 Si photodiode detector which we used to convert the light intensity from the interferometer into a voltage. Note that the voltages ΔV_1 and ΔV_2 are measured relative to the DC offset voltage of the detector when no light is incident. The optical phase added by the DC optical path difference is tuned via a piezoelectric actuator prior to any modulation so that $\sin(2kd) = 1$. This occurs when the total voltage is equal to the sum of the individual voltages from each arm of the interferometer; $\Delta V = \Delta V_1 + \Delta V_2$. After proper tuning, the displacement of the membrane is extracted from a measurement of the DC and *rms* voltages from Eq. (5.8) with $\sin(2kd) = 1$.

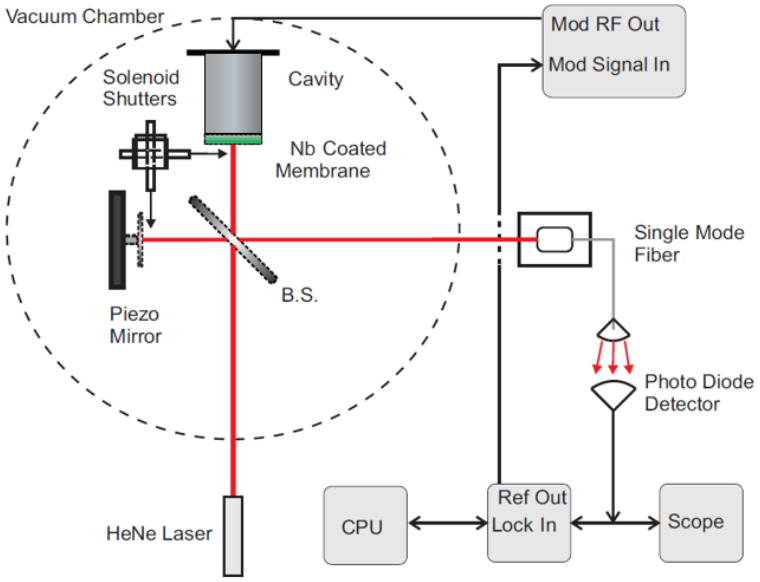

Figure 5.6: Experimental configuration for SiN membrane displacement amplitude measurements. The membrane is driven into motion by an RF signal that is amplitude modulated at its mechanical resonance. We use a Michelson interferometer to measure the phase difference between optical paths.

The DC voltages (ΔV_1 and ΔV_2) were measured with an oscilloscope. Solenoid-actuated blockers were used to block the beams as necessary to measure each arm's intensity. A piezoelectric actuator was used to tune the interference pattern to its most sensitive setting as described above. The *rms* voltage was measured with an SRS 830 DSP lock-in amplifier, and the lock-in reference signal was used to amplitude modulate the Agilent N5183A RF signal generator at the reference frequency. A Labview VI program automatically swept the reference frequency and recorded the *rms* voltage measurement from the lock-in. Data representing the displacement of the square and circular membranes are shown below in Fig. 5.7.

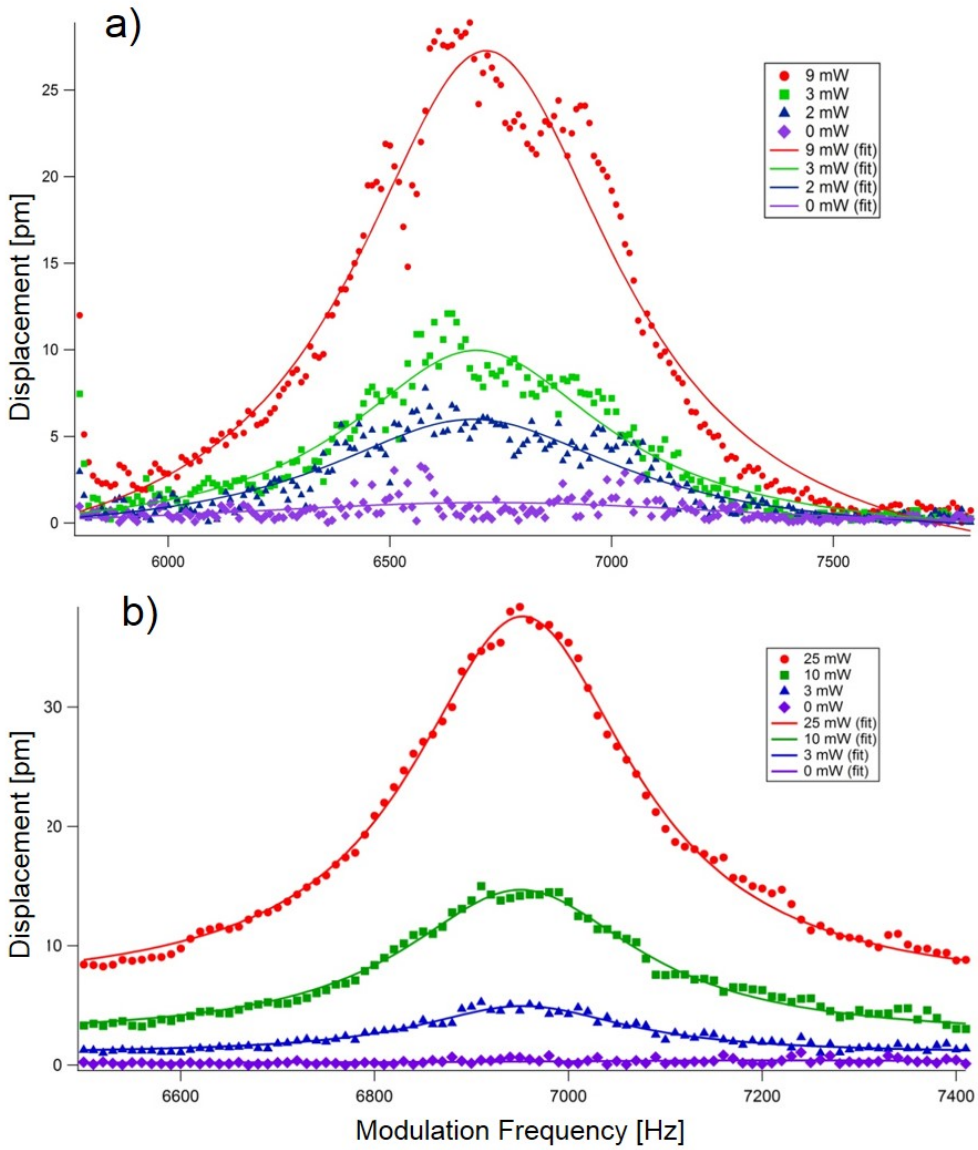

Figure 5.7: a) Data representing the displacement amplitude of a rectangular, Nb-coated SiN membrane as a function of RF amplitude modulation frequency. b) Data representing the displacement amplitude of a circular, Nb-coated SiN membrane as a function of RF amplitude modulation frequency.

The "double peak" trend in Fig. 5.7a) could be attributed to square membrane mode degeneracy as a result of x and y length inconsistencies in the square geometry. The data in Fig. 5.7b) clearly conform to a Lorentzian fit indicating a lack of the possible degeneracy present in the square windows. Resonance occurred at 6.75 kHz in the rectangular membrane and 6.95 kHz in the circular membrane. The graphs demonstrate clear evidence of membrane motion as even the lowest signal is an order of magnitude above the interferometer's noise floor.

When examining the relationship between the maximum displacement, u_{max}, and the seeded RF power, P_{ext},

$$u_{max} = \frac{P_{ext} Q_{RF}}{\pi m f_{011} L} \sum_n \frac{a_n + b_n}{\sqrt{(\mu_n \omega_n^2 - \Omega^2)^2 + 4\beta^2 \Omega^2}} \tag{5.9}$$

we see that these values are proportional and should exhibit linear behavior when plotted against each other [44]. Fig. 5.8 demonstrates this linear relationship for the square and circular membranes and serves as additional evidence for membrane motion as a result of the TE_{011} mode.

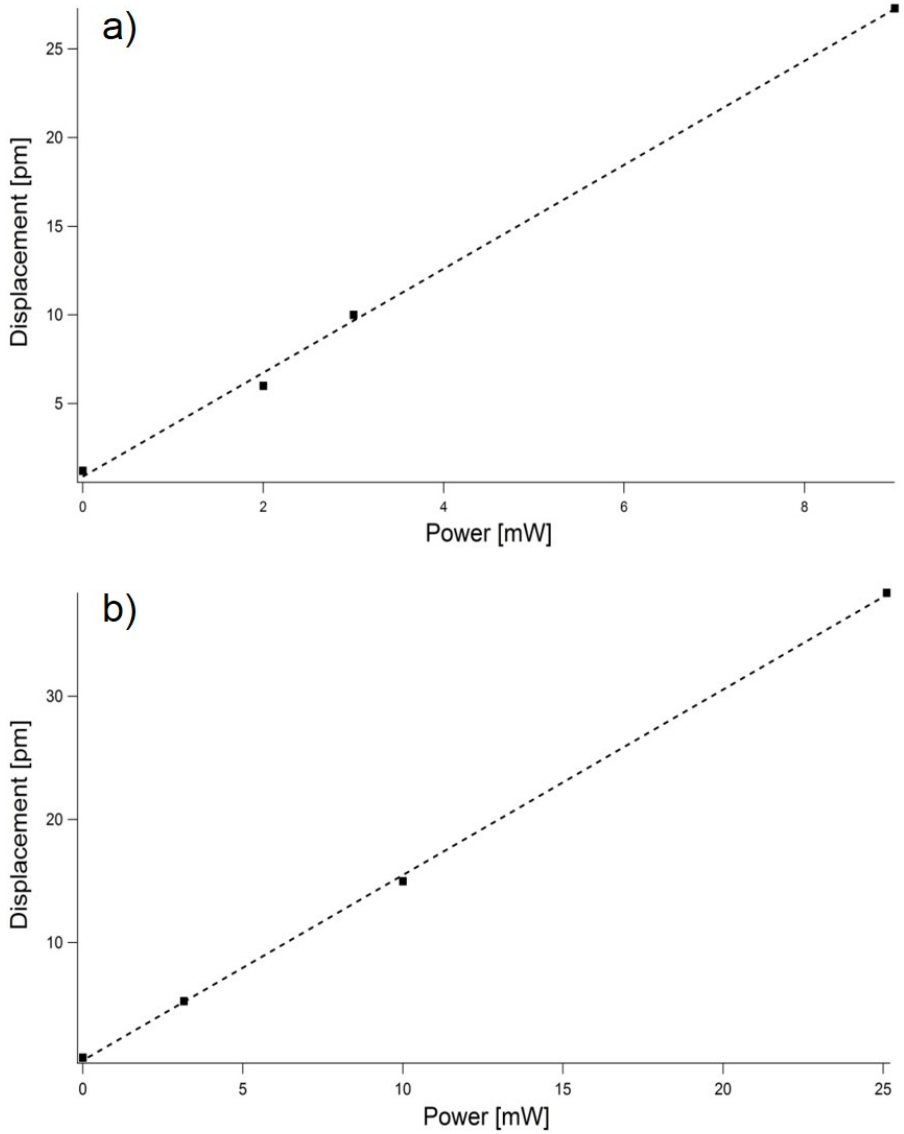

Figure 5.8: a) Rectangular membrane displacement amplitude as a function of input RF power. The displacement data points are taken to be the average peak displacement for a given input RF power. b) Circular membrane displacement amplitude as a function of input RF power. As in part a), the displacement data points were obtained by averaging the peaks of a given input RF power.

5.4.3 Vibrational modes

It is useful to analyze the behavior of the membrane as it vibrates from the modulation of the input RF signal. The fashion in which this oscillation occurs speaks to the potential success of future experiments. Although we were unable to detect higher order modes in the rectangular membrane configuration, we have observed two additionally resonant modes in the circular membrane configuration. These resonances occurred at 8.2 kHz and 13.5 kHz and their displacement data are shown below in Fig. 5.9. As expected, the amplitude of oscillation is significantly reduced at higher frequencies.

In order to determine which modes these peaks correspond to, we look to the equation for mode resonances in circular geometries

$$\omega_{mn} = \lambda_{mn}\frac{v}{r} \tag{5.10}$$

and try and match the predicted resonances with their experimental counterparts. Here, m and n represent the number of nodes in the azimuthal and radial directions, λ represents the zero value of a Bessel function determined by m and n, v is the speed of sound in the membrane, and r is the radius of the membrane. Table 5.1 gives the expected resonance frequency of select circular membrane modes. The resonance frequencies in the table are based on an estimate of the speed of sound in the membrane which is given by the equation

$$v = \sqrt{\frac{\sigma}{\rho}} \tag{5.11}$$

where σ is the membrane's stress and ρ is the film's density. The stress in the film is given by Norcada's website to be >250 MPa, so some uncertainty will remain until further experiments divulge the membrane's actual tensile stress. The strongest signal obtained in circular membrane experiments (Fig. 5.7b)) most likely represents the second-order fundamental mode ($m = 0$, $n = 2$). By this logic, and by referencing Table 5.1, one can infer the location of other higher order modes. For example, the modes presented in Figs. 5.9a) and 5.9b) could correspond to λ_{12} and λ_{13}, respectively. Unfortunately, without further data, the results remain inconclusive for now. The same is true for signals observed at even higher frequencies.

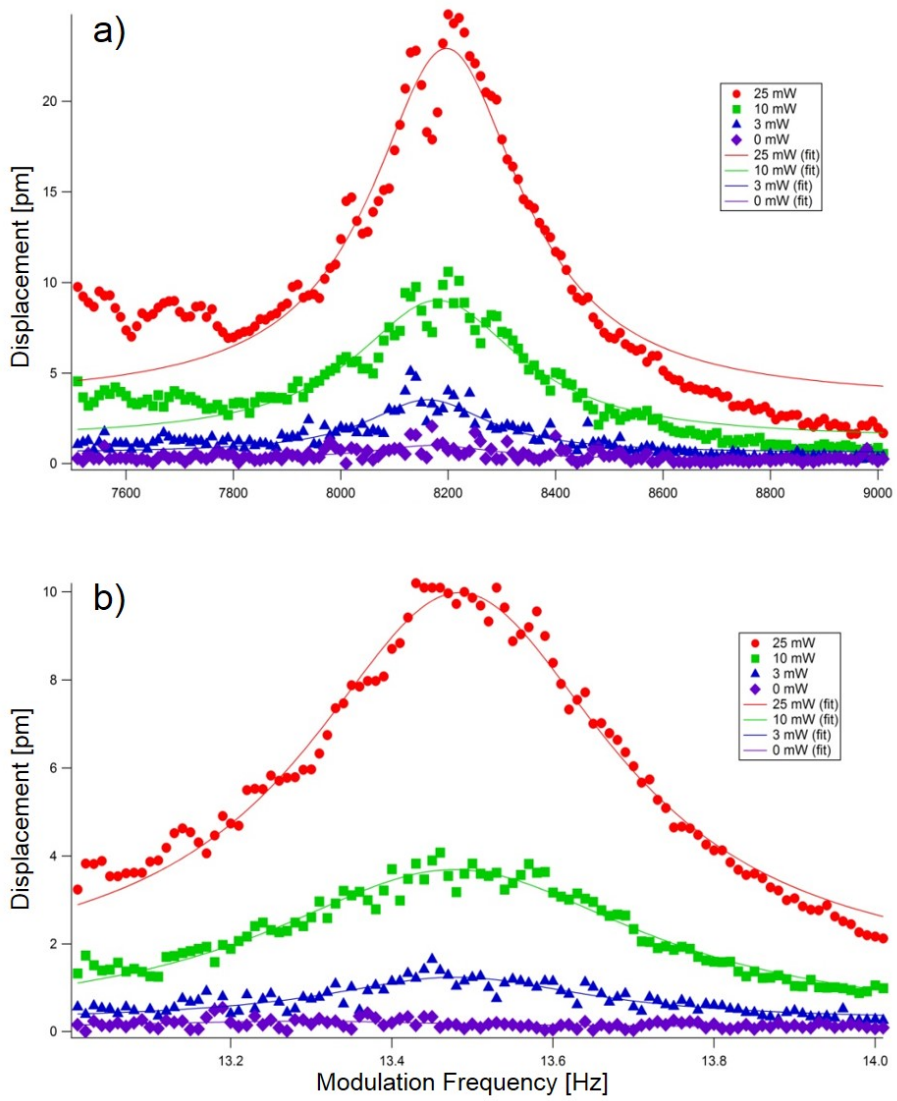

Figure 5.9: a) Data representing the displacement amplitude of a circular, Nb-coated SiN membrane as a function of RF amplitude modulation frequency. The resonance of this mode appears to be located at 8.2 kHz. b) Data representing the displacement amplitude of a circular, Nb-coated SiN membrane as a function of RF amplitude modulation frequency. The resonance of this mode appears to be located at 13.5 kHz.

Table 5.1: The expected resonance frequency for circular membrane modes based on the values of m and n. As mentioned earlier in this section, the values shown are estimates based on an uncertain value of the membrane's tensile stress.

	m	n	λ_{mn}	ω_{mn}	f_{mn}
λ_{01}	0	1	2.40483	21545.93	3.43 kHz
λ_{02}	0	2	5.52008	49456.81	7.87 kHz
λ_{03}	0	3	8.65373	77505.68	12.34 kHz
λ_{11}	1	1	3.83171	34329.97	5.46 kHz
λ_{12}	1	2	7.01559	62855.74	10 kHz
λ_{13}	1	3	10.1735	91148.84	14.51 kHz
λ_{21}	2	1	5.13562	46012.27	7.32 kHz
λ_{22}	2	2	8.41724	75413.74	12 kHz
λ_{23}	2	3	11.6198	104106.9	16.57 kHz

Chapter 6

Tunable SRF cavities as RF filters and coupled quantum systems

6.1 Tuning

Many experiments involving SRF cavities rely heavily on frequency tunability for gathering data or tweaking certain parameters. The capability to tune a metallic cavity is fairly straightforward when performing experiments at room temperature, but tuning SRF cavities through (relatively) large frequency ranges while inside a DR and cooled to below 1 K proves to be another matter altogether. Mechanically pushing on a cavity wall with a micrometer is no longer an option without extensive engineering due to the stringent conditions necessary for the DR to reach such low temperatures. Here we outline the tuning capabilities we have developed for enhanced cavity performance at cryogenic temperatures.

We anticipate that tuning our SRF cavities will be vital in experiments involving multiple cavities. The parametric amplifier/oscillator three cavity system, in particular, will require the ability to tune all three cavities to degeneracy. Such an experiment requires a tunability range that overcomes uncertainty in cavity dimensions resulting from machining and etching. Assuming a machining uncertainty of approximately 12.7 μm (0.0005 inches is standard radial tolerance for most lathes) and an etching uncertainty of 1 μm over several hours, the total frequency uncertainty is estimated to be $\pm$6 MHz. The DR environment severely limits our options in regards to tuning methods so we begin to circumvent this problem with an investigation into piezoelectric transducers (PZTs).

6.1.1 Stack actuator

Early frequency tuning experiments utilized a ceramic stack PZT wedged between a fixed aluminum slab and the cylindrical wall of a prototype aluminum

cavity at room temperature. Increasing applied voltage to the stack causes it to push against the cavity wall and the resulting bending of the metal yields a shifted cavity response. The measured response can be seen in Fig. 6.1 and shows a frequency tunability range of approximately 200 kHz which is well below the desired range.

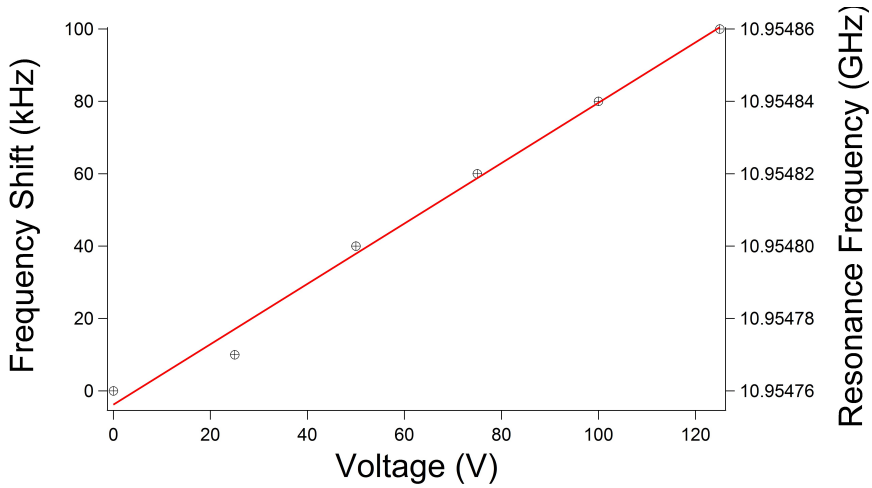

Figure 6.1: Response of an aluminum prototype cylindrical cavity to the force applied by a stack PZT to its outer wall. The left vertical axis shows the shift in cavity resonance for a given voltage while the right vertical axis shows the exact cavity resonance at said voltage. The stack PZTs operate between applied voltages of 0 to 125 V. A linear plot is fit to the graph to demonstrate the linear nature of detuning in this small resonance window of the cavity.

Further, tuning range is expected to decrease by one order of magnitude, down to 20 kHz, for tests at cryogenic temperatures. This poor tunability makes sense when considering the Young's modulus for aluminum. The equation for the change in length of a material based on its Young's modulus and the force applied is

$$\Delta L = \frac{F L_0}{A Y} \tag{6.1}$$

where Y is the material's Young's modulus, F is the force applied to the object over area A, and L_0 is the original length of the material. Plugging in a cavity wall thickness of 0.3 cm, a PZT cross-sectional area of 2×10^{-5} m^2, a PZT blocking force of 1000 N, and the Young's modulus for aluminum, we see a change in local cavity wall thickness of approximately 1×10^{-6} m, or 1 μm. Looking back to the equation for the resonance of a cylindrical cavity, Eq. 2.2, we can expect a shift in cavity resonance based on this change to the local cavity wall thickness as this is a change in effective cavity radius over a small portion of the cavity's length. This can be

calculated by multiplying the shift in frequency from a change in the total radius and multiplying by the ratio of PZT width to total cavity length. The equation looks like

$$\Delta f = \frac{c}{2\pi}\sqrt{\left(\frac{x'_{mn}}{R}\right)^2 + \left(\frac{\pi}{L}\right)^2} \times \left(\frac{w_{PZT}}{L}\right) \tag{6.2}$$

which leads to a change in cavity resonance of approximately 20 kHz which is actually less than the measured value.

6.1.2 Bimorphic actuator

After discovering this limitation, we decided to investigate alternative piezoelectric implementations. Namely, bimorphic actuator PZTs stood out as a particularly effective method for tuning cavity resonance. These piezoelectric devices have a much larger dynamic range than their stack counterparts due to their flexural nature. The large dynamic range comes at the cost of requiring the PZT to be fixed along its circumference. An applied voltage causes one layer of the bimorphic material to expand while the other contracts. This leads to a bending motion resembling a drumhead oscillation that can linearly translate a fixed object a great deal more than stack PZTs; up to 500 μm for actuators with our specs. This results in an effective translational range of approximately 60 MHz, or 6 MHz at cryogenic temperatures. While this may seem sufficient for our purposes, bimorphic PZT implementation has some major drawbacks. Namely, the actuator cannot simply push against an end-wall as this will create a protruding hemisphere rather than translating the end-wall a full 500 μm. Consequently, we designed and built a piston-like attachment for the bimorphic PZT which acts as a movable end-wall. This attachment allows for completely linear end-wall translation and subsequent tunability in our Nb cavities.

We tested two actuators in two cavities of equal volume but differing material at cryogenic temperature. Results of these tests are shown in Fig. 6.2. The results indicate a slight difference in total translation between the two PZTs across their maximum 60 volt range. We can account for this small difference in dynamic range (3 MHz) by considering subtle experimental differences between cavities such as thermal contraction coefficients, mounting pressure applied, and piston machining precision. Regardless, the test demonstrates larger than expected tunability in both cavities while mounted in a DR.

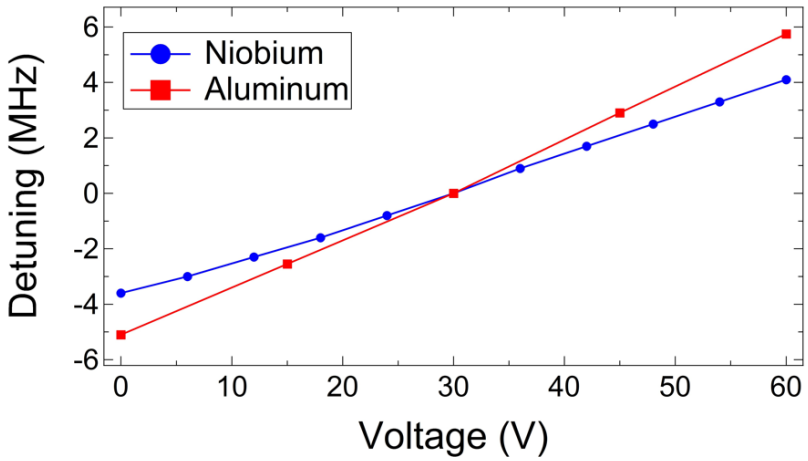

Figure 6.2: Cavity detuning as a function of applied voltage for two separate bimorphic PZTs. The range for applied voltage is much less for these actuators than for stack actuators, but translation remains greater due to their flexural nature. Both tests were performed at cryogenic temperature demonstrating the feasibility and appeal of these PZTs in further experiments.

6.1.3 Cryogenic dielectric translation for stub cavity tuning

The quarter-wave stub cavities are much easier to tune while preserving the integrity of the system since they utilize an open-ended geometry in which the evanescent field decays. The cavities do not, however, lend themselves to simple PZT mounting configurations. A cryogenic linear translator is required in order to hold a dielectric in place and translate it along the cavity's central axis. This dielectric changes the cavity's effective volume thereby shifting the resonance while minimally perturbing the electromagnetic field. Additionally, a linear translator offers a larger range of motion than individual PZTs. This allows for experiments that require an increased frequency range such as demonstration of level repulsion in dual SRF cavities or tuning an SRF cavity-integrated optoelectronic oscillator (OEO) through several modes.

We utilize a Janssen cryogenic linear drive (CLD) that offers a great deal of control at cryogenic temperatures but offers no means of determining actual translation distance while the DR is sealed and operating. Calibration of the CLD requires several measurements across room temperature and cryogenic environments. First, we need a room temperature measurement of the effective cavity pull parameter over a small range of motion. This involves measuring the change in resonance of a stub cavity at room temperature, $\Delta\omega(293K)$, after translating a certain number of CLD steps, N, and using vernier calipers to measure

the physical distance traveled, $\Delta x(293K)$. The step size of the CLD at room temperature is then

$$\xi(293K) = \frac{\Delta x(293K)}{N}. \tag{6.3}$$

The cavity pull parameter at room temperature, given a small $\Delta x(293K)$, can then be defined as

$$G(293K) = \frac{\Delta\omega(293K)}{\Delta x(293K)} = \frac{\Delta\omega(293K)}{N \times \xi(293K)}. \tag{6.4}$$

We then return the CLD to its original position while making sure to account for hysteresis, replace the room temperature coupler with a cryogenic coupler, and begin a cooling cycle of the DR. Due to thermal contraction of the cavity, sapphire rod, and CLD, the resonance at approximately 50 mK will not be identical to the resonance at room temperature. We record the new resonance and then tune the cavity across the frequency range $\Delta\omega(293K)$ while keeping track of the number of CLD steps taken, M. The assumption here is that the system should have an almost identical cavity pull parameter in room temperature and cryogenic environments due to the thermal contraction coefficients of Nb and sapphire being very close in value. Specifically, this means that

$$\Delta\omega(293K) = \Delta\omega(0K) \tag{6.5}$$

and, therefore,

$$G(293K) = G(0K). \tag{6.6}$$

So, for constant temperature and cavity coupling, we can combine Eqs. 6.4 and 6.6 to show that

$$\frac{\Delta\omega(293K)}{\Delta x(293K)} = \frac{\Delta\omega(0K)}{M \times \xi(0K)}. \tag{6.7}$$

This equation allows us to solve for the step size of the CLD at 50 mK

$$\xi(0K) = \frac{\Delta\omega(0K) \times \Delta x(293K)}{M \times \Delta\omega(293K)} = \frac{\Delta x(293K)}{M} \tag{6.8}$$

while keeping in mind that $\Delta x(293K)$ should be measured again after the warm-up. If this value has changed, there is some error associated with the calibration and this should be noted. We now have a value for $\xi(0K)$ which allows for experiments in which the translation distance must be accounted for. A plot of stub cavity S2's resonance versus calibrated CLD translation distance is shown in Fig. 6.3. Results indicate that the sapphire rod minimally perturbs the field after receding approximately 9 mm from the stub of the cavity.

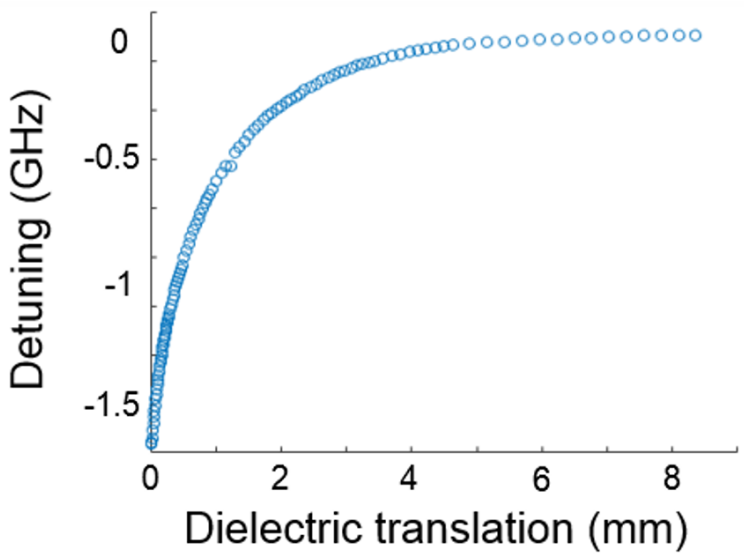

Figure 6.3: Calibrated tuning curve for cavity S2 at approximately 50 mK. The beginning of the curve corresponds to the sapphire rod being in contact with the stub of the cavity. The x-axis then denotes the translation distance away from the stub while the y-axis denotes the corresponding cavity detuning. The x-values were calculated using the methods for CLD calibration described earlier in this section.

A measurable change in intrinsic quality factor became apparent while tuning cavity S2 towards the end of its effective tuning range. While maintaining a critically coupled system at the point of interest in frequency space, we obtained several measurements of intrinsic Q as the rod was retracted from the cavity volume. The results are shown below in Table 6.1.

Table 6.1: Several values of Q_0 for different sapphire rod insertion distances. The values for β demonstrate how the input coupler length affects Q_0. A β of 55 implies extreme over-coupling and that Q_0 for this resonance is larger than indicated and most likely closer to the cavity's natural intrinsic Q of 2×10^8.

Δx (mm)	f_0 (GHz)	Q_0	β
7.0	10.5	2.8×10^7	55
2.1	10.236	1.1×10^6	0.96
0.8	9.8	8.4×10^5	0.47

The position of the rod at resonance 10.5 GHz was chosen because it is far from the stub but still close enough to strongly interact with the electromagnetic fields. Resonance 10.236 GHz was selected because this is the natural frequency of cavity S1. We intend to have these two cavities interact with each other while both are tuned to a degenerate frequency, so knowing the intrinsic quality factor for this rod position seems worthwhile. Resonance 9.8 GHz was chosen because this was the lowest frequency in which we could obtain β and subsequently calculate Q_0.

6.2 Double cavity mechanics

The "double cavity" portion of the proposed system is complicated enough to warrant its own discussion. Specifically, energy transfer between the two cavities poses a challenge since the splitting in the spectral doublet must be a certain value to achieve parametric amplification and oscillation. We do not fully understand the mechanics underlying this process, but this section will attempt to analyze the double cavity in a room temperature and SRF setting. We will use quarter-wave stub cavities for these analyses and experiments since we have achieved higher quality factors in these types of cavities compared to others.

6.2.1 Modeling the double cavity as a potential well

First we define the simplest case of basis states to represent each cavity

$$\begin{aligned} |L\rangle &= \begin{pmatrix} 1 \\ 0 \end{pmatrix} \\ |R\rangle &= \begin{pmatrix} 0 \\ 1 \end{pmatrix} \end{aligned} \tag{6.9}$$

where $|L\rangle$ is the left cavity and $|R\rangle$ is the right cavity. Next, we define κ in terms of these basis states

$$\begin{aligned} \kappa &= \langle L| \, H \, |R\rangle \\ &= \langle R| \, H \, |L\rangle \end{aligned} \tag{6.10}$$

and set up the Hamiltonian matrix in terms of the resultant energies and our coupling constant

$$H = \begin{bmatrix} E_L & \kappa \\ \kappa & E_R \end{bmatrix} \tag{6.11}$$

where E_L and E_R refer to the left cavity energy and right cavity energy, respectively. For clarity, Fig. 6.4 depicts the system described by the above Hamiltonian.

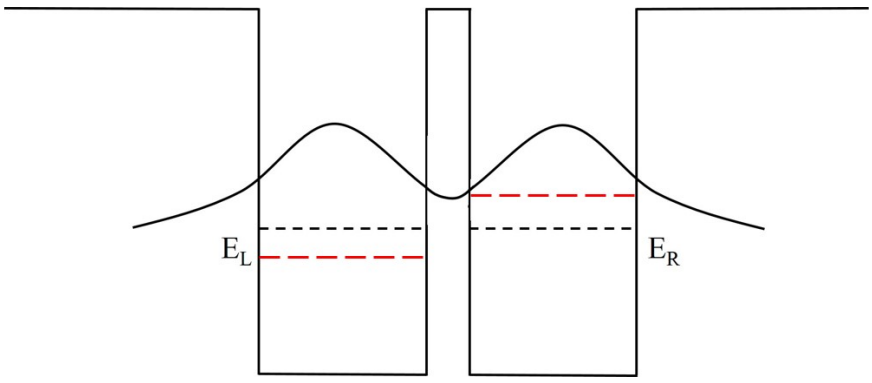

Figure 6.4: The degenerate (black dashed) and repelled (red dashed) energy eigenstates of a double potential well. A non-zero coupling constant, κ, allows for energy exchange between the two wells.

Taking the determinant, we see that

$$\begin{vmatrix} E_L - E_\kappa & \kappa \\ \kappa & E_R - E_\kappa \end{vmatrix} = 0$$
$$E_\kappa^2 - (E_L + E_R)\, E_\kappa + \left(E_L E_R - \kappa^2\right) = 0 \tag{6.12}$$

which is a quadratic and can, therefore, be solved using the quadratic equation. Doing so yields

$$E_{\kappa\pm} = \frac{(E_L + E_R) \pm \sqrt{(E_L - E_R)^2 - 4\,(E_L E_R - \kappa^2)}}{2} \tag{6.13}$$

where 2κ represents the minimum width of the avoided crossing. This becomes more clear after setting $E_L = E_R = E_0$, as is the case in identical cavities, and simplifying to obtain

$$E_{\kappa\pm} = E_0 \pm \kappa \tag{6.14}$$

leading to the relationship

$$\Delta E_{min} = 2\kappa \tag{6.15}$$

as expected. Assigning the notations

$$\begin{aligned} E_L &= E_0 \\ E_R &= E_0 + F \end{aligned} \tag{6.16}$$

where E_0 is some characteristic energy and F is a function of κ allows us to plot these energies as a function of cavity detuning.

6.3 Coupled 3D cavities for quantum electrodynamics

SRF cavities make up a large portion of research in high-energy physics because of their natural affinity for use in particle accelerators [18, 41, 56–58] but they have also been gaining popularity in recent years as a means of performing cavity quantum electrodynamics (cQED) experiments involving the coupling of electromagnetic radiation to qubits [59–61]. This resurgence also includes breakthroughs in superconducting microwave circuits as a means of performing cQED experiments [62–64]. In an effort to move towards a dual-cavity SRF parametric oscillator for cQED, we present experimental results demonstrating an avoided crossing in coupled, high-Q SRF quarter-wave stub cavities.

We expect κ to determine the minimum separation of the avoided crossing based on Eq. 6.13. We will show experimental results demonstrating the avoided crossing for varying values of κ in room temperature and cryogenic environments. Here, κ is determined by antenna length. Avoided crossing experiments were performed both in room temperature and cryogenic environments. As such, the procedure for taking measurements must adjust to the limitations of measuring the experimental system at temperatures below 1 K. Specific methods are outlined for both environments in the following sections.

6.3.1 Room temperature experiments

These experiments were performed with aluminum quarter-wave stub cavities whose cavity-to cavity coupling κ is established by an approximately 13 mm long SMA wire whose cladding was stripped thereby exposing bare wire which was inserted into the cavity through the cavity wall. The intrinsic quality factor of these cavities at room temperature is on the order of 10^3, so the wires must protrude into the cavity to achieve sufficient coupling. Measurements utilized a network analyzer whose signal coupled to the dual-cavity system via SMA cables connected to a coaxial center pin mounted to each cavity's outer wall. These pins were cut to near identical length and we ensured that they were long enough to establish a large enough coupling, C_{RT}, from source to cavity. We utilized a dielectric rod connected

to a translation stage which was oriented parallel to the cavity's symmetry axis as the tuning element of the system. We then recorded the S21 transmission spectrum for several tuning rod translation steps. A photograph of the setup described above is shown in Fig. 6.5.

We adjusted κ by attaching each cavity to a translation stage and adjusting their positions with respect to a stationary SMA placed between them. As a result, we have several plots of avoided crossings between the aluminum cavities for several values of κ. We varied coupling from antenna length $L = 7.25$ mm (the non-avoided crossing regime) to $L = 9.25$ mm (the extremely over-coupled regime) in steps of 0.25 mm.

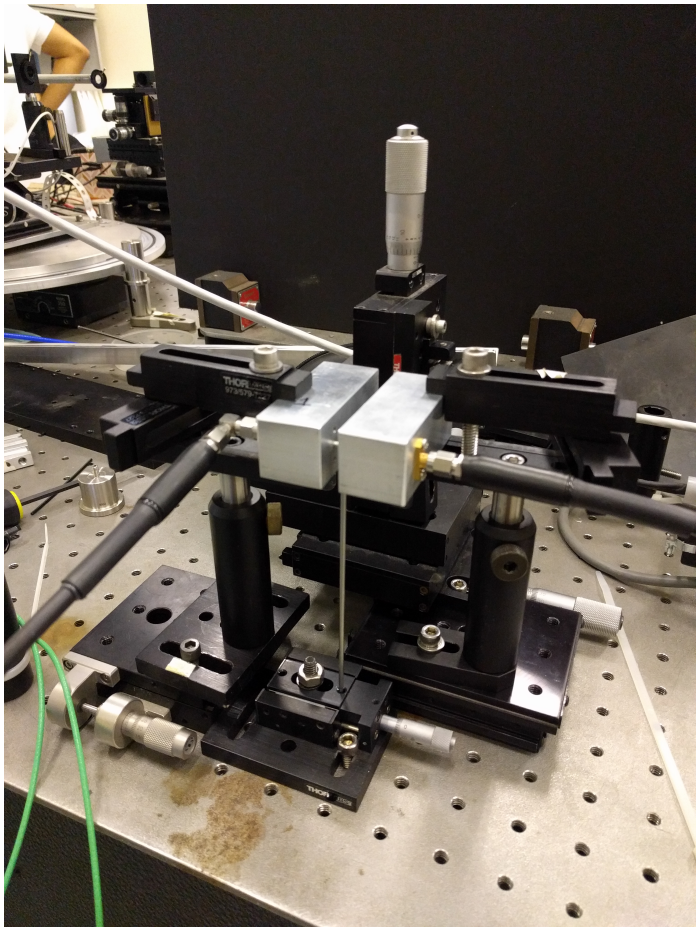

Figure 6.5: A photograph of the double Al cavity system. The cavity-to-cavity coupling, κ, is controlled by translation stage adjustments of 0.25 mm increments.

6.3.2 SRF experiments

SRF experiments were performed with niobium quarter-wave stub cavities in which κ was established through the use of an approximately 13 mm long SMA wire similar to the one used in the previously described room temperature experiments. The bare wire in these experiments does not protrude into the cavity in order to transfer energy between cavities evanescently. A sapphire rod translated by a cryogenic linear drive (CLD) adjusted the resonance of cavity S2. The dual-cavity system is shown in greater detail in Figs. 6.6 and 6.7.

A signal generator fed a 10 GHz signal into the dilution refrigerator and subsequently into the dual-cavity system via SMA cable. The length of the pins that coupled to each cavity mode determined the signal-to-cavity coupling C_{SRF} for each cavity. A cryogenic circulator allowed for both S11 and S21 signals to be recorded. The S11 signal feeds directly to a diode and then to a source meter which measures the peak voltage. The S21 signal passes through a cryogenic HEMT amplifier at 4 K and another amplifier at room temperature before passing through the diode and source meter. We recorded several spectra of both S11 and S21 measurements while translating the sapphire rod through the point of dual-cavity degeneracy.

When κ was limited by antenna length $L = 4.5$ mm, no avoided crossing was observed. Changing κ by adjusting antenna length to $L = 5$ mm lead to an avoided crossing in both S11 and S21 measurements. We also choose a position in frequency space of strong interaction between the two cavity modes and measure for power-dependence in the S21 spectra.

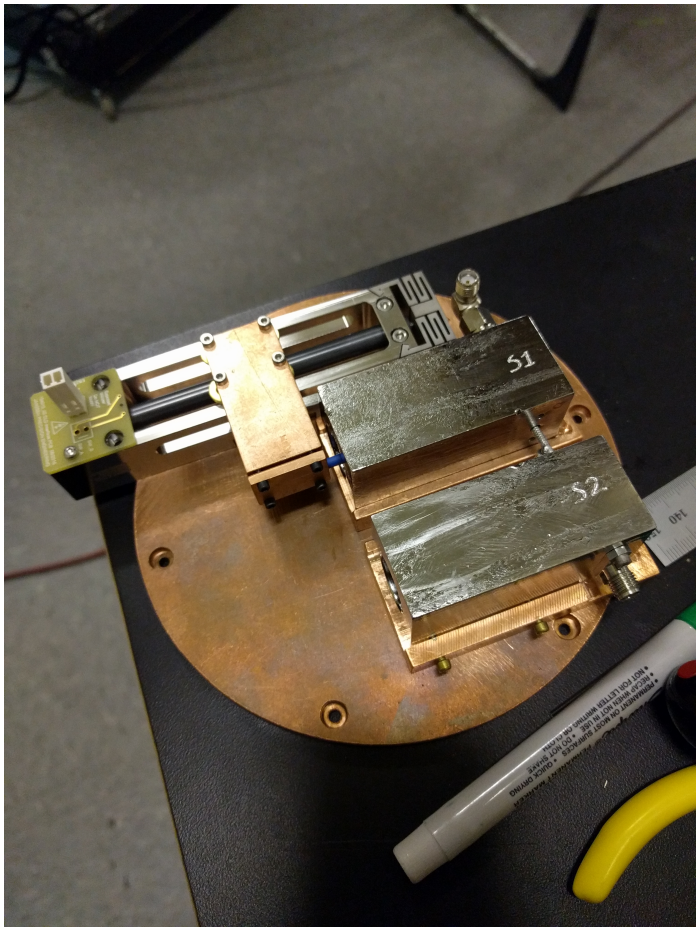

Figure 6.6: A photograph of the double Nb cavity system. Cu mounts hold the cavities in place and are fixed to the Cu plate underneath to provide insurance of reproducibility. A small piece of SMA cable provides the coupling between cavities. A rectangular Cu piece attaches to the CLD and holds the sapphire rod in place.

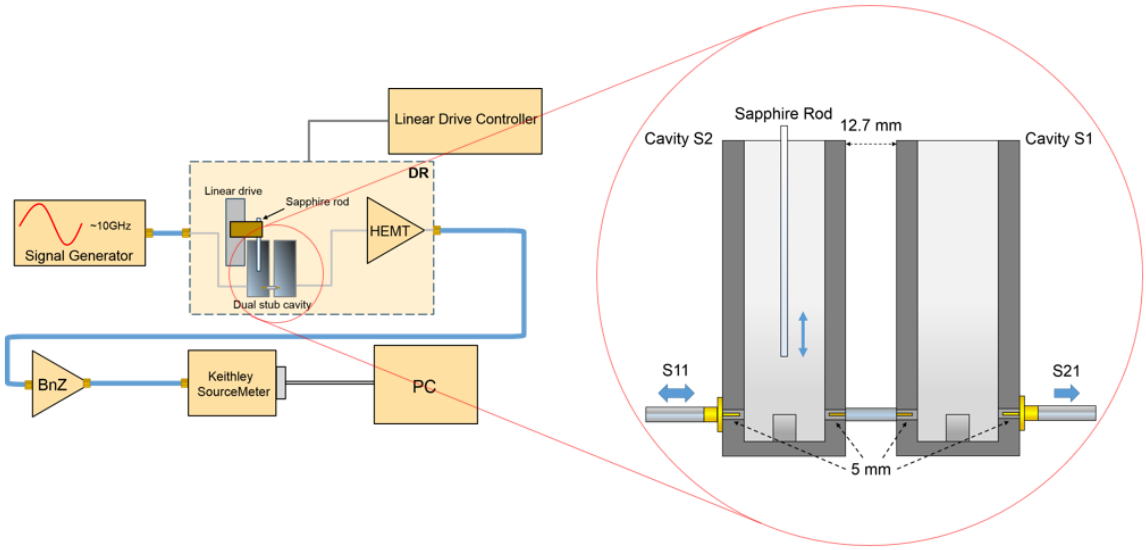

Figure 6.7: The double cavity system in cryogenic environment. Coupling between cavities can occur due to the insertion of bare wire into each cavity wall. The cavities are spatially separated as little as possible to avoid additional modes manifesting in the coupling SMA. Tuning of cavity S2 is possible due to the insertion of a sapphire rod which is translated by a cryogenic linear drive. Use of a cryogenic circulator allows for S11 or S21 measurements. All couplers were set to a length of 5 mm to allow for strong coupling between cavities and over-coupling of the signal into the system.

6.3.3 Room temperature measurements

Nine total couplings were recorded and mapped in 3D plots for room temperature experiments. The results for these plots are shown in Fig. 6.8. These spectra were analyzed and the peak-to-peak frequency separation of each doublet was plotted and recorded. The first data point does not display a minimum separation as this value lies outside the tuning range of the cavity. The rest of the data shows a range in minimum peak separation from approximately 150 to 7 MHz as the coupler antenna is translated out of the cavity. The last data point corresponds to a normal frequency crossing. A plot of the minimum separation as a function of dielectric translation for each antenna length is shown in Fig. 6.9.

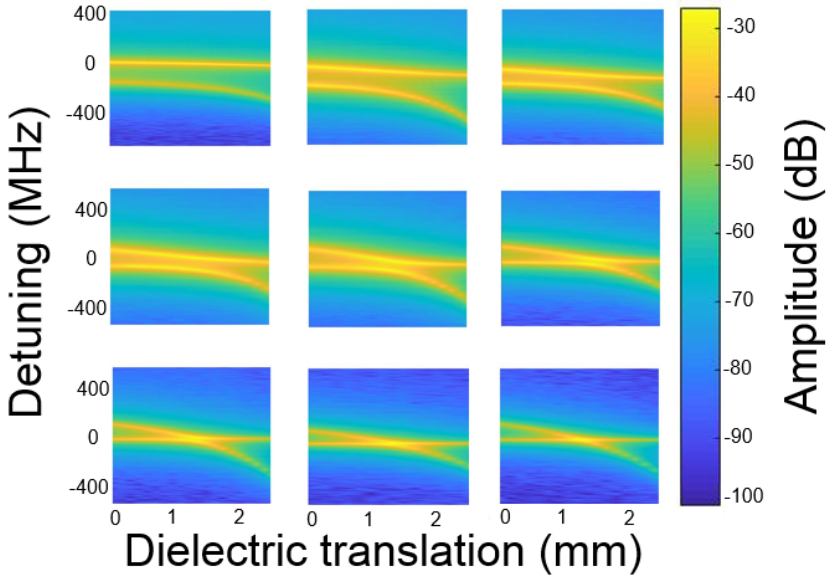

Figure 6.8: 3D plots of the avoided crossing in an aluminum dual-cavity system at room temperature. These plots demonstrate coupling between cavities corresponding to antenna lengths ranging from (left to right, top to bottom) L=7.6 mm (1.9 mm protrusion into cavity) to L=9.4 mm (3.7 mm protrusion into cavity).

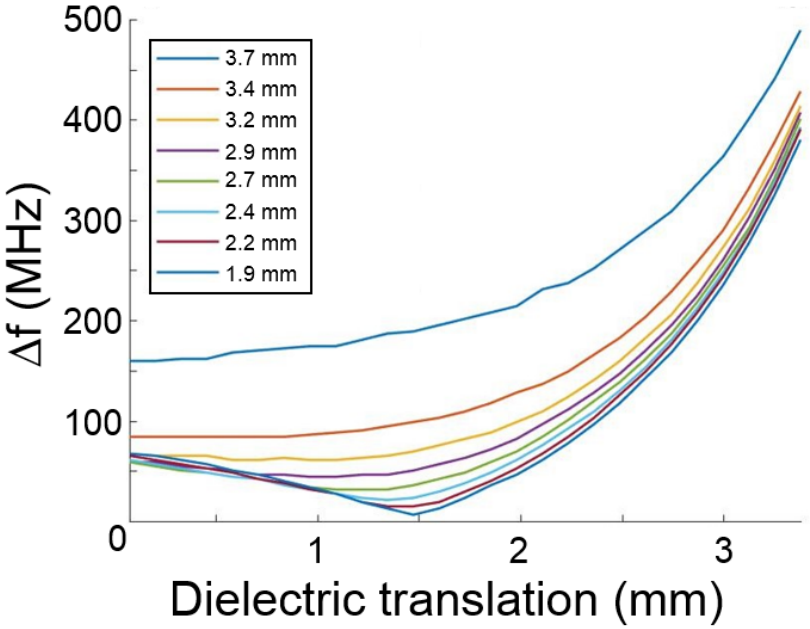

Figure 6.9: All spectral doublet peak frequency differences from room temperature experiments overlaid to demonstrate the downward trend in minimum peak separation as a function of cavity coupling.

A normal crossing occurred while the coupling antenna still protruded several millimeters into the cavity volume. This implies that the fields driving the currents that exchange energy between the cavities dissipate too quickly to achieve effective energy transfer during these experiments. We inferred that the double cavity system required further testing with higher Q cavities in order to achieve an avoided crossing for very short antenna lengths and, therefore, smaller values of κ.

6.3.4 SRF measurements

We performed measurements on a Nb dual-cavity system in dilution refrigerator under vacuum. We took frequency spectra for reflection and transmission measurements much in the same way as we did for room temperature experiments. We first located the frequency doublet, placed the sapphire rod in the desired starting location by manually operating the CLD software, then recording the spectra one at a time after moving the sapphire rod in increments of approximately 1 μm (lowest resolvable translation increment for the CLD in cryogenic environment). Results from these measurements were plotted in 2D and 3D and are shown in Figs. 6.10 and 6.11.

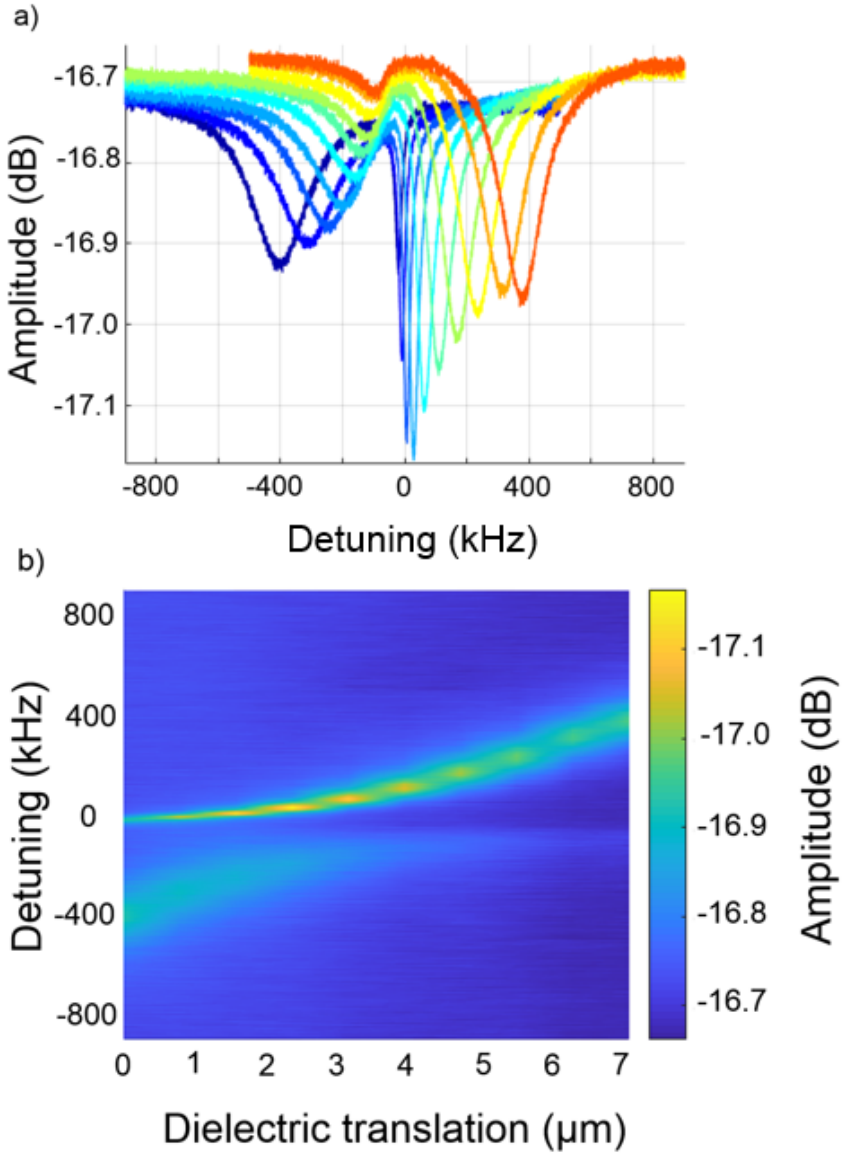

Figure 6.10: a) A standard plot of the S11 signal amplitude as a function of detuning for the spectral doublet in cryogenic environment. This signal for a cavity coupling corresponds to antenna length L=5 mm. b) A 3D plot of the data shown in part a). The z-axis is converted to a logarithmic scale so that the disparity between amplitudes is somewhat alleviated. There is clear evidence of an avoided crossing in each plot.

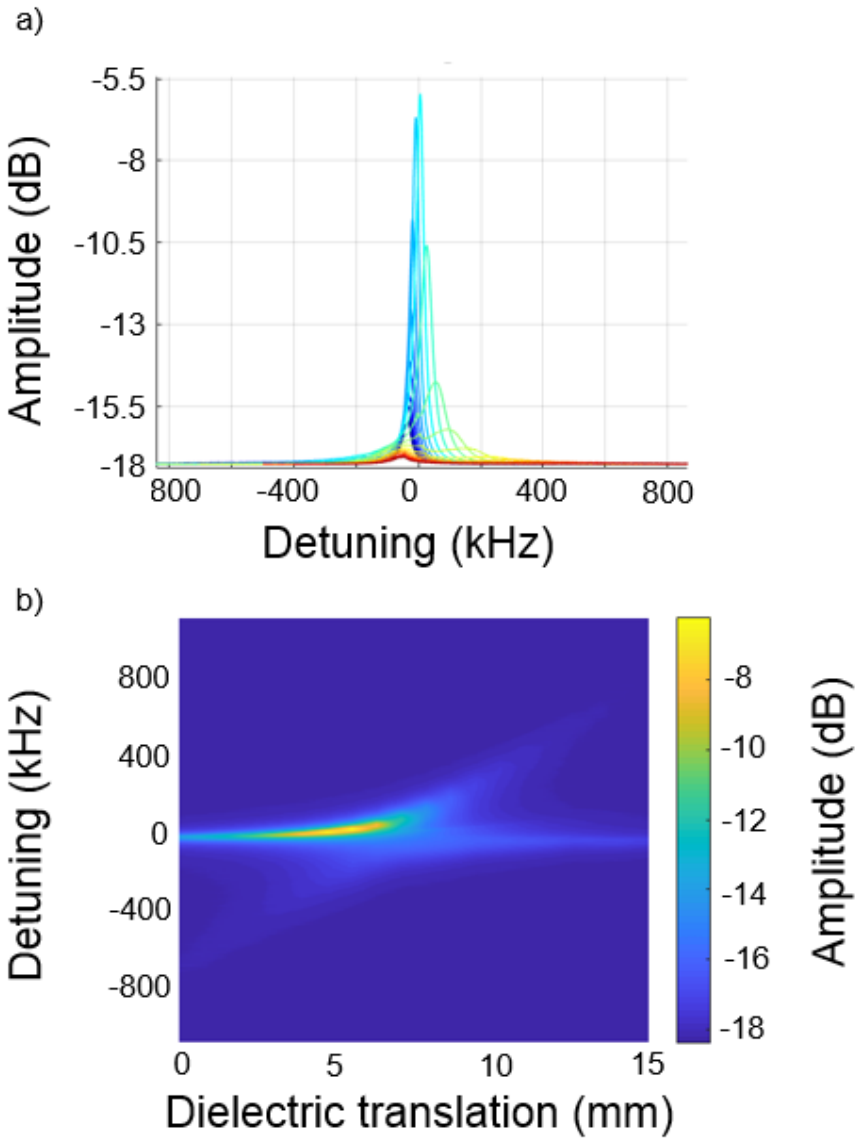

Figure 6.11: a) A standard plot of the S21 signal amplitude as a function of detuning for the same system and cavity coupling as in Fig. 6.10 (antenna length of L=5 mm). b) A 3D plot of the data shown in part a). Again, the z-axis has been converted to a logarithmic scale for ease of viewing.

We also recorded several spectra for the avoided crossing transmission measurement as a function of input power to make sure we were not saturating either of the amplifiers used during these experiments. Input powers ranged from -7 to 2 dBm in increments of 3 dBm. The data for this test is shown in Fig. 6.12. As expected, the curves increase in amplitude for larger input powers, but the data has been normalized here so that any discrepancies between plots become immediately apparent. While the left peak demonstrates some strange behavior, the overall shape and position of the doublet does not appear to change.

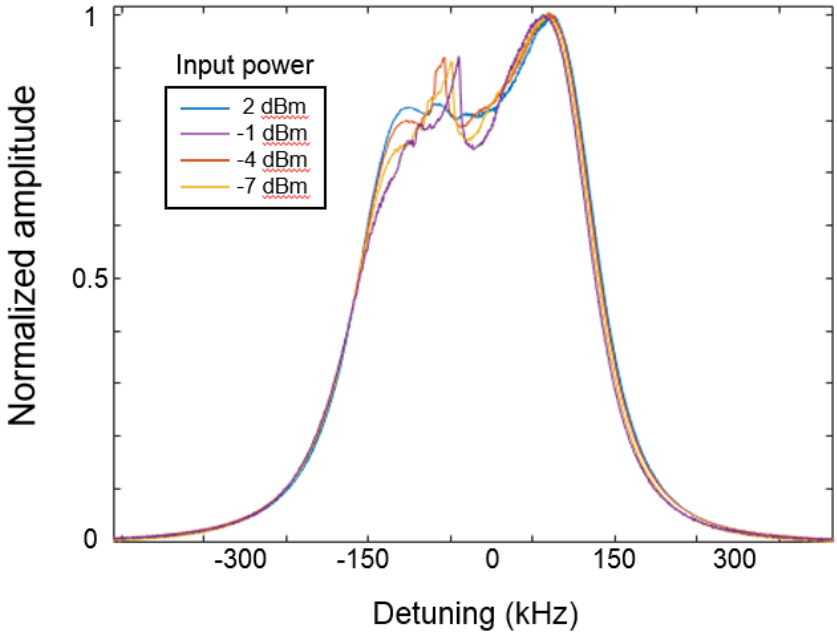

Figure 6.12: Normalized S21 signal amplitude spectra for increasing signal generator power as a function of detuning. We chose a location in frequency space corresponding to strong dual-cavity mode interaction.

Lastly, we plot the numerical values of the minimum peak separations for room temperature and SRF measurements in Fig. 6.13. The dashed red line indicates where the cavity wall is located. Values to the right of the line correspond to room temperature tests as these experiments required strong coupling directly to the fields of the cavity. The value to the left of the line corresponds to the single SRF measurement we achieved. As mentioned previously, coupling efficiently to our high-Q stub cavities requires a recessed center pin for evanescent coupling which does not perturb the cavity mode and degrade the Q.

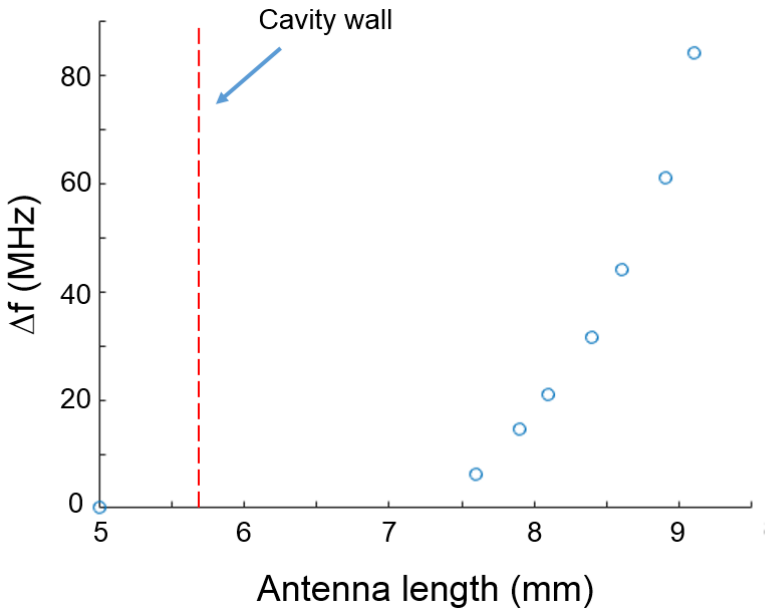

Figure 6.13: The minimum peak separation of the spectral doublet as a function of coupler antenna length. The most highly coupled case did not yield minimum peak separation data because the cavities reached the maximum tuning range before the minimum separation was reached. The dashed red line indicates the location of the cavity wall. Only one data point falls to the left of the line as we were only able to achieve an avoided crossing for one value of κ.

Chapter 7

Outlook

7.1 Thesis summary

Superconductivity is a powerful tool in experimentation as expelling magnetic fields from the volume of a material allows for sensitive measurements of currents and voltage. Currents flowing with almost no resistance also offer a variety of benefits when incorporating superconducting metals or materials into one's experiment. For us, the appeal manifests in the possibility for extremely low losses in an oscillator-like system. The ability to achieve quality factors of 10^9, or even higher [40, 58, 65], facilitates long photon lifetimes in the realm of milliseconds which leads to efficient energy transfer to other potential cavity components. I described a "triple cavity" system earlier in this thesis that aimed to do just that: store a large number of photons in order to drive a mechanical oscillator as a free mass and transfer their energy to a cavity under vacuum.

We discussed the facets involved in designing, machining, and etching a Nb cavity for SRF applications. We identified a problem in the form of the TE_{011} mode being degenerate with the parasitic TM_{111} mode. Solutions to this problem include a circular ridge/groove along the outer edge of the cavity end-cap and a piston-like end-cap that leaves a small gap between its outer edge and the cavity's inner wall. Experiments demonstrated that, while the piston method attenuated the TM_{111} mode completely, it could not sustain quality factors larger than $Q = 10^6$. We outlined the steps necessary to carefully and correctly machine, etch, and bake a Nb cavity. Many hours of work went into perfecting the machining and etching process including several iterations of etching methods. Scientists from Jefferson Labs helped us immensely by agreeing to bake our cavity components in their high-vacuum furnace. We also began to consider an alternative design for our high-Q cavities in the form of the quarter-wave stub cavity.

Next, we discussed testing of single SRF cavity experiments as well as the results from these tests. We introduced S-parameters as the main mechanism behind all

of our measurements and provided examples of what these signals look like on a network analyzer and oscilloscope. We presented all of our cavity prototypes and discussed the reasoning behind each new improvement. We also introduced the coupling constant β which identifies how efficiently the couplers deposit and extract energy from the cavity. β allows us to extract the intrinsic quality factor of the cavity. A value of $\beta < 1$ means the cavity is under coupled while a value of $\beta > 1$ means the cavity is over coupled. If β is too large ($\beta > 5$) it cannot accurately extract the intrinsic Q of the cavity. The process for measuring Q involves sending a modulated signal into the cavity and scanning to locate the resonance. Once it is found, we send a pulsed signal into the cavity and measure the ring down time. We use this value of τ when plugging into the equation for the intrinsic quality factor. We presented the intrinsic Q values for each prototype in a table at the end of the chapter. The Nb stub cavity dubbed "S1" achieved the largest Q of 1.7×10^9.

Chapter 4 saw the introduction of silicon nitride windows sputter-coated with a thin layer of Nb. The silicon nitride window is essential to the success of the project as it acts as the mechanical element that parametrically drives the signal/idler cavities in the triple cavity system. We presented data comparing the RRR values of Nb films from several samples. Films deposited by us at Marvell Nanolab in Berkeley demonstrated RRR values similar to those deposited by Norcada. We then presented data demonstrating clear evidence of a modulated RF field driving several of these membranes into motion. An interferometer setup measured the amplitude of oscillation for these membranes as a function of RF input power. Plotting membrane displacement with respect to input power showed a clear increase in maximum amplitude for increasing RF power.

Lastly, we discussed tuning SRF cavities in the context of double cavity mechanics and analyzed the spectral doublet formed in such a system in greater detail. A theoretical analysis of the cavity-to-cavity coupling was presented. We found that the minimum separation between the peaks of the doublet is equal to 2κ, where κ represents the coupling constant between cavities. An exact expression for κ has not yet been identified. We presented data corresponding to an avoided crossing in a room temperature double Al cavity system as well as a double SRF stub cavity system. We observed a minimum separation of approximately 6.7 MHz at room temperature and approximately 200 kHz at cryogenic temperature.

7.2 Future work

To recap, we have discussed parametric amplification, SRF cavity construction, SRF cavity testing, silicon nitride membrane mechanics, and double SRF cavity mechanics so far in this thesis. All of these topics are necessary when considering the triple cavity system described in Chapter 1. Unfortunately, many of these areas of research have fallen just short of providing us with a working triple cavity. There

is hope, however, in the prospect of continuing this research in the future. While it is true that we did not achieve a Q of 10^9 in a cylindrical Nb cavity, the Nb quarter-wave stub cavity easily reached a Q of 10^9 after minimal etching and baking treatments. Combining this fact with the favorable results from double SRF cavity avoided crossing experiments provides an alternative avenue for this research in the form of a double stub cavity parametric amplifier/oscillator system.

Additionally, several experiments involving stub cavities discussed earlier in this thesis can be further refined or pushed to the next stage. The avoided crossing experiment, for example, demonstrated less than optimal coupling between the two stub cavities due to a mismatch in their intrinsic quality factors. This resulted from the sapphire rod tuning mechanism lowering the Q of cavity S2 to approximately 10^6; a far cry from the 10^9 Q of cavity S1. However, the rod itself has demonstrated interesting behavior while inside the cavity. The way it is clamped to the CLD allows it to act as a cantilever-like oscillator and as it vibrates it appears to shift the frequency of the signal inside the cavity creating sidebands from red and blue detuned photons. Finding a way to alleviate the Q damping could lead to establishing a robust optomechanical system in these cavities.

Further, incorporating a mechanical element offers opportunities for myriad other interesting cQED experiments. Raman scattering [66], optomechanically induced transparency [67, 68], and even a jump into applications in general relativity [69, 70]. Recently, superconducting coaxial RF cavities and microwave circuits have been garnering attention in the field of quantum computing as well [71, 72]. These cavities can also be used as an RF filter for a variety of applications such as acting as the low-pass filter in an optoelectronic oscillator.

All in all, we have created a foundation for ongoing SRF experimentation in the lab when there was no such precedent previously. We have learned a great deal from the SRF community thus far and wish to contribute something ourselves. Continuation of this work will go on to push the boundaries of what those in the scientific community believe SRF cavities can achieve. Other members of the lab are developing equally, if not more, exciting work and I am excited to see their results in the coming years.

Bibliography

[1] V. Braginsky, Sov. Phys. JETP 25 (1967) 653. 2

[2] O. Arcizet, P.-F. Cohadon, T. Briant, M. Pinard, A. Heidmann, Radiation-pressure cooling and optomechanical instability of a micromirror, Nature 444 (7115) (2006) 71. 2

[3] F. Marquardt, J. P. Chen, A. Clerk, S. Girvin, Quantum theory of cavity-assisted sideband cooling of mechanical motion, Physical Review Letters 99 (9) (2007) 093902. 2

[4] Y.-S. Park, H. Wang, Resolved-sideband and cryogenic cooling of an optomechanical resonator, Nature physics 5 (7) (2009) 489. 2

[5] R. Riviere, S. Deleglise, S. Weis, E. Gavartin, O. Arcizet, A. Schliesser, T. J. Kippenberg, Optomechanical sideband cooling of a micromechanical oscillator close to the quantum ground state, Physical Review A 83 (6) (2011) 063835. 2

[6] S. J. Minter, K. Wegter-McNelly, R. Y. Chiao, Do mirrors for gravitational waves exist?, Physica E: Low-dimensional Systems and Nanostructures 42 (3) (2010) 234–255. 3

[7] C. Wilson, G. Johansson, A. Pourkabirian, M. Simoen, J. Johansson, T. Duty, F. Nori, P. Delsing, Observation of the dynamical Casimir effect in a superconducting circuit, Nature 479 (7373) (2011) 376. 4, 47

[8] L. A. Martinez, Parametric oscillation and microwave optomechanics with cm-sized srf cylindrical cavities, Ph.D. thesis, University of California, Merced (2014). 6

[9] J. Bardeen, L. N. Cooper, J. R. Schrieffer, Theory of superconductivity, Physical Review 108 (5) (1957) 1175. 6, 10

[10] J. Bardeen, L. N. Cooper, J. R. Schrieffer, Microscopic theory of superconductivity, Physical Review 106 (1) (1957) 162. 6

[11] B. T. Matthias, T. H. Geballe, V. B. Compton, Superconductivity, Reviews of Modern Physics 35 (1) (1963) 1. 6

[12] M. Schafroth, Theory of superconductivity, Physical Review 96 (5) (1954) 1442. 6

[13] J. G. Bednorz, K. Muller, Earlier and recent aspects of superconductivity. 6

[14] T. Berlincourt, Type ii superconductivity, Reviews of Modern Physics 36 (1) (1964) 19. 6

[15] J. D. Doss, Engineer's guide to high-temperature superconductivity. 6

[16] P. W. Anderson, Coherent excited states in the theory of superconductivity: Gauge invariance and the meissner effect, Physical review 110 (4) (1958) 827. 7

[17] J. Sólyom, Free-electron model of metals, in: Fundamentals of the Physics of Solids, Springer, 2009, pp. 1–76. 9

[18] H. Padamsee, K. Jens, H. Tom, Rf superconductivity for accelerators, New York. A Wiely-Interscience Publication (1998) 129–144. 12, 72

[19] H. Padamsee, The science and technology of superconducting cavities for accelerators, Superconductor science and technology 14 (4) (2001) R28. 13

[20] J. Halbritter, Surface residual resistance of high-q-superconducting resonators, Journal of Applied Physics 42 (1) (1971) 82–87. 14

[21] H. Padamsee, RF superconductivity: science, technology and applications, John Wiley & Sons, 2009. 15

[22] R. W. Boyd, Nonlinear optics, Academic press, 2003. 16, 17

[23] R. Y. Chiao, L. A. Martinez, S. J. Minter, A. Trubarov, Parametric oscillation of a moving mirror driven by radiation pressure in a superconducting fabry–pérot resonator system, Physica Scripta 2012 (T151) (2012) 014073. 19

[24] M. Crocce, D. A. Dalvit, F. C. Lombardo, F. D. Mazzitelli, Hertz potentials approach to the dynamical casimir effect in cylindrical cavities of arbitrary section, Journal of Optics B: Quantum and Semiclassical Optics 7 (3) (2005) S32. 20

[25] S. Kuhr, S. Gleyzes, C. Guerlin, J. Bernu, U. B. Hoff, S. Deléglise, S. Osnaghi, M. Brune, J.-M. Raimond, S. Haroche, et al., Ultrahigh finesse Fabry-Pérot superconducting resonator, Applied Physics Letters 90 (16) (2007) 164101. 22

[26] M. Reagor, H. Paik, G. Catelani, L. Sun, C. Axline, E. Holland, I. M. Pop, N. A. Masluk, T. Brecht, L. Frunzio, et al., Reaching 10 ms single photon lifetimes for superconducting aluminum cavities, Applied Physics Letters 102 (19) (2013) 192604. 22

[27] I. Wilson, C. Schramm, J. Kinzer, High Q resonant cavities for microwave testing, Bell Labs Technical Journal 25 (3) (1946) 408–434. 23

[28] H. L. Thal, Cylindrical TE 011/TM111 mode control by cavity shaping, IEEE Transactions on Microwave Theory and Techniques 27 (12) (1979) 982–986. 24

[29] A. Suri, Extractive metallurgy of niobium, Routledge, 2017. 27, 28

[30] J. Turneaure, I. Weissman, Microwave surface resistance of superconducting niobium, Journal of Applied Physics 39 (9) (1968) 4417–4427. 29

[31] J. P. Turneaure, N. T. Viet, Superconducting Nb TM010 mode electron-beam welded cavities, Applied Physics Letters 16 (9) (1970) 333–335. 29

[32] M. Kinter, I. Weissman, W. Stein, Chemical polish for niobium microwave structures, Journal of Applied Physics 41 (2) (1970) 828–829. 29

[33] Y. Jung, H. J. Kim, H. H. Lee, H. C. Yang, Analysis of bcp characteristics for srf cavities. 29

[34] Y. Tereshkin, G. Davis, A. Rowe, H. Edwards, C. Boffo, Bcp processing facility, in: Presented at, no. FERMILAB-CONF-03-241-E, 2003. 30

[35] D. Bloess, Chemistry and surface treatment, SRF-84, Geneva, July (1984) 409–425. 30

[36] C. Preston, T. Grimm, C. Compton, N. Sanborn, Etching of niobium in buffered chemical polish in a small ventilated room, Michigan State University report 24. 30

[37] C. Preston, N. Sanborn, C. Compton, T. Grimm, Non-temperature controlled etching of niobium in bcp, Michigan State University report 21. 30

[38] P. Bauer, L. Bellantoni, T. Berenc, C. Boffo, R. Carcagno, C. Chapman, H. Edwards, L. Elementi, M. Foley, E. Hahn, et al., Srf cavity and materials r&d at fermilab, in: Proceedings of LINAC, 2004. 30

[39] D. Baird, C. Boffo, C. Cooper, R. Ruthe, Vapor generation and mist evaporation during buffered chemical polish (bcp) operations at the material development testing laboratory (mdtl). 30

[40] P. Dhakal, G. Ciovati, G. Myneni, K. Gray, N. Groll, P. Maheshwari, D. McRae, R. Pike, T. Proslier, F. Stevie, et al., Effect of high temperature heat treatments on the quality factor of a large-grain superconducting radio-frequency niobium cavity, Physical Review Special Topics-Accelerators and Beams 16 (4) (2013) 042001. 35, 83

[41] G. Ciovati, Effect of low-temperature baking on the radio-frequency properties of niobium superconducting cavities for particle accelerators, Journal of Applied Physics 96 (3) (2004) 1591–1600. 35, 72

[42] D. M. Pozar, Microwave engineering, John Wiley & Sons, 2009. 36, 41

[43] M. J. Reagor, Superconducting cavities for circuit quantum electrodynamics, Yale University, 2016. 41

[44] L. A. Martinez, A. R. Castelli, W. Delmas, J. E. Sharping, R. Chiao, Electromagnetic coupling to centimeter-scale mechanical membrane resonators via RF cylindrical cavities, New Journal of Physics 18 (11) (2016) 113015. 42, 59

[45] C. H. Bui, J. Zheng, S. Hoch, L. Y. Lee, J. Harris, C. Wei Wong, High-reflectivity, high-Q micromechanical membranes via guided resonances for enhanced optomechanical coupling, Applied Physics Letters 100 (2) (2012) 021110. 47

[46] T. Morkved, W. Lopes, J. Hahm, S. Sibener, H. Jaeger, Silicon nitride membrane substrates for the investigation of local structure in polymer thin films, Polymer 39 (16) (1998) 3871–3875. 47, 48

[47] J. Zmuidzinas, Superconducting microresonators: Physics and applications, Annu. Rev. Condens. Matter Phys. 3 (1) (2012) 169–214. 47

[48] S. H. Ma, L. A. Lepak, R. J. Hussain, W. Shain, M. L. Shuler, An endothelial and astrocyte co-culture model of the blood–brain barrier utilizing an ultra-thin, nanofabricated silicon nitride membrane, Lab on a Chip 5 (1) (2005) 74–85. 47

[49] S. Gröblacher, K. Hammerer, M. R. Vanner, M. Aspelmeyer, Observation of strong coupling between a micromechanical resonator and an optical cavity field, Nature 460 (7256) (2009) 724. 47, 48

[50] K. Børkje, S. Girvin, Quantum optomechanics with a high-frequency dilational mode in thin dielectric membranes, New Journal of Physics 14 (8) (2012) 085016. 47

[51] G. D. Cole, W. Zhang, M. J. Martin, J. Ye, M. Aspelmeyer, Crystalline coatings for ultra-low-noise optical cavities, in: CLEO: Science and Innovations, Optical Society of America, 2013, pp. JM2N–2. 48

[52] R. Russo, L. Catani, A. Cianchi, S. Tazzari, J. Langner, High quality superconducting niobium films produced by an ultra-high vacuum cathodic arc, Superconductor Science and Technology 18 (7) (2005) L41. 50

[53] C. Benvenuti, S. Calatroni, P. Darriulat, M. Peck, A.-M. Valente, Fluxon pinning in niobium films, Physica C: Superconductivity 351 (4) (2001) 429–437. 50

[54] M. Krishnan, E. Valderrama, B. Bures, K. Wilson-Elliott, X. Zhao, L. Phillips, A.-M. Valente-Feliciano, J. Spradlin, C. Reece, K. Seo, Very high residual resistivity ratios of heteroepitaxial superconducting niobium films on mgo substrates, Superconductor Science and Technology 24 (11) (2011) 115002. 50

[55] D. J. Griffiths, Introduction to electrodynamics (1989), Google Scholar. 55

[56] R. E. Ricker, G. R. Myneni, Evaluation of the propensity of niobium to absorb hydrogen during fabrication of superconducting radio frequency cavities for particle accelerators, Journal of research of the National Institute of Standards and Technology 115 (5) (2010) 353. 72

[57] A. Grassellino, A. Romanenko, D. Sergatskov, O. Melnychuk, Y. Trenikhina, A. Crawford, A. Rowe, M. Wong, T. Khabiboulline, F. Barkov, Nitrogen and argon doping of niobium for superconducting radio frequency cavities: a pathway to highly efficient accelerating structures, Superconductor Science and Technology 26 (10) (2013) 102001. 72

[58] A. Romanenko, F. Barkov, L. Cooley, A. Grassellino, Proximity breakdown of hydrides in superconducting niobium cavities, Superconductor Science and Technology 26 (3) (2013) 035003. 72, 83

[59] S.-L. Zhu, Z. Wang, K. Yang, Quantum-information processing using josephson junctions coupled through cavities, Physical Review A 68 (3) (2003) 034303. 72

[60] C.-Y. Chen, M. Feng, K.-L. Gao, Toffoli gate originating from a single resonant interaction with cavity qed, Physical Review A 73 (6) (2006) 064304. 72

[61] H. Paik, D. Schuster, L. S. Bishop, G. Kirchmair, G. Catelani, A. Sears, B. Johnson, M. Reagor, L. Frunzio, L. Glazman, et al., Observation of high coherence in josephson junction qubits measured in a three-dimensional circuit qed architecture, Physical Review Letters 107 (24) (2011) 240501. 72

[62] J. Teufel, D. Li, M. Allman, K. Cicak, A. Sirois, J. Whittaker, R. Simmonds, Circuit cavity electromechanics in the strong-coupling regime, Nature 471 (7337) (2011) 204. 72

[63] T. Palomaki, J. Harlow, J. Teufel, R. Simmonds, K. Lehnert, Coherent state transfer between itinerant microwave fields and a mechanical oscillator, Nature 495 (7440) (2013) 210. 72

[64] R. Andrews, A. Reed, K. Cicak, J. Teufel, K. Lehnert, Quantum-enabled temporal and spectral mode conversion of microwave signals, Nature communications 6 (2015) 10021. 72

[65] H. Diepers, H. Martens, Superconducting niobium te011 mode cavities with high critical magnetic field and high q value, Physics Letters A 38 (5) (1972) 337–338. 83

[66] P. Roelli, C. Galland, N. Piro, T. J. Kippenberg, Molecular cavity optomechanics as a theory of plasmon-enhanced raman scattering, Nature nanotechnology 11 (2) (2016) 164–169. 85

[67] M. Aspelmeyer, T. J. Kippenberg, F. Marquardt, Cavity optomechanics, Reviews of Modern Physics 86 (4) (2014) 1391. 85

[68] T. Ojanen, K. Børkje, Ground-state cooling of mechanical motion in the unresolved sideband regime by use of optomechanically induced transparency, Physical Review A 90 (1) (2014) 013824. 85

[69] R. Y. Chiao, R. W. Haun, N. A. Inan, B.-S. Kang, L. A. Martinez, S. J. Minter, G. A. Munoz, D. A. Singleton, A gravitational aharonov-bohm effect, and its connection to parametric oscillators and gravitational radiation, in: Quantum Theory: A Two-Time Success Story, Springer, 2014, pp. 213–246. 85

[70] Y. Ma, S. L. Danilishin, C. Zhao, H. Miao, W. Z. Korth, Y. Chen, R. L. Ward, D. G. Blair, Narrowing the filter-cavity bandwidth in gravitational-wave detectors via optomechanical interaction, Physical review letters 113 (15) (2014) 151102. 85

[71] B. Vogell, B. Vermersch, T. Northup, B. Lanyon, C. Muschik, Deterministic quantum state transfer between remote qubits in cavities, Quantum Science and Technology 2 (4) (2017) 045003. 85

[72] T. Brecht, W. Pfaff, C. Wang, Y. Chu, L. Frunzio, M. H. Devoret, R. J. Schoelkopf, Multilayer microwave integrated quantum circuits for scalable quantum computing, npj Quantum Information 2 (2016) 16002. 85